Dissecting Conformational Dynamics and Ligand Binding in Substrate Binding Proteins using single-molecule Förster Resonance Energy Transfer

Zhongying Han

München, June.05.2023

Dissecting Conformational Dynamics and Ligand Binding in Substrate Binding Proteins using single-molecule Förster Resonance Energy Transfer

Dissertation

an der Fakultät für Biologie

der Ludwig-Maximilians-Universität München

vorgelegt von

Zhongying Han

aus Shandong, China

München, June.05.2023

Gutachter:

1. Prof. Dr. Thorben Cordes

2. Prof. Dr. Philip Tinnefeld

Datum der Abgabe: 05.06.2023

Datum der mündlichen Prüfung: 07.12.2023

Eidesstattliche Erklärung

Hiermit erkläre ich, dass ich diese Dissertation selbstständig angefertigt und weder ganz noch teilweise einem anderen Prüfungsausschuss vorgelegt habe. Ich habe nicht versucht, die Dissertation einzureichen oder die Promotionsprüfung auf andere Weise abzulegen.

München, den June. 05. 2023

Zhongying Han

Statutory declaration and statement

I hereby declare that I completed this thesis independently and that it has not been submitted to another examination board in whole or in part. I have not attempted to submit the thesis or take the Ph.D. exam in any other way.

München, den. June 05.2023

Zhongying Han

List of publications

1. Patrick Eiring[+], Ryan McLaughlin[+], Siddharth S. Matikonda[+], **Zhongying Han[+]**, Lennart Grabenhorst[+], Dominic A. Helmerich, Mara Meub, Gerti Beliu, Michael Luciano, Venu Bandi, Niels Zijlstra, Zhen-Dan Shi, Sergey G. Tarasov, Rolf Swenson, Philip Tinnefeld, Viktorija Glembockyte,* Thorben Cordes,* Markus Sauer* and Martin J. Schnermann*. Targetable Conformationally Restricted Cyanines Enable Photon-Count-Limited Applications. *Angew*. *Chem*. 2021, 133, 26889 – 26897.

   [+] These authors contributed equally to this work.

2. **Zhongying Han**, Sabrina Panhans, Marija Ram, Anna Herr, Alessandra Narducci, Michael Isselstein, Oliver Brix, Paul D. Harris, Eitan Lerner, Douglas Griffith, Niels Zijlstra* and Thorben Cordes*. Dissecting Mechanisms of Ligand Binding and Conformational Changes in the Glutamine-Binding Protein.

Publication I:

Patrick Eiring[+], Ryan McLaughlin[+], Siddharth S. Matikonda[+], **Zhongying Han[+]**, Lennart Grabenhorst[+], Dominic A. Helmerich, Mara Meub, Gerti Beliu, Michael Luciano, Venu Bandi, Niels Zijlstra, Zhen-Dan Shi, Sergey G. Tarasov, Rolf Swenson, Philip Tinnefeld,Viktorija Glembockyte,* Thorben Cordes,* Markus Sauer* and Martin J. Schnermann*. Targetable Conformationally Restricted Cyanines Enable Photon-Count-Limited Applications. *Angew*. *Chem*. 2021, 133, 26889 – 26897.

[+] These authors contributed equally to this work.

In this publication, I labelled the protein model system MalE with different fluorophore pairs and managed to do the solution-based single-molecule FRET measurements. My contributions are Fig. 3 and Fig.4 in the main text, Fig. S2, Fig. S3 and Fig. S4 in the supporting information.

Publication II:

Zhongying Han[1], Sabrina Panhans[1], Marija Ram[1], Anna Herr[1], Alessandra Narducci[1], Michael Isselstein[1], Oliver Brix[1], Paul D. Harris[2], Eitan Lerner[2,3], Douglas Griffith[1], Niels Zijlstra[1,*] and Thorben Cordes[1,*]. Dissecting Mechanisms of Ligand Binding and Conformational Changes in the Glutamine-Binding Protein.

In this publication, I performed the protein labelling, purification, isothermal titration calorimetry (ITC) and surface-immobilized smFRET measurements. Sabrina Panhans and Marija Ram overexpressed the wild-type GlnBP and two mutants. Anna Herr and I performed solution-based single-molecule experiments. Alessandra Narducci established the unfolding and refolding

protocol. Michael Isselstein aligned and established the total internal reflection fluorescence (TIRF) microscopy. Oliver Brix wrote the script to merge all the TIRF results together. Paul D. Harris and Eitan Lerner performed data analysis using mpH^{2}MM and presented Fig. 4 and Fig. S9, S10. Dr.Niels Zijlstra and Prof. Dr. Thorben Cordes conceived and designed the project. Prof. Dr. Thorben Cordes and I wrote the paper. Dr. Douglas Griffith presented Fig. 1C and revised the paper. I analysed and presented all the other figures in the paper.

We hereby confirm the above statements:

Zhongying Han   Thorben Coedes

天将降大任于斯人也，必先苦其心志，劳其筋骨，饿其体肤，空乏其身，行拂乱其所为，所以动心养性，增益其所不能。

<div align="right">孟子 – 公元前 551</div>

When Heaven is about to place a great responsibility on a person, it always first frustrates his spirit and will, exhaust his muscles and bones, expose him to starvation and poverty, harass him by troubles and setback to stimulate his spirit, toughen his nature and enhance his abilities.

<div align="right">**Mencius – B. C. 551**</div>

Table of contents

Abbreviations

SBPs	Substrate-Binding Proteins
NMR	Nuclear Magnetic Resonance
PRE	paramagnetic relaxation enhancement
MD	Molecular Dynamics
MalE	Maltose Binding Protein
GlnBP	Glutamine Binding Protein
Thr	Threonine
Cys	Cysteine
Ser	Serine
IF	induced fit
CS	Conformational selection
ITC	Isothermal Titration Calorimetry
SPR	Surface-plasmon resonance
mpH^{2}MM	Multiple parameters Hidden Markov Modelling
MFD	Multiparameter fluorescence detection
PIE	Pulsed Interleaved Excitation
TIRF	Total Internal Reflection Fluorescence
STED	Stimulated emission depletion
STORM	Stochastic Optical Reconstruction Microscopy
SBD	Substate-Binding Domain
PBP	Periplasmic Binding Protein
GlnBP(111-192)	GlnBP(Val111Cys-Gly192Cys)
GlnBP(59-130)	GlnBP(ThrCys-Thr192Cys)
Val	Valine
Gly	Glycine
***L*-Gln**	*L*-glutamine
***L*-Arg**	*L*-arginine

smFRET	Single-molecule Förster Resonance Energy Transfer
ALEX	Alternating-laser Excitation Microscopy
APBS	All Photon Burst Search
DCBS	Dual Channel Burst Search
POC	Pyranose oxidase and catalase
TX	Trolox
BVA	Burst Variance Analysis
RDC	Residual Dipolar Coupling
MSM	Markov State Model
Kd	Dissociation Constant
AV	Accessible Volumes
FPS	FRET-restrained positioning and screening method
FCS	Fluorescence correlation spectroscopy
MFD	Multiparameter fluorescence detection
PIE	Pulsed interleaved excitation

1 Abstract

Over the past decades, the conformational dynamics and ligand binding mechanism of (prokaryotic) substrate binding proteins have been studied. Their conformational landscape with two conformational states allows for ligand binding via induced-fit IF (binding first), via the conformational selection mechanism CS (conformational change first), or a combination thereof. Recently, however, this simple two state model was challenged. This thesis deals with the development of novel approaches and assays that can help to clarify ligand binding mechanisms and to monitor conformational dynamics in proteins, which are a hallmark of various fundamental biological processes. Single-molecule Förster-resonance energy transfer (smFRET) was employed to probe both intrinsic and ligand-induced conformational dynamics of SBPs at room temperature.

For smFRET assays, excellent dye properties of are a prerequisite. Consequently, we show here in the first part of the thesis that novel conformationally restrained sulfonated cyanine fluorophores can improve FRET assays to monitor protein conformational states. To benchmark the performance of these dyes in smFRET experiments, I selected the ABC-transporter related MalE as a protein model system and benchmarked the performance of newly established rigidized cyanine dyes against established gold-standards.

In the second part of the results in this thesis, I provide a detailed characterization of the ligand binding mechanism of GlnBP. For this we used a combination of isothermal titration calorimetry (ITC), single-molecule Förster resonance energy transfer (smFRET) and surface-plasmon resonance (SPR). Our combined experimental analysis in combination with kinetic modelling suggests that conformational changes in GlnBP (mostly) occur in the presence of ligand and exclude any conformational dynamics of apo- and holo-GlnBP on timescales between 1 μs and 10 ms.

2 Introduction

2.1 Aims of the thesis

Although fluorescent dyes are among the most widely used bioimaging techniques as they provide detailed information on a single biomolecular level with high spatial and temporal resolution. But one of the most widely used cyanine dyes can impact the photon output by the inherent *cis-trans* photoisomerization. To address this issue, our collaborators from the Schnermann laboratory added a ring system to pentamethine cyanine, which can increase the quantum yield and extend the lifetime of cyanine chromophores.

Consequently, the first aim of the thesis is to prove that the conformationally restrained sulfonated cyanine fluorophores are much more stable than the parent cyanine chromophores in the smFRET applications. To approach this, I selected MalE, as a protein model system, which has two cysteines on positions Thr36Cys and Ser352Cys that can be labelled with maleimide-modified fluorophore pairs, i. e. donor and acceptor fluorescent dyes (see chapter 4.1), to study the conformational changes of MalE. I also implemented solution-based smFRET measurements on MalE to study structural changes and dynamics of biomacromolecules in aqueous solution.

The conformational dynamics and ligand binding interaction of GlnBP have been studied using smFRET measurements. The crystal structure of GlnBP show that the GlnBP adopt an open (apo) state in the absence of ligand and a closed state in the presence of ligand. However, recent studies indicated that GlnBP can adopt various states either in the absence of ligand or in the presence of ligand and the binding mechanism is concluded by the combination of IF and CS, which is highly unlikely as what I know from the SBPs.

Therefore, the second aim of the thesis is to decipher the conformational dynamics and binding mechanism of GlnBP using smFRET technology. For this work, we produced GlnBP wild-type and two double-cysteine variants (see chapter 4.2) for fluorophore attachment and smFRET measurements. With these proteins, we

present a biochemical and biophysical characterization of GlnBP to derive the thermodynamic and kinetic characteristics of ligand binding and conformational changes. For this we used a combination of ITC (see chapter 4.23), smFRET (see chapter 4.25) and SPR measurements. Our combined analysis of the ligand-free and ligand-bound states of GlnBP via ITC and smFRET strongly suggests that conformational changes in GlnBP (mostly) occur in the presence of ligand. Also, the kinetic evaluation of the SPR data indicated that GlnBP is most likely to use the IF ligand binding mechanism. Our analysis also excludes any conformational dynamics of apo- and holo-GlnBP on timescales between 100 µs and 10 ms via mpH^{2}MM (see chapter 4.26) and even down to 100 ns via MFD-PIE and FCS with larger amplitudes (see chapter 4.27).

The last goal of the thesis is to screen the rare conformational events of surface-immobilized GlnBP on slower timescales (i.e., > 100 ms) using TIRF-microscopy. Unfortunately, GlnBP did not retain its biochemical activity on the glass coverslips and <50 % of all GlnBP molecules showed a shift of conformational states upon addition of the ligand.

Over the past decades, the conformational dynamics and ligand binding mechanism of (prokaryotic) substrate binding proteins (SBPs, Figure 1) have been studied. The conformational landscape of SBPs with two conformational states (open/closed, Figure 1B) allows for ligand binding via induced-fit IF (binding first), via the conformational selection mechanism CS (conformational change first), or a combination thereof (Figure 1C). Recently, however, this simple two state model was challenged by NMR paramagnetic relaxation enhancement experiments (PRE) and MD simulations that suggest the existence of unliganded closed or semi-closed states in SBPs such as maltose binding protein, MalE or glutamine binding protein GlnBP (Figure 1C). Additionally, single-molecule approaches, such as nanopore-recordings and single-molecule Förster-resonance energy transfer (smFRET), were employed to probe both intrinsic and ligand-induced conformational dynamics of SBPs at room temperature in buffer solution to better understand which crystallographic states are present in solution and with what kinetics these interconvert.
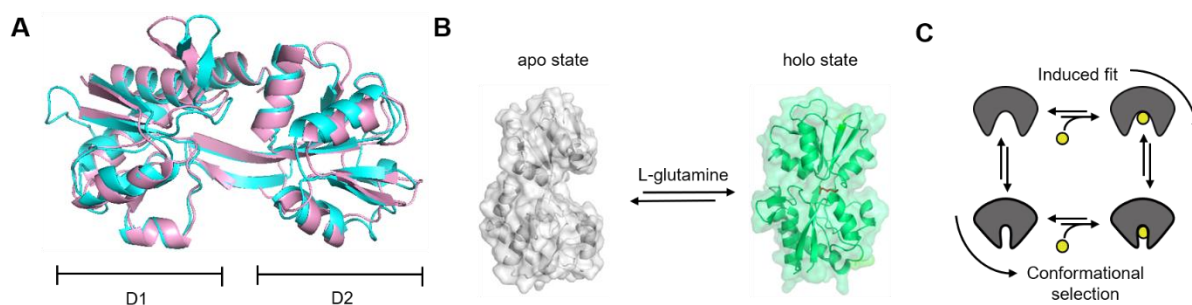
Figure 1. Conformational states and possible ligand binding mechanisms of a typical SBP. (A) Structural comparison of SBD2 from *Lactococcus Lactis* (4KR5[1]; cyan) and GlnBP from *E. coli* (pink). SBD2 and GlnBP share 34% sequence identity with a TM-score of 0.90, indicating that the two proteins are structurally very similar. (B) Crystal structures of the ligand-free (PDB file:1GGG[2]; grey) and ligand-bound GlnBP (PDB file:1WDN; green) from *E. coli*. (C) Sketch of ligand binding via induced-fit (IF) and conformational selection (CS) mechanisms.

This thesis deals with the development of novel approaches and assays that can help to clarify ligand binding mechanisms and to monitor conformational

dynamics in proteins. Why are such studies relevant? – Often, the existence of a ligand-free protein conformation is taken as an indicator for CS as a dominant pathway (Figure 1C). However, the existence of a ligand-free protein conformation that structurally resembles a ligand-bound form is a necessary, but insufficient evidence for the operation of a CS mechanism (Figure 1C), as ligand binding may not proceed via this conformation at all. Whether such a ligand-free closed (or near closed) conformation can be observed depends on the magnitude of its equilibrium probability as well as the sensitivity of the techniques used to probe it. Nevertheless, an inability to detect such ligand-free (closed) conformations is often taken as an indicator for IF as a dominant pathway (Figure 1C), again based on insufficient evidence. Thus, we wanted to try to develop a procedure that allows to obtain sufficient information on the proteins MalE and GlnBPs to make a conclusive statement about their ligand binding mechanisms.

Consequently, we show in this thesis that the conformationally restrained sulfonated cyanine fluorophores can improve commonly used assays to monitor protein conformational states via intramolecular Förster Resonance Energy Transfer (FRET) assays. FRET has become a popular tool in biological science [3, 4] since it is well adapted to studying biomolecules like nucleic acids or proteins at the nanometer scale and is sensitive to distances in the range of 3–12 nm [5]. The energy transferred between the two spectrally different donor and acceptor fluorophores in fluorescence investigation employing directly reflects their proximity and FRET is often referred to as a molecular ruler. The realization of experiments with single-molecule sensitivity (smFRET), pioneered by Shimon Weiss, Taekip Ha and co-workers nearly 25 years ago [6], has been a breakthrough in this field. With the technique conformational heterogeneity can be resolved and dynamic transitions between different states can be observed by measuring one FRET pair at a time. Since then, smFRET has been widely used to investigate the conformational dynamics and interaction of individual

biomolecules [7], and this is the primary method used in this thesis to examine the conformational dynamics of proteins.

For smFRET assays, excellent photophysical properties of dye are a prerequisite. Synthetic fluorescent dye molecules are widely used in such assays and can provide detailed information on conformational states and changes in biomolecules with high spatial and temporal resolution. The performance and photon output of the popular cyanine dyes is often hampered by the inherent ability for *cis-trans* photoisomerization that can occur around the polymethine chain (Figure 2) and lets to a reduction of quantum yield due to internal conversion. To address this issue, our collaborators from the Schnermann laboratory at NIH rigidized the polymethine dye core to increase the quantum yield and the lifetime of cyanine chromophores as shown below.
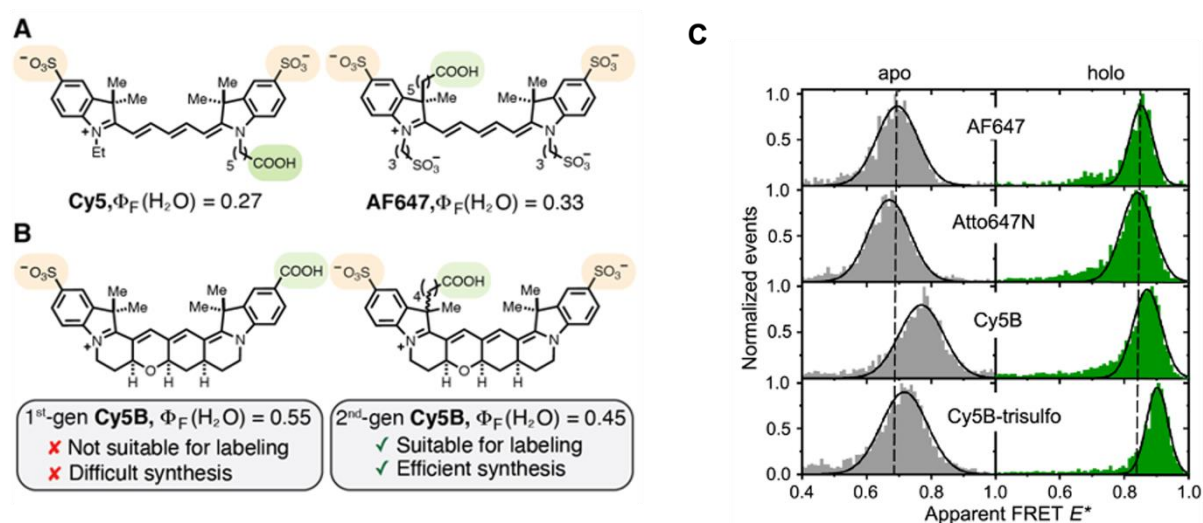
Figure 2: (A) Previously reported pentamethine cyanines, and (B) evolution of restrained pentamethine variants. Orange: sulfonated positions, Green: site of bioconjugation. (C) Apparent FRET efficiency E* histograms of MalE obtained from single molecule μsALEX FRET experiments. Different FRET acceptor fluorophores as indicated in the Figure panels were combined with the same donor fluorophore (AF555). E* histograms were recorded in the absence (apo) and presence of saturating ligand concentrations of 100 mM maltose (holo). All histograms shown are projections from bursts with a stoichiometry between 0.3 and 0.7.

To benchmark the performance of these dyes in smFRET experiments, we selected MalE as a protein model system with two cysteine residues at positions Thr36Cys and Ser352Cys for labelling with maleimide-modified fluorophore pairs. In these experiments, the conformationally restrained sulfonated cyanine fluorophores (Figure 2A/B) were benchmarked against the commonly used acceptor dyes AF647 and Atto647N (Figure 2C).

In the second part of the results in this thesis, we studied the conformational dynamics in GlnBP and understand what is ligand-driven, which changes occur intrinsically and what the relevance of both is mechanistically. For this work, we produced GlnBP wild-type and two double-cysteine variants for fluorophore attachement and smFRET measurements. With these proteins, we present a biochemical and biophysical characterization of GlnBP to derive the thermodynamic and kinetic characteristics of ligand binding and conformational changes. For this we used a combination of isothermal titration calorimetry (ITC), single-molecule Förster resonance energy transfer (smFRET) and surface-plasmon resonance (SPR). After verification of the thermodynamic ligand binding characteristics of GlnBP, we characterized the conformational states and changes associated to ligand binding via smFRET. Our combined analysis of the ligand-free and ligand-bound states of GlnBP via ITC and smFRET strongly suggests that conformational changes in GlnBP (mostly) occur in the presence of ligand. Our analysis also excludes any conformational dynamics of apo- and holo-GlnBP on timescales between 100 µs and 10 ms via mpH2MM and even down to 100 ns via MFD-PIE and FCS with larger amplitudes (Figure 3).
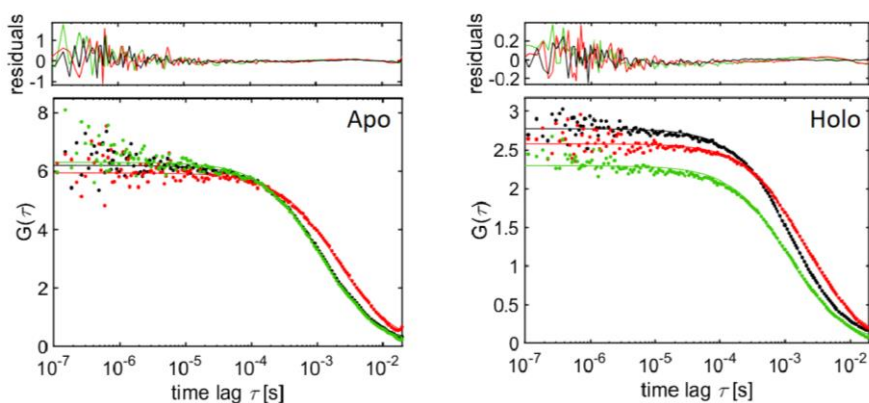
Figure 3. Analysis of conformational dynamics using burst-wise FCS for apo and holo states. The autocorrelation functions of the detected donor (DDxDD) and acceptor signal (AAxAA) are displayed in green and red, respectively. The cross-correlation function between donor and FRET signal (DDxDA) is shown in black and have no sign of conformational (FRET) dynamics below 100 µs.

We also performed TIRF-microscopy with surface-immobilized GlnBP to characterize the protein and its conformational dynamics on slower timescales (i.e., > 100 ms) and to screen for rare conformational events, which are better observed in surface-immobilized smFRET experiments due to longer observation times (Figure 4). Unfortunately, GlnBP did not retain its biochemical activity on the glass coverslips and <50 % of all GlnBP molecules showed a shift of conformational states upon addition of the ligand (Figure 4). Based on these findings, we conclude that our fluorophore-labelled GlnBP cannot be used for mechanistic analysis based on surface-immobilization.
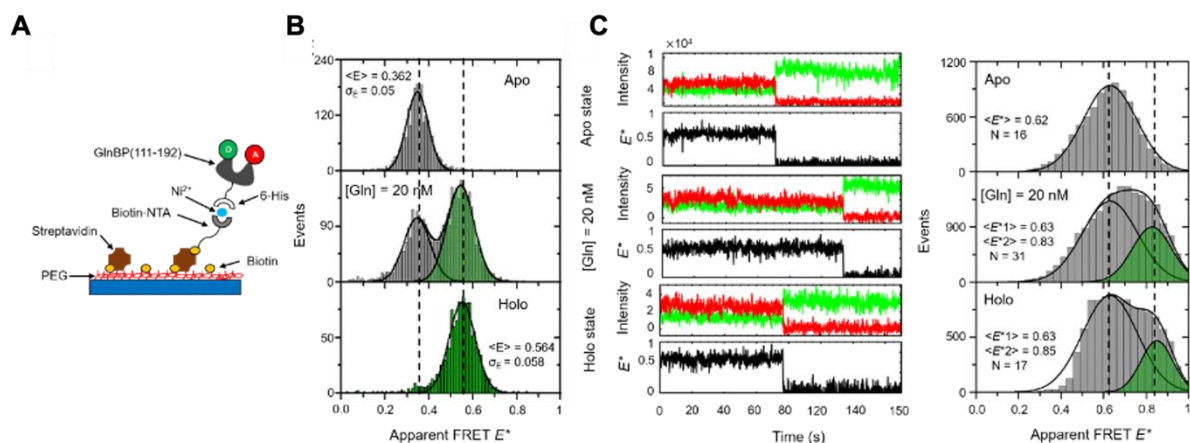
Figure 4. Comparing smFRET measurements of GlnBP(111-192) using diffusion-based µsALEX versus TIRF microscopy. (A) Schematic view of the refolded GlnBP(111-192) labelled with Atto532-Atto643 for smFRET characterization. (B) Typical µs-ALEX-based E*-S* histograms of the refolded GlnBP(111-192). (C) Representative fluorescence time trace of respective single emitter of the refolded GlnBP(111-192) under continuous wave excitation of ~500 µW at 532 nm and the FRET histograms of all analyzed molecules.

To complement the available information on conformational changes, we performed surface plasmon resonance (SPR) spectroscopy to obtain kinetic information on the association and dissociation steps of ligand binding. It is important to highlight that SPR and smFRET have a distinct ability to monitor protein ligand complex formation. SPR exclusively monitors a mass increase in the vicinity of the chip, i.e., on the immobilized protein and with that protein-ligand interaction. Since conformational changes are not seen, SPR can monitor formation of final CL state for the CS mechanism, but only the intermediate OL complex formation for IF (Figure 1B). It is inverse for smFRET which allows to follow formation of the CL state for IF, but it cannot discriminate between C and CL state in the CS mechanism and would here monitor an intermediate state C in the ligand binding pathway.

In SPR, GlnBP showed specific and stable interaction with glutamine based on the magnitude of the equilibrium RU response as a function of glutamine concentration (Figure 5A). Analysis of the concentration-dependent maximal RU units and fitting to a simply Hill binding model with no cooperativity yields an

affinity of 21 nM (Figure 5B) which is internally consistent with all other data (Figure 3/4). Also, the kinetic evaluation of the data indicated that GlnBP is most likely to use the IF ligand binding mechanism.
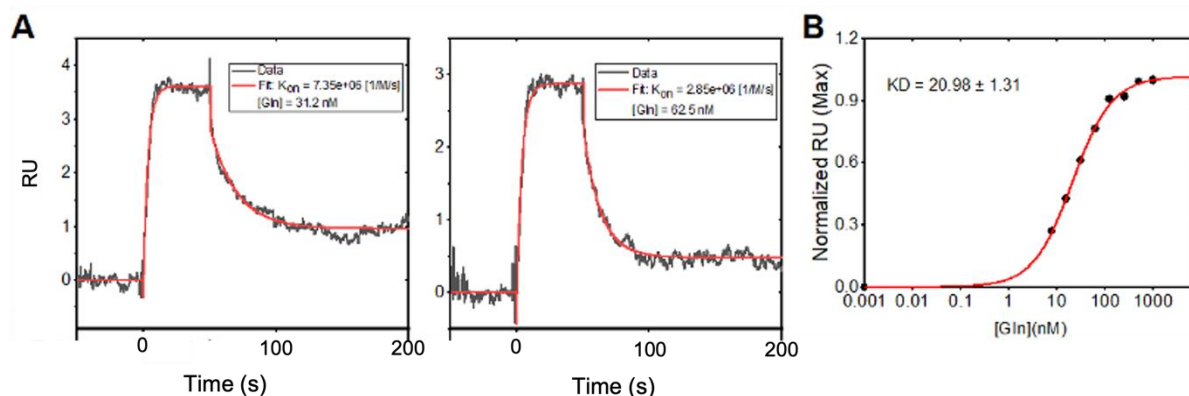
Figure 5. Kinetic analysis of ligand binding and dissociation in GlnBP using SPR. (A) SPR sensor gram for association, equilibrium, and dissociation phases for two different ligand concentrations as indicated. Globally derived kon and koff rate constants from the Langmuir model are indicated in the respective panel. (B) Determination of Kd values from normalized equilibrium responses of the SPR from single-cycle kinetics.

2.2 Basics of fluorescence

Fluorescence is the spontaneous emission of light from an excited state chromophore[8, 9]. The phenomenon has become widely used in the natural sciences for various applications[9]. Fluorescence spectroscopy, i.e., the analysis of different photophysical parameters of a fluorophore, plays an important role in biochemistry and in biophysics[10]. With the development of advanced fluorescence imaging methods, e.g., immunohistochemistry, live-cell fluorescence imaging, confocal microscopy[7] and super-resolution microscopy (STED or STORM[11]), it has also expanded into biotechnology, medical diagnostics, and genetic analysis[9]. Furthermore, fluorescence imaging can be employed at the level of single-molecule detection and thus enables ultra-sensitive and specific detection of biomacromolecules[12-14].

Fluorescence is an optical phenomenon where the first excited electronic singlet state S_1 decays spontaneously into the ground state S_0 via emission of a photon. Biologically relevant fluorescence phenomena often originate from aromatic and

planar molecules as shown in Figure 2.2. Depending on the radiative rate constant k of the emission and the nature of the state (singlet vs. triplet), the luminescence is divided into two categories: fluorescence ($k \sim 10^8$ s^{-1}) and phosphorescence ($k \sim 10^3$ s^{-1} to 10^0 s^{-1})[15] – in this thesis we will focus on the phenomenon of fluorescence in which the electron returns to its initial state S$_0$ after a characteristic lifetime τ on the nanosecond timescale. However, the emitted fluorescence photons exhibit lower frequencies (longer wavelength, Stokes Shift) since a portion of the energy of the absorbed photon is lost via vibrational relaxation. Competing pathways are the non-radiative pathways internal conversion and intersystem crossing. In the latter, the excited state electron can enter a triplet state T$_1$. The triplet state is relevant since it is chemically reactive and is one important source of photobleaching and for the generation of damaging free radicals such as reactive oxygen species (ROS)[16]. The triplet state can be depopulated by the interaction with triplet oxygen (O_2^3). The excited singlet or triplet states can also interat with oxidizing or reducing substances to generate radical ion states ($F^{\cdot+/-}$), which can be recovered via the complementary redox reaction. A graphical representation of relevant photophysical is displayed in a Jablonski diagram as shown in Fig. 2.1.

11
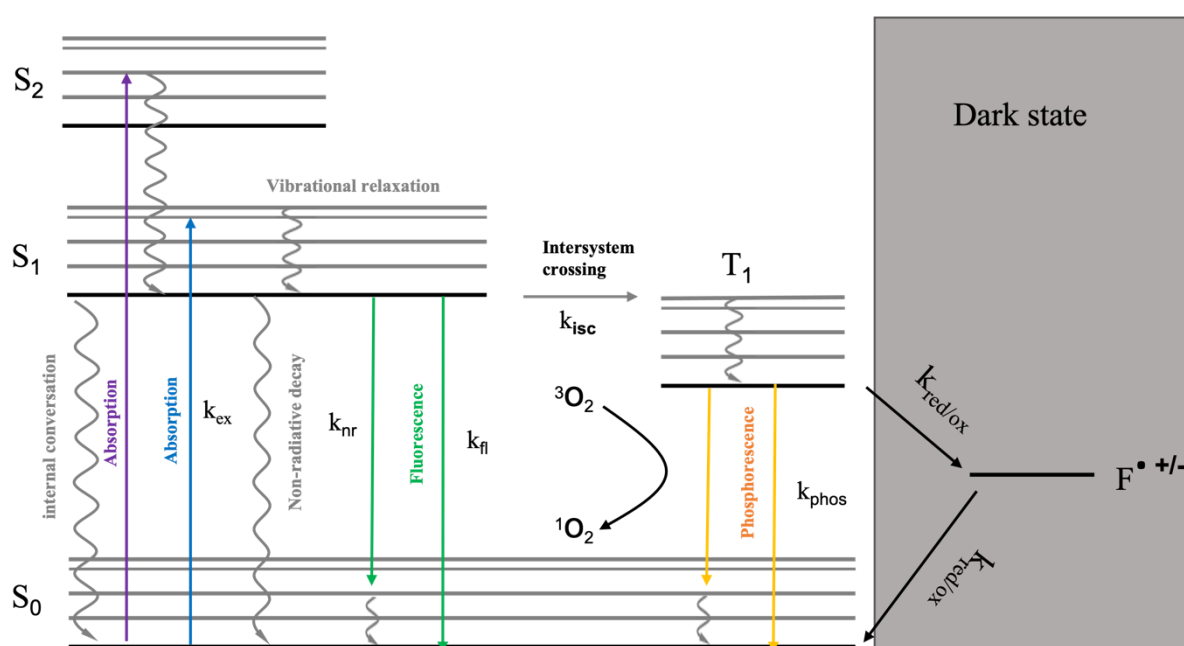
Fig. 2.1. Jablonski Energy Diagram. A Jablonski diagram of a fluorophore consists of S_0: the ground state, S_1, S_2: singlet first and second excited state, T_1: the triplet state, k_{ex}: excitation rate, k_{nr}: non-radiative decay rate, k_{fl}: intrinsic fluorescence emission rate, k_{isc}: intersystem crossing rate, and k_{phos}: phosphorescence emission rate.

2.2.1   Fluorophores

Organic dyes molecules are popular fluorophores due to their large quantum yield and high absorbance cross section, making them ideal markers for single-molecule applications. The fluorescence spectrum is shifted towards lower energy (red shift) in comparison to the absorption caused by the loss of energy by vibrational relaxation. Oftentimes, the core structures are modified by attaching charged side groups (e.g., SO3-) in order to improve the solubility in water (Fig 2.2).
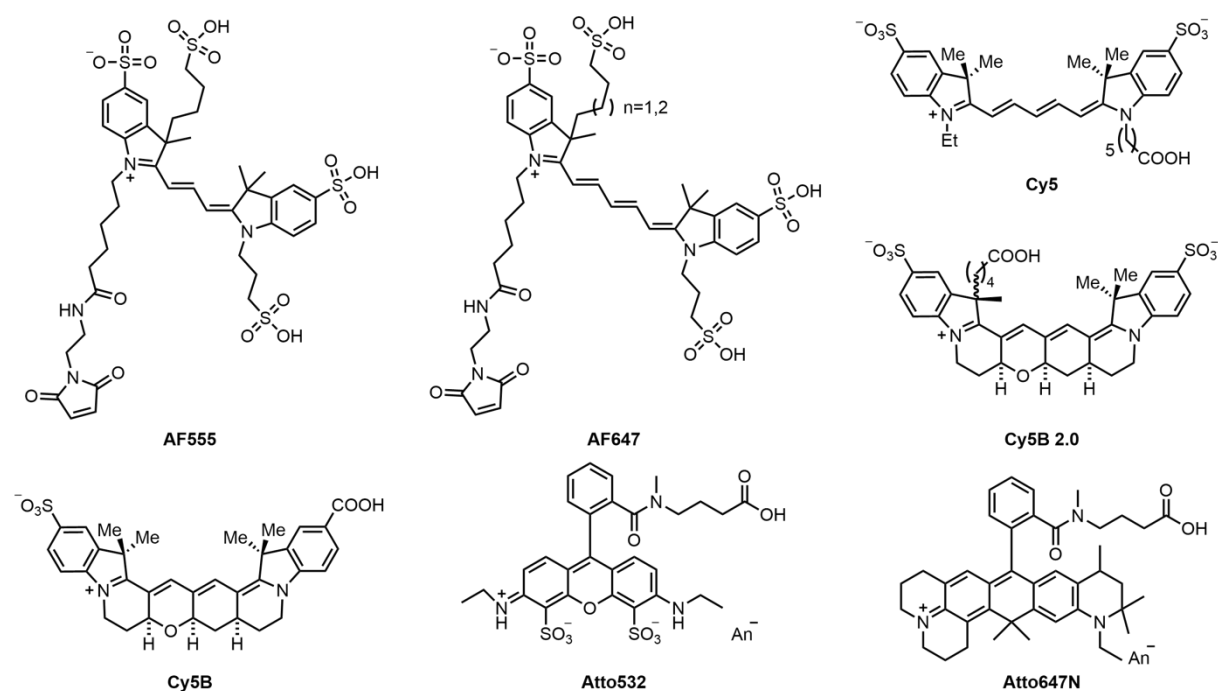
Figure 2.2 The structures of the fluorophores. Cy5 is the previous pentamethine cyanine and Cy5B is the evolution of restricted pentamethine variant.

This thesis mainly focuses on the popular polymethine-based cyanine fluorescent dyes Cy5B, Cy5B 2.0, AF555 and AF647 in comparison to rhodamines (Atto532) and carborhodamines (Atto647N and Atto643). The photon output of cyanine fluorophores is limited by the *trans-to-cis* photoisomerization. However, appending a ring system (Fig 2.2) to the pentamethine system hinders rotation around the central double bonds and with that improves the quantum yield and extend the fluorescence lifetime[13]. In chapter 4.1.3, I compare the photophysical properties of these new dyes against standards used in the field.

2.2.2 Bioconjugation of fluorophores

It is has become an established standard to attach fluorophores to target biomolecules using specific reactive groups. The thiol-maleimide reaction (Fig. 2.3) is a commonly used method for site-selective alteration of proteins via cysteine residues and was the primary method used for biolabeling in this thesis. As targets I used different double cysteine mutants of the substrate binding proteins (SBPs) MalE, SBD and GlnBP, which were stochastically labeled with two different dyes (the donor and acceptor, Fig. 2.3).
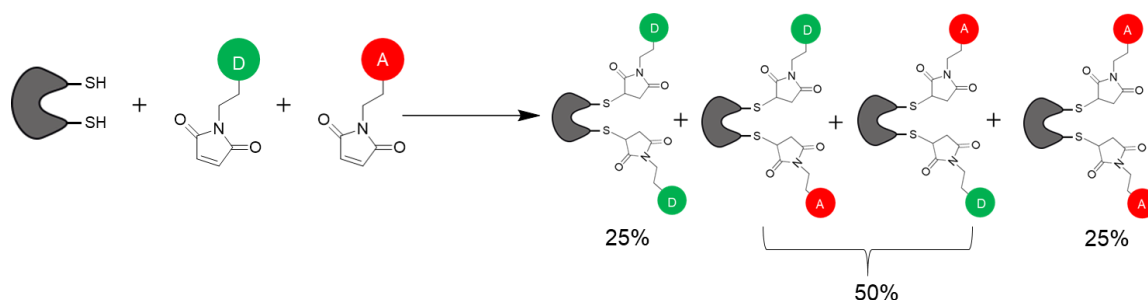
Figure 2.3 Schematic diagram of stochastic protein labelling via thiol-maleimide chemistry giving rise to mix of label compositions.

2.2.3   Photostablizing agents

As a result of frequent transitions between bright and dark fluorophores states (such as triplet states) "blinking" signals can be observed. Also, irreversible photochemical reactions, commonly known as photobleaching, describe pathways the lead to degradation of the dye structure. It is thus become common practice to quench such reactive states (triplet state) and prevent interactions with photodamaging chemicals to increase the photostability.

Blinking is mitigated by the fact that triplet oxygen can efficiently depopulate the triplet state of a fluorophore by generating the more energetic singlet oxygen species[17] (see also Fig. 2.1). While the depletion of triplet-states can be benefical the high reactivity of the resulting reactive-oxygen species can be the cause of photodamange of the dyes[18]. Therefore, oxygen is usually removed from aqueous buffer solutions to prevent photobleaching and preserve the stability and function of tagged molecules. Protocatechutic acid (PCA) and protocatechute-3,4-dioxygenase (PCD) [19] or glucose oxidase in combination with catalase (GOC)[20] are the two most frequent enzymatic oxygen scavenging systems, that consume oxygen in the enzymatic reactions for depletion from the buffer solution. However, in both cases, the substrate oxidation produces carboxylic acids, which can result in a continuous decrease in pH over time. An alternative is the combination of pyranose oxidase and catalase (POC) which does not change the (Figure 2.4). Since the triplet becomes longer lived in the absence of oxygen, it can be quenched by using a mixture of reducing and oxidizing chemicals to generate a radical ion through electron transfer (reducing and oxidizing system, ROXS) (Figure 2.1). Subsequently, this radical ion can be recovered through the complementary redox reaction [21]. However, since this thesis focuses on solution-based measurements with short observation times < milliseconds, photo-stabilizer additives are usually not required.
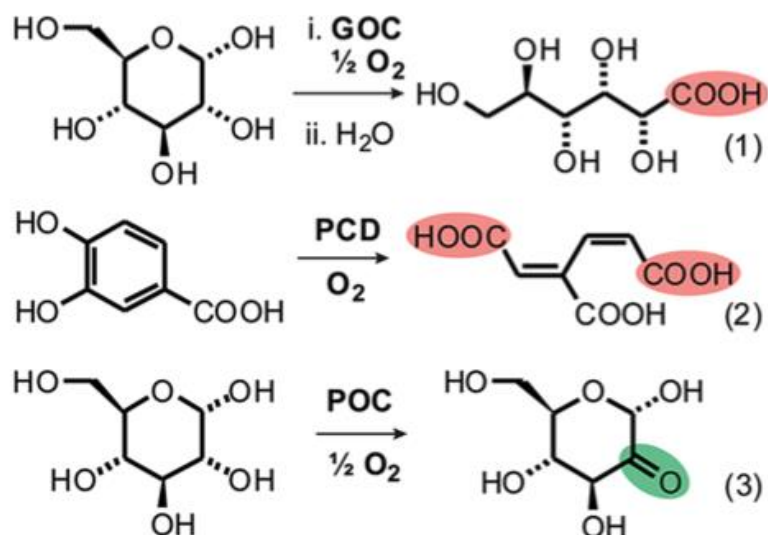
Figure 2.4. The basis of oxygen removal using enzymatic reactions of GOC, PCD and POC[22].

2.3 Förster resonance energy transfer (FRET)

When two chromophores (or fluorophores) come into proximity, energy can be transferred from the excited donor molecule to a ground state acceptor molecule via dipolar coupling as shown in Figure 2.5. The phenomenon of Förster Resonance Energy Transfer (FRET) describes such a non-radiative energy exchange mechanism that relies on dipole-dipole interactions between the donor and acceptor. This phenomenon is used within this thesis for study of conformational dynamics of proteins that allow to characterize their binding mechanism.

For FRET to occur, one requirement is the overlap of the emission spectrum of the donor with the absorption spectrum of the acceptor (iso-energetic transitions). The FRET fluorophore 'couple' can serve as a distant ruler on the 3-10 nm scale and, therefore, can be utilized to detect conformational changes or distances in biological macromolecules (intramolecular FRET). Detecting the dynamic interaction between two molecules is possible when FRET dyes are placed on each of the interacting entities (intermolecular FRET). The rate of energy transfer,

denoted by k_T, is highly sensitive to inter-fluorophore distance with a steep distance dependence:

$$k_T = \frac{1}{\tau_{D(0)}} \left(\frac{R_0}{R}\right)^6 \tag{1}$$

In eqn. 1 the fluorescence lifetime of the donor in absence of the acceptor is $\tau_{D(0)}$, and the Förster radius R_0.
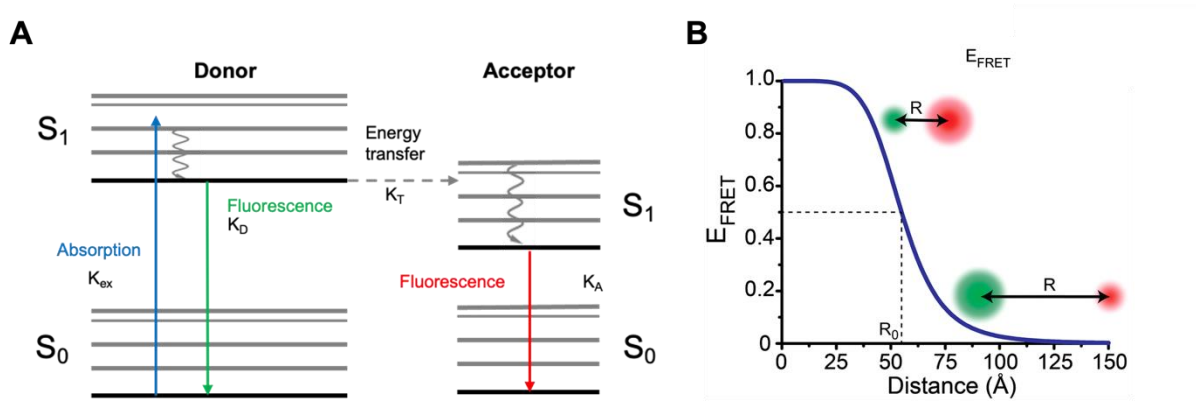
Figure 2.5. (A) An illustration of FRET between a donor dye and an acceptor dye in a Jablonski diagram. S_0: singlet ground state, S_1: first excited singlet state, k_{ex}: excitation rate, k_D and k_A: emission rates of the donor and acceptor fluorophores, respectively, and k_T the rate of the energy transfer. (B) A plot of the FRET efficiency as a function of the distance between a donor and an acceptor.

The energy transfer efficiency is calculated as the ratio of the transfer rate in comparison to the total decay rate of the donor in the presence of the acceptor.

$$E = \frac{k_T}{k_T + \tau_D^{-1}} \tag{2}$$

Which can be rewritten, using equation (1) as

$$E = \frac{R_0^6}{R_0^6 + R^6} = \frac{1}{1 + \left(\frac{R}{R_0}\right)^6} \tag{3}$$

The inter-dye distance with a 50% energy transfer efficiency is known as the Föster radius R_0, and is given by,

$$R_0^6 = \frac{9000(ln10)k^2\phi_D}{128\pi^5 N_A n^4} J(\lambda)$$

(4)

where k^2 is a geometric factor that depends on the relative orientation of the acceptor and donor transition dipoles, ϕ_D is the quantum yield of the donor, N_A is Avogadro's Number, n is the refractive index of the medium, and $J(\lambda)$ is the overlap integral of the acceptor's absorption and the donor's emission spectrum. $J(\lambda)$ depends on the normalized emission spectrum of the donor $\int_0^\infty F_D(\lambda)d\lambda = 1$ and the absorption spectrum of the acceptor expressed in terms of the extinction coefficient $\epsilon_A(\lambda)$:

$$J(\lambda) = \int_0^\infty F_D(\lambda)\epsilon_A(\lambda)\lambda^4 d\lambda$$

(5)

The orientation factor κ^2 is calculated as

$$\kappa^2 = (\cos\theta_T - 3\cos\theta_D \cos\theta_A)^2$$

(6)

Given the angle between the donor emission dipole moment and the acceptor absorption dipole moment, θ_T , θ_D and θ_A are the angles between the corresponding dipole and the vector linking the donor and acceptor. k^2 can take values ranging from 0 to 4. k^2 is commonly averaged across all potential angles to get a value of 2/3.

2.4 Overview of substrate binding proteins (SBPs)

The SBP model proteins used within this thesis are part of ATP-binding cassette (ABC) transporters (Figure 2.6, left). These ubiquitous proteins uses the energy supplied by ATP hydrolysis to allow the unidirectional trans-bilayer transit of a number of sub-states [23]. In these, two transmembrane domains (TMDs) constitute the translocation pathway in the translocator unit, while two

cytoplasmic nucleotide-binding domains (NBDs) bind and hydrolyze ATP to power transports.
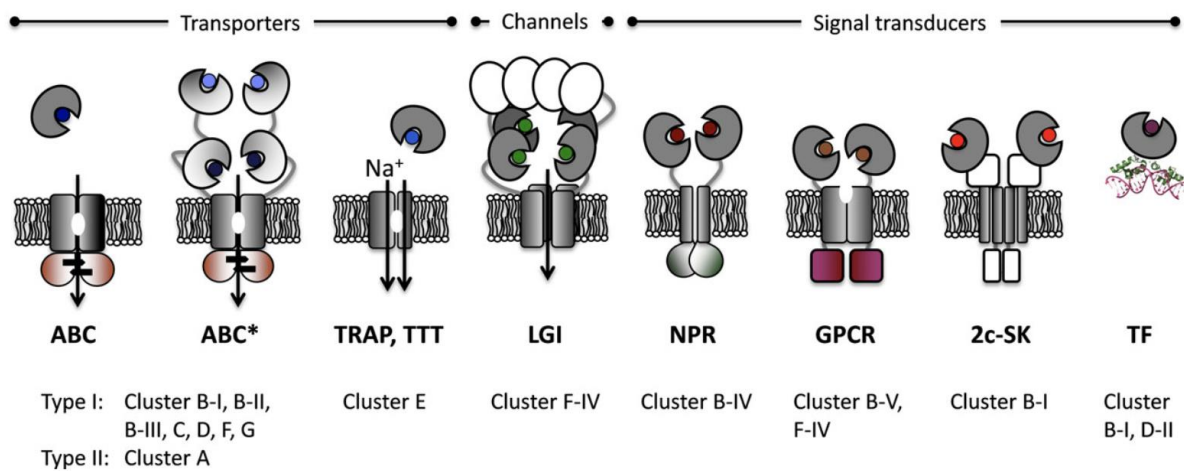
Figure 2.6 Schematic overview of SBP-dependent (membrane) proteins [24]. ABC, an ABC importer with the SBP in the periplasm, ABC*, an ABC importer with two SBDs fused to the TMD, yielding four SBDs per transporter complex.

Substrate-binding proteins (SBPs) and substrate-binding domains (SBDs) are a type of protein which interact with membrane protein complexes to facilitate solute uptake or signal transduction[23, 25, 26], which were originally discovered to be associated with prokaryotic ATP-binding cassette (ABC)-transporters. SBPs bind their ligands with high affinity and deliver them to the translocator (the TMDs), where the substrate is released into the translocation pore upon ATP binding and hydrolysis in the NBDs[27]. The systems are valuable biophysical model systems since they are soluble and robust to handle and feature a well-understood and well-characterized structure with ligand-free open and ligand-bound closed conformations (see more details below).

2.4.1 Maltose Binding Protein (MalE)

The periplasmic substrate binding protein (SBP), MalE [28], from *E.coli*, is a well characterized component of the maltose input system [29, 30]. It is assumed that

MalE is required for maltose uptake in vivo, since the knockout strains on MalE cannot grow on maltose even at external sugar concentrations of 25 mM [31]. Furthermore, in addition to maltose, MalE also can bind several maltodextrins [12, 32, 33] with affinity in the micromolar range. Crystal structure studies have demonstrated that MalE is composed of two globular lobes, the N-terminal domain and C-terminal domain, which form a pocket to bind with substrate at the interface [34]. Substate binding induces bending of the interface of the two lobes. Therefore, the MalE adopts one apo (open) state in the absence of maltose and a holo (closed) state in the presence of maltose (Figure 2.7). The resemblance of the process to the Venus flytrap plant capturing its prey has led it to be known as the Venus flytrap mechanism.
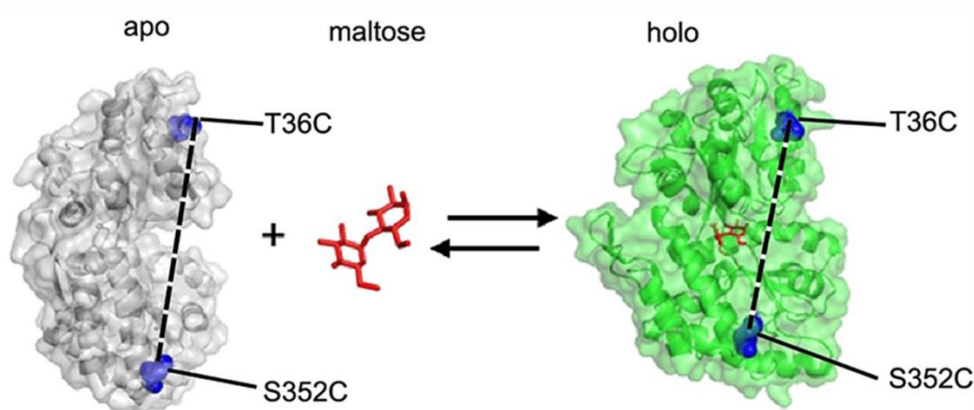
Fig. 2.7 Crystal structure of MalE in apo (grey, pdb file:1omp) and holo (green, pdb file:1anf) where the labeling positions Thr36Cys and Ser352Cys are indicated in blue.

For studies of conformational dynamics of MalE, we used the double-cysteine variant Thr36Cys-Ser352Cys. The protein was designed to monitor the switching of the apo (open) state in the absence of substrates and a holo (closed) state in the presence of substrates using smFRET measurements[12]. Furthermore, this variant was selected to benchmark the conformationally restrained sulfonated cyanine dyes against commonly used fluorescent dye combinations (donor fluorophore AF555 with acceptors AF647 and Atto647N) [13].

2.4.2　Glutamine Binding Protein (GlnBP)

E.coli GlnBP is another substrate binding protein (SBP), which can specifically bind *L*-glutamine with sub-micromolar affinity [35, 36] and *L*-arginine with millimolar affinity [37]. Also GlnBP, similar to MalE, belongs to a prokaryotic ABC transporter[34]. GlnBP contains a single polypeptide chain of 226 residues with a tertiary structure of approximately 35% α-helices and 37% β-sheets[38]. Crystal structure studies demonstrated that GlnBP adopts two conformational states, an open (apo) state [2] in the absence of glutamine and a closed (holo) state [39] in the presence of glutamine (Fig. 2.8A and 2.8B, respectively). It is monomeric and consists of two globular domains, i.e., the small domain (residues 90–180) and the large domain (residues 5–84 and 186–224), linked by the hinge region (residues 85–89 and 181–185), and the ligand binds at the domain surface.
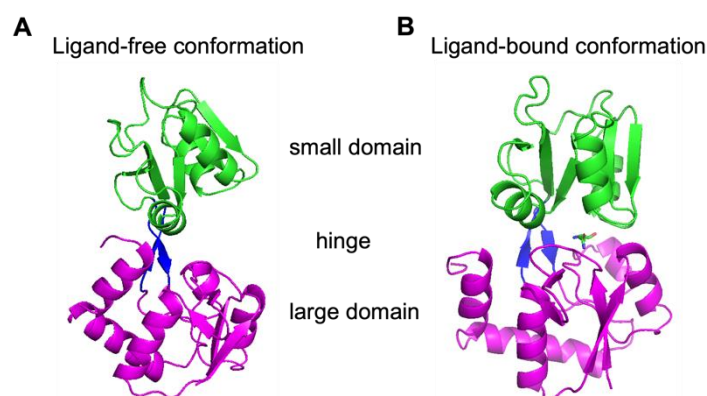
Fig. 2.8 Crystal structures simulation of GlnBP. (A) The ligand-free conformation of GlnBP (PDB file: 1GGG) and (B) the ligand-bound conformation of GlnBP (PDB file: 1WDN). The green, blue, and magenta colored structure represent the small domain, the hinge region, and the large domain, respectively.

Conformational dynamics in GlnBP play an important role in the regulation of its biological function, i.e., membrane transport[40]. GlnBP was intensely studied and its conformational changes were characterized by smFRET techniques

(Figure 2.9A), NMR residual-dipolar coupling (RDC) techniques[41] (Figure 2.9B), MD simulations [38, 42], (Figure 2.9C) and MSMs [43] (Figure 2.9D). Results from these studies were interpreted such that GlnBP could adopt four different conformational states both in the ligand-free (open) state [41] and the ligand-bound (closed) state [44], yet based on insufficient support. Based on these findings the authors suggested GlnBP to bind L-glutamine through two ligand binding mechanisms, i.e. conformational selection and induced-fit mechanism[43].
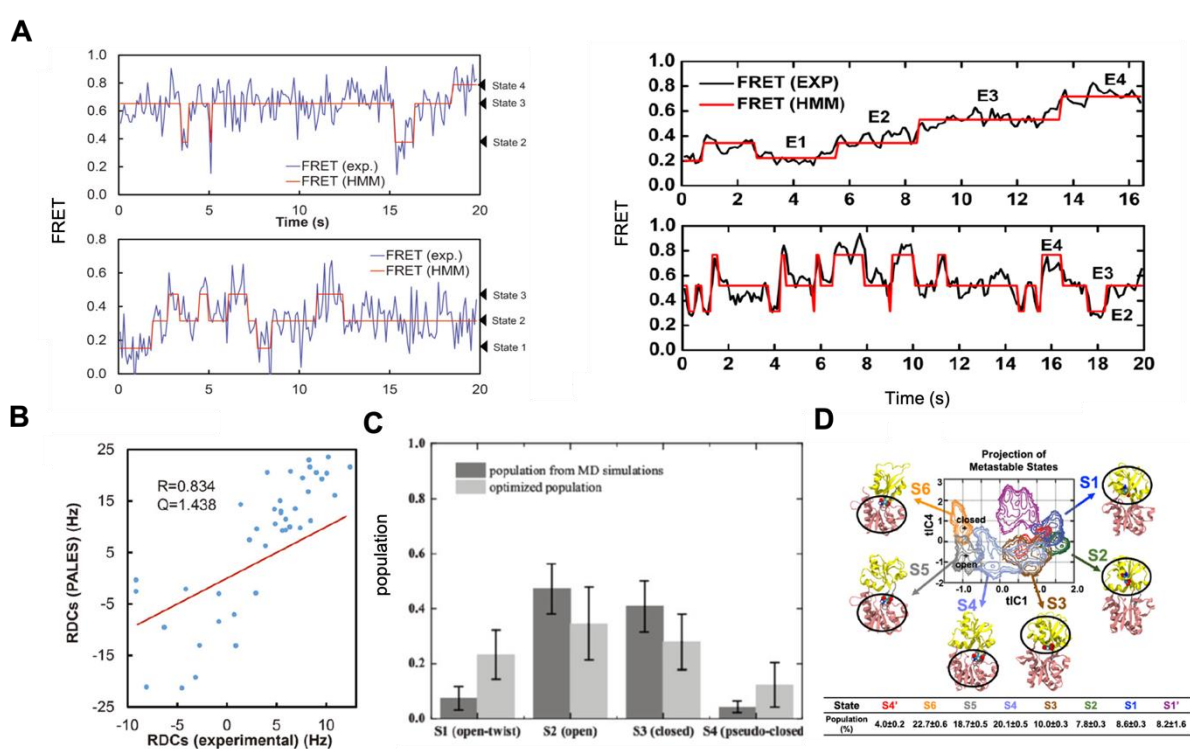
Fig. 2.9 (A) smFRET results of GlnBP on apo state (left) and closed state (right). (B) Agreement between the apo-GlnBP experimental RDCs and the RDCs predicted based on the open crystal structure. (C) Populations of the four macrostates derived from MD simulations and optimized populations. (D) Projection of metastable states of GlnBP using MSMs analysis.

SBPs can bind its specific substrate with IF or CS mechanism. IF assume that a ligand binds a highly populated open conformation of a protein, followed by a structural adjustment to a ligand-bound, fully closed state. In CS assume that a

ligand selectively binds a weakly populated single substate in the ensemble of conformations, and no further conformational changes occurs after ligand binding.

According to the studies, they hypothesized that GlnBP undergoes pronounced conformational changes both in the absence and in the presence of substrate, involving a total of four (up to six) conformational states. Based on this, the authors speculated that GlnBP binds ligand through a combination of CS and IF. These conclusions stand in strong contrast to previous research on structurally related SBD1 and SBD2 [12, 45]. Furthermore, Kooshapur[46] and co-workers did not find evidence for conformational dynamics of GlnBP using an NMR approach. Additionally, MD simulation of SBD2 indicate that GlnBP cannot form a closed state conformation in a ligand-free condition[47]. These findings instead conclude that the protein binds with ligand to form a closed state following the induced-fit mechanism.

3 Materials and Methods

3.1 Materials

3.1.1 Chemicals

Chemicals	Producer
Guanidine Hydrochloride	Sigma Aldrich, Taufkirchen, Germany
1,4-Dithiothreit (DTT)	Carl Roth, Karlsruhe, Germany
SnakeSkin TM Dialysis Tubing	Thermo Fisher Scientific, MA, USA
Ni^{2+}-Sepharose resin	GE Healthcare, USA
Imidazole, $\geq$99%	Carl Roth, Karlsruhe, Germany
Isopropyl-β-D-1-thiogalactopyranose (IPTG)	Carl Roth, Karlsruhe, Germany
Kanamycin	Carl Roth, Karlsruhe, Germany
L-glutamine	Merck, Darmstadt, Germany
L-Arginine	Carl Roth, Karlsruhe, Germany
AF555	Jena Bioscience, Germany
AF647	Jena Bioscience, Germany
Atto532	Attotech, Germany
Atto643	Attotech, Germany
mPEG3400-silane	abcr. Gute Chemie, Germany
biotin-PEG3400-silane	abcr. Gute Chemie, Germany
Biotin-NTA	Biotium, USA
Streptavidin	Carl Roth, Karlsruhe, Germany
Pyranose oxidase	Sigma Aldrich, Taufkirchen, Germany
Catalase	Sigma Aldrich, Taufkirchen, Germany
Glucose	Sigma Aldrich, Taufkirchen, Germany
Potassium hydroxide	Honeywell, Germany
Acetone	Carl Roth, Karlsruhe, Germany

3.1.2 Buffers and solutions

Buffer	Company or ingredients	Final concentration
Tris buffer, pH 8.0	Carl Roth, Karlsruhe, Germany	
PP1	Tris buffer, pH 8.0 (1M)	50 mM (5 ml)
	KCl (2.5 M)	1 M (40 ml)
	Imidazole (1 M)	10 mM (1 ml)
	Glycerol (99%)	10% (10 ml)
	Water	(44 ml)
		Total 100 ml
PP2	Tris buffer, pH 8.0 (1M)	50 mM (5 ml)
	KCl (2.5 M)	1 M (2 ml)
	Imidazole (1 M)	10 mM (2 ml)
	Glycerol (99%)	10% (10 ml)
	Water	(81 ml)
		Total 100 ml
PP3	Tris buffer, pH 8.0 (1M)	50 mM (5 ml)
	KCl (2.5 M)	1 M (2 ml)
	Imidazole (1 M)	10 mM (25 ml)
	Glycerol (99%)	10% (10 ml)
	Water	(58 ml)
		Total 100 ml
PP4	Tris buffer, pH 8.0 (1M)	50 mM (5 ml)
	KCl (2.5 M)	50 mM (2 ml)
	Water	(93 ml)
		Total 100 ml

Buffer	Company or ingredients	Final concentration o
PP5	Tris buffer, pH 8.0 (1M)	50 mM (5 ml)
	KCl (2.5 M)	50 mM (2 ml)
	Glycerol (99%)	50% (50 ml)
	Water	43 ml
		Total 100 ml
Anode buffer	Tris-HCl (1M)	250 mM (25 ml)
	Water	(75 ml)
Cathode buffer	Tris (1M)	100 mM (10 ml)
	Tricine (1M)	100 mM (10 ml)
	SDS (1%)	0.1% (100 μl)
	Water	(79.9 ml)

3.1.3 Consumables

Materials	Company
GeneJET Plasmid miniprep kit	Thermo Fisher Scientific Inc.
Microscope cover glasses, 24x60mm	Paul Marienfeld GmbH
Poly-Prep Chromatography Columns	BIO-RAD Laboratories
Superdex 75 Increase 10/300 GL column (for ÄKTA)	Cytiva Life Sciences
vivaspin6 centrifugal concentrator 10,000 MWCO	Sartorius
vivaspin20 centrifugal concentrator 10,000 MWCO	Sartorius

3.2 Methods

3.2.1 Protein labelling for ALEX Spectroscopy

The MalE double cysteine variant was obtained as described before.[12] The cysteines were stochastically labeled with the maleimide derivatives of the donor dye (AF555, Jena Bioscience, Germany) and acceptor dyes (AF647 (Jena Bioscience, Germany), Atto647N (ATTO-TECH, Germany), and Cy5B and Cy5B-trisulfo). For this, the His-tagged protein was first incubated in 10 mM DTT in labeling buffer A (50mM TRIS-HCl, 50mM KCl, pH 7.4) for 30 min to reduce all oxidized cysteine residues. Subsequently, the protein was diluted 10 times with buffer A and immobilized on a Ni Sepharose 6 Fast Flow resin (GE Healthcare), after the resin was washed extensively with milliQ water followed by buffer A. To remove the DTT from the immobilized protein, the resin was washed with 2 mL of buffer A. The protein was left on the resin and incubated overnight at 4°C with 5-10 times molar excess of each fluorophore (donor and one of the acceptors) compared to protein in buffer A. Subsequently, the unreacted fluorophores were removed by washing the resin with 6 mL of buffer A. Bound proteins were eluted with 800 μl of elution buffer (50mM TRIS-HCl, 50mM KCl, 400mM Imidazole, pH7.4) The labeled protein was further purified by size-exclusion chromatography (ÄKTA pure, Superdex 75 Increase 10/300 GL, GE Healthcare) to eliminate remaining fluorophores and remove soluble aggregates. The same labelling method was used for GlnBP.

3.2.2 Protein expression and purification

Two GlnBP double cysteine variants were generated by site-directed mutagenesis, allowing the insertion of two cysteine residues into GlnBP at positions (V111C – G192C) and (T59C – T130C), separately. *Escherichia coli* BL21-pLysS cells were freshly transformed with the plasmid carrying the coding sequence for GlnBP WT or a GlnBP variant and grown in 2 L LB medium (100 mg/mL

Kanamycin and 50 mg/mL chloramphenicol) at 37 °C under aerobic conditions. At an OD_{600nm} of 0.6-0.8, overexpression of the proteins of interest was induced upon addition of 1mM IPTG to the culture media. The cells were further grown for 1.5-2 hours after induction and then harvested by centrifugation for 20 minutes at 1529 g (Beckman, JA10) at 4°C. All subsequent operations were carried out at 4 °C, and all solutions were stored at 4 °C. Cell pellets from 2L culture were collected in a 50 mL falcon and resuspended in buffer A (50 mM Tris-HCl, pH 8.0, 1 M KCl, 10 mM imidazole, 10% glycerol) with 1 mM dithiothreitol (DTT). At 4°C, the falcon was gently shaken overnight.

Cells were disrupted by sonication (Branson tip sonication; amplitude: 25%; 10 min; 0.5 s on/off pulses; temperature was kept cold using an ice-water bath). Centrifugation was used to fractionate the cell lysate (at 4°C for 30 minutes at 4416 g, Eppendorf, Centrifuge 5804 R) and at 4°C for 1 hour for ultracentrifugation (70658 g, Beckman, Type 70Ti) in vacuum), and the pellet was discarded. The protein was purified by affinity chromatography using the Ni^{2+}-Sepharose fast flow resin (GE Healthcare), pre-equilibrated with 10 column volumes of buffer A containing 1 mM DTT and gravity loaded with the supernatant from the preceding ultra-centrifugation step. The resin-bound protein was washed with 10 column volumes of buffer A containing 1 mM DTT, followed by buffer B containing 1 mM DTT (50 mM Tris-HCl, pH 8,0, KCl 50 mM, imidazole 20 mM, glycerol 10%), and finally eluted in buffer C (50 mM Tris-HCl, pH 8.0, KCl 50 mM, imidazole 250 mM, glycerol 10%) with 1 mM DTT. The eluted sample was concentrated (Vivaspin6 columns, 10 KDa MWCO, 6 mg/mL), dialyzed against PBS buffer supplemented with 1 mM DTT, and stirred gently at 4°C overnight. SDS-PAGE was used to quantify the yield of protein overexpression and purification (Coomassie staining). The absorbance at 280 nm was used to estimate the protein concentration (knowing the molar extinction coefficient of GlnBP ~25,900 M^{-1} cm^{-1}). The protein was then splitted into aliquots and kept at a temperature of -20 °C. All proteins were further purified using size-

exclusion chromatography (ÄKTA pure system, Superdex 75 Increase 10/300 GL, GE Healthcare). The purified protein was splitted into aliquots and stored at -80°C prior to the measurements.

3.2.3   Unfolding and refolding process of GlnBP

The stock concentrations of GlnBP variants were estimated at about 6 mg/mL. Each GlnBP variant was thawed from -80°C, then the protein was diluted to a final concentration of 3-4 μM (final volume of ~20 mL) in the unfolding buffer (PBS buffer) containing 6 M guanidine hydrochloride (GdnHCl). Subsequently, the solution was incubated for 3 h under gentle stirring at ambient temperature. Next, the unfolded GlnBP variants were centrifuged (3046 g, 30 min at 4°C) to remove insoluble aggregates which could act as nuclei to trigger aggregation during refolding process. A Snakeskin TM dialysis membrane was prepared (pre-cooled at 4°C and soaked in refolding buffer - PBS buffer with 1mM DTT, pH 7.4 - for 2 min). The GlnBP variants were transferred into the dialysis tubing which were sealed tightly afterwards by double-knots and clips at each end. The unfolded GlnBP variant was refolded by a two-step dialysis, in the presence of a total 200-fold excess of refolding buffer. First, each protein was dialyzed against 2 L refolding buffer overnight under gentle stirring at 4°C. Then, buffer was exchanged with additional 2 L refolding buffer for another day at 4°C. The refolded protein was then concentrated from 20 mL to final 500 μL (Vivaspin 10kDa MWCO; 3000g × 15 min at 4°C) and further purified by size-exclusion chromatography (ÄKTA pure system, Superdex-75 Increase 10/300 GL, GE Healthcare). The unfolding and refolding process for GlnBP WT was conducted under the same conditions as described for the GlnBP variants.

3.2.4 Isothermal titration calorimetry (ITC).

The ITC measurements were performed in a MicroCal PEAQ-ITC isothermal titration calorimeter (Malvern Instruments). The prediction ITC software "MicroCal PEAQ-ITC Control" was employed for designing and conducting the experiments. Once the Kd value and the binding stoichiometry (N) were assigned as predefined values, the concentration of both the protein and the titrant (ligand) stock solutions could be calculated by the "design-experiment" function on the software to get an optimal sigmoidal one-site binding curve. GlnBP concentration was assessed using the Nanophotometer (N60 Touch, Implen GmbH) with at least three reading repeats to get accurate determinations of concentration values.

For all ITC measurements, the temperature was set at 25°C with stirring speed at 750 rev / min. The GlnBPs solution (10 µM in PBS buffer pH 7.4, 300 µL) was manually loaded into the sample cell. The titrant (L-Glutamine, 100 µM in PBS buffer, pH 7.4) was automatically loaded into the titration syringe and injected in the sample cell with a titration speed of 2 µL every 150 second and a total of 19 injections. As a control experiment, L-Glutamine was titrated into the sample cell containing PBS buffer without GlnBPs. All the titration data were analysed using the MicroCal PEAQ-ITC Analysis Software.

3.2.5 µsALEX experiments.

Single-molecule µs-ALEX experiments were carried out at room temperature on a custom-built confocal microscope (Figure 3.1). In short, alternating excitation light (50 µs period) was provided by two diode lasers operating at 532 nm (OBIS 532-100-LS, Coherent, USA) and 640 nm (OBIS 640- 100-LX, Coherent, USA). Both lasers were combined by coupling them into a polarization maintaining single-mode fiber (P3-488PM-FC-2, Thorlabs, USA) and subsequently guided into the microscope objective (UplanSApo 60X/1.20W, Olympus, Germany) via a dual-edge dichroic mirror (ZT532/640rpc, Chroma, USA). Fluorescence light

was collected by the same objective, focused onto a 50 μm pinhole and separated into two spectral channels (donor and acceptor) by a dichroic beam splitter (H643 LPXR, AHF, Germany). Fluorescence emission was collected by two avalanche photodiodes (SPCM-AQRH-64, Excelitas) after additional filtering (donor channel: BrightLine HC 582/75 and acceptor channel: Longpass 647 LP Edge Basic, both from Semrock, USA). The detector outputs were recorded via an NI-Card (PCI-6602, National Instruments, USA) using a custom-written LabView program.
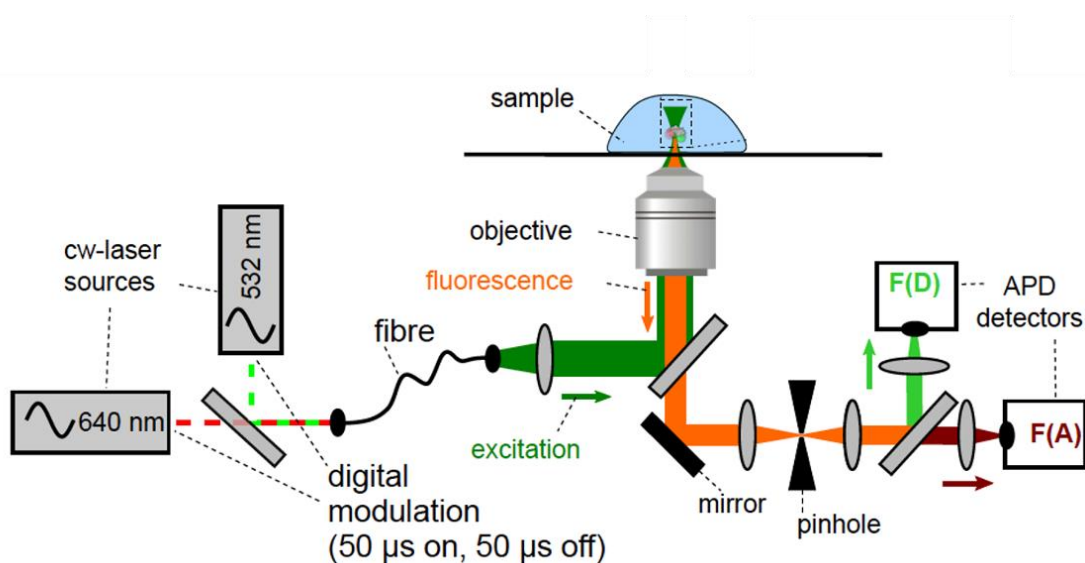
Figure 3.1. Schematic of an ALEX setup with two alternating laser sources that are focused in the solution above the coverslip and steered into the objective. The same objective is used to collect the emitted light, and a dichroic mirror is used to separate it from the excitation light. Before being focussed onto an APD chip, the emitted light is spectrally divided and spatially filtered by a pinhole. (from Christian Gebhardt Ph.D thesis)

Data analysis was performed using a home written software package as described in[48]. Three relevant photon streams were extracted from the recorded data based on the alternation period, corresponding to donor-based donor emission F(DD), donor-based acceptor emission F(DA) and acceptor-based acceptor emission F(AA). Bursts from single-molecules were identified using published procedures[49] based on an all-photon-burst-search algorithm with a threshold of

15, a time window of 500 µs and a minimum total photon number (F(DD)+D(DA)+F(AA)) of 150, unless stated otherwise in the figure caption.

For each fluorescence burst, the stoichiometries S* and apparent FRET efficiencies E* were calculated and then presented for all bursts yielding a two-dimensional (2D) histogram. Uncorrected apparent FRET efficiency E* monitors the proximity between the two fluorophores and is calculated according to E* = F(DA)/(F(DD)+F(DA)). Stoichiometry S* is defined as the ratio between the overall fluorescence intensity during the green excitation period over the total fluorescence intensity during both green and red periods and describes the ratio of donor-to-acceptor fluorophores in the sample: S*=(F(DD)+F(DA)/(F(DD)+F(DA)+F(AA)). Collecting the E*/S* values of all detected bursts into a 2D E*/S* histogram yielded subpopulations that can be separated according to their E*- and S*-values. The 2D histograms were fitted using a 2D gaussian function, yielding the mean apparent FRET efficiency and its standard deviation or width of the distribution. Photon-counting histograms (PCHs) were obtained using similar thresholds as for the 2D E*/S* histograms.

The MalE variant was labelled with different fluorophore pairs (AF555/Atto647N, AF555/AF647, AF555/Cy5B, AF555/Cy5B 2.0) and then purified by SEC. The selected elution fractions were used without further treatment for µs-ALEX experiments. The refolded GlnBP(111-192) and GlnBP(59-130) variants were labelled with commercial maleimide derivatives of AF555/AF647 or Atto532/643[50], and then purified by SEC. The chromatogram of refolded GlnBP(111-192) was labelled with AF555/AF647, and those of all other variants and dye labelling combinations are displayed in Figure 4.13. The selected elution fractions were used without further treatment for µs-ALEX experiments. ALEX experiments were carried out at room temperature using 25–50 pM of double-labelled GlnBP protein in PBS buffer (pH7.4). Titration experiments were done by adding specific concentrations of ligand (glutamine) to the buffer. In general,

the diode laser at 532 nm was operated at 60 µW and the 640 nm at 25 µW (measured at the back aperture of the objective), unless stated otherwise.

3.2.6 Analysis of "within-burst" FRET dynamcis.

Analysis of within-burst FRET-dynamics via mpH²MM was conducted as described previously[51]. In short, FRET Bursts[52] was used for detecting single-molecule photon bursts using the dual channel burst search[49] AND-gate algorithm with a sliding window of m=10 photons searching for instances with an instantaneous photon rate of at least F=6 times the background rate. Afterwards, bursts were filtered to have at least 50 photons originating from donor excitation and 50 photons originating from acceptor excitation. The photon stream was then divided into bursts, and a shift was applied to acceptor excitation originating photons stream so that their arrival time range overlap with that of donor excitation originating photon streams.

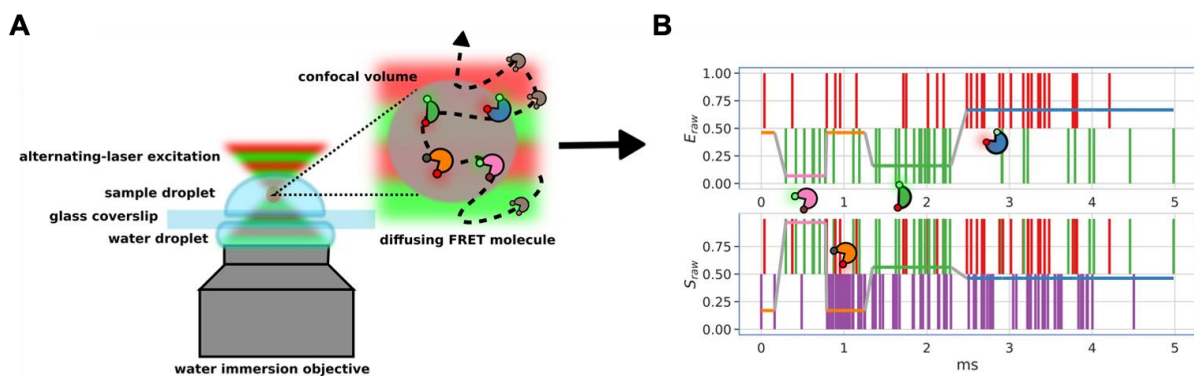Figure 3.2. (A) Confocal microscope setup with inset illustrating the diffusive trajectory of a single molecule in and out of the confocal volume, undergoing conformational and photophysical changes, producing, (B) a photon time trace; photons represented by vertical bars, and the most likely state path according to the Viterbi algorithm overlayed as horizontal colored line. The figure was adapted from ref. [51].

Optimizing for larger numbers of states ceased once the ICL ceased to decrease between successively larger state models. Optimized models were manually examined, and the optimal state model selected considering the ICL and the reasonableness of the model given prior knowledge based on transition rates and the E* and S* values of the states. After selection of the most-likely state model, the corresponding most-likely state-path determined by the *Viterbi* algorithm was used to segment bursts into dwells and to classify burst by which states were present within each burst.

3.2.7   smFRET with MFD-PIE and burst-wise FCS analysis.

Similar as for μsALEX, solution-based smFRET experiments via MFD-PIE were conducted as described previously.[53] Briefly, 100 pM of GlnBP labelled with Atto532 and Atto643 was placed on a BSA-passivated LabTek chamber and examined for 2-hours. The sample was excited with 532 nm and 640 nm pulsed lasers with a repetition rate of 26.6 MHz and 45 and 23 μW laser powers (measured on the objective), respectively. The solution-based smFRET experiments were performed by Zhongying Han and Ecenaz Bilgen on a home-built dual-colour confocal microscope in the group of Prof. Don Lamb (LMU Chemistry). The setup combines multiparameter fluorescence detection (MFD) with pulsed interleaved excitation (PIE).[54] A schematic of the two-color PIE-MFD setup was obtained from the PhD thesis of Kira Bartnik.
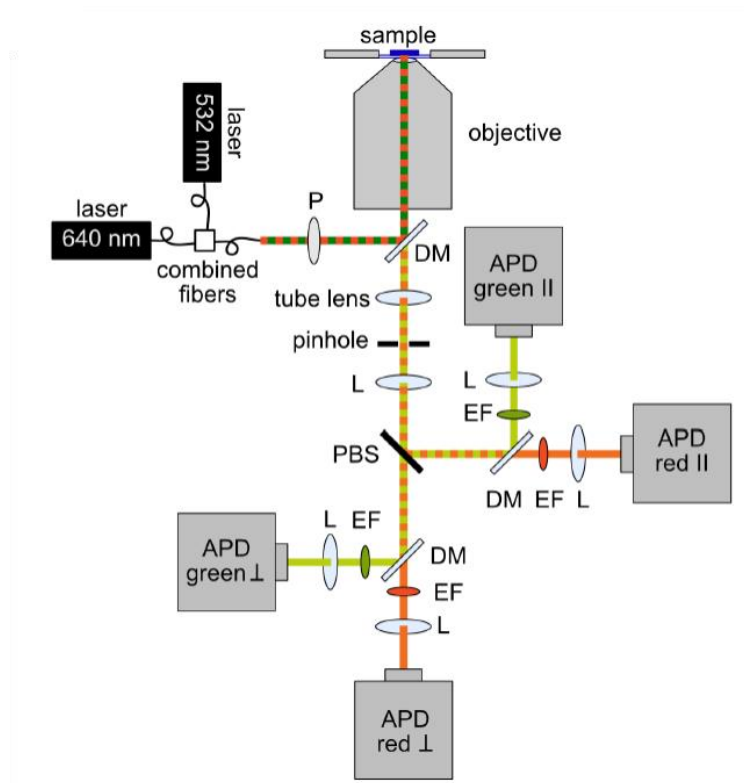
Figure 3.3. A schematic representation of the two-color PIE-MFD confocal setup with an infinity corrected objective and a tube lens to focus the fluorescence signal onto the pinhole. P: polarizer, DM: dichroic mirror, L: lens, PBS: polarizing beam splitter, EF: emission filter, and APD: avalanche photodiode for parallel (∥) and perpendicular (⊥) detection.

For pulsed-interleaved excitation, laser lines at 532 nm (PicoTA 530, Toptica, Munich, Germany) and 640 nm (LDH-D-C-640, Picoquant, Berlin, Germany) are coupled into single-mode fibers (Schäfter+Kirchhoff, Hamburg, Germany), combined through a T-geometry wavelength division multiplexer (WDM-12P-111-532/647-3.57125-PPP-50-3A3A3A-3-1,1,2, OZ Optics, Carp, Canada) and collimated (60FC-4-RGB11-47, Schäfter+Kirchhoff). The pulsed lasers are operated at a repetition rate of f = 26.67 MHz (leading to pulses of 37.5 ns) with a delay of Δt = 18 ns. The laser light is cleaned by a Glan-Thompson polarizer (GTHM polarizer, Thorlabs, Dachau, Germany) and focused into the sample by a 60x water immersion objective (Plan Apo IR 60x/1.27 WI, Nikon, Düsseldorf, Germany). Laser powers before the objective of 100 μW were typically used. For

the simultaneous detection of various fluorescence parameters like intensity, lifetime and anisotropy, fluorescence is collected by the same objective, seperated by a dichroic mirror (DualLine z532/635, AHF Analysentechnik, Tübingen, Germany), focused through a pinhole with a diameter of 75 μm, and parallel and perpendicular components seperated by a polarizing beam splitter (05FC16PB.3, Newport, Darmstadt, Germany). For both parallel and perpendicular signals, fluorescence is spectrally split by a dichroic mirror (640DCXR, AHF Analysentechnik) and cleaned by emission filters (Brightline HQ582/75 for the green signal and Brightline HQ700/75 for the red signal, both from AHF Analysentechnik). Signals are detected on four single-photon counting avalanche photodiodes (APDs, SPCM-AQR, Perkin Elmer, Hamburg, Germany), each of which is connected to a seperate time-correlated single photon counting (TCSPC) card (SPC-154, Becker & Hickel GmbH, Berlin, Germany).

With MFD-PIE, it is possible extract FRET efficiency, stoichiometry, fluorescence lifetime and anisotropy information from each single-molecule burst. Correction factors including direct acceptor excitation (α), spectral crosstalk (β) and detection correction factor (γ) are also accounted for reporting accurate the FRET efficiency values[55]. The accurate FRET efficiency (E) can be determined from:

$$E = \frac{F_{GR} - \alpha F_{RR} - \beta F_{GG}}{F_{GR} - \alpha F_{RR} - \beta F_{GG} + \gamma F_{GG}}$$

Where F_{GG}, F_{GR} and F_{RR} are background corrected fluorescence signals detected in green/ donor (G), red/acceptor (R) after donor excitation and acceptor channels, respectively.

Alternatively, the use of pico-second pulsed lasers and time correlated single photon counting (TCSPC) electronics enable calculating FRET efficiencies from the quenching of the donor in presence in acceptor. According to the formula:

$$E = 1 - \frac{\tau_{D(A)}}{\tau_{D(0)}}$$

$\tau_{D(A)}$ is the fluorescence lifetime of the donor in presence of acceptor and $\tau_{D(0)}$ is the fluorescence lifetime of the donor only species. Static species can be observed on the static FRET line which is a linear relation between E and $\tau_{D(A)}$. Sub-millisecond conformational dynamics can also be judged by observing the right-shifted populations from the static FRET line.

Burst-wise FCS analysis is an alternative approach to observe sub-millisecond conformational dynamics. In this approach, donor (DD) and acceptor (AA) signals detected from single-molecule events are cross-correlated. Thus, fluctuations in the FRET efficiencies appear as anti-correlated signal in the cross-correlation function. A time window of 50 ms was applied around each burst for Burst-wise FCS so that other single-molecule events falling into the time window are eliminated to obtain correlation functions that are specific to the selected bursts. All the above mentioned data analysis was done by the PIE analysis with MATLAB (PAM) software package.[56]

3.2.8   In vitro sample preparation and surface immobilization

Biotin-streptavidin interaction was used to immobilize tagged proteins and labelled DNA on a PEG-functionalized coverslip for single molecule studies. The protein-his-tag and a biotin-NTA chelated with Ni^{2+} were used to mark GlnBP(111-192) labelled with maleimide modified derivatives Atto532/Atto643, whilst DNA labelled with Cy3B/Atto647N was directly tagged with a biotin.
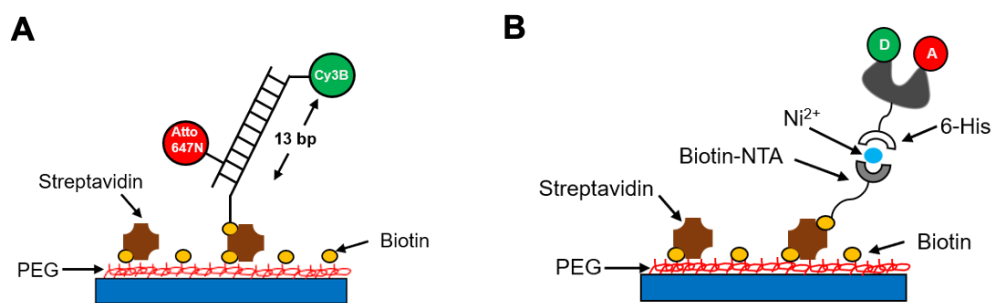
Figure 3.4. (A) Schematic view of dsDNA labelled with Cy3B and Atto647N for smFRET characterization on PEGylated coverslips. (B) Schematic view of the refolded GlnBP(111-192) labelled with Atto532-Atto643 for smFRET characterization.

To prepare a functionalized glass surface, cover slides (1.5H Marienfeld Superior) were first sonicated in MQ water for 30 min. The slides were then rinsed three times with MQ water, sonicated for 30 min in HPLC-grade acetone, rinsed three times with MQ water again. Then the slides were sonicated with 1M KOH for 30 mins, rinsed three times with MQ water and dried with a stream of nitrogen air. To remove any organic material left on the surface, the cover slides were plasma-cleaned for 15 min with oxygen. To create a mPEG/biotin–coated surface, the slides were immediately incubated in a 99:1 solution of mPEG3400-silane (abcr, AB111226) and biotin-PEG3400-silane (Laysan Bio Inc) in a Toluene solution overnight at 55°C. After incubation, the slides were sonicated (10 minutes in ethanol, 10 minutes in MQ water), dried under nitrogen stream, and kept under vacuum. Prior to TIRF experiments, each slide was incubated with a 0.2 mg/mL streptavidin in PBS solution for 10 minutes utilizing Ibidi sticky-slide (18 well) for single molecule studies. PBS buffer pH7.4 was used to wash away the unbound excess of streptavidin. For GlnBP(111-192) immobilization, 20 nM biotin-NTA (QIAGEN) was charged with 50 nM Ni^{2+} and incubated on the slide for 10 minutes before rinsing away the unbound excess biotin-NTA and Ni^{2+} with PBS (this step was omitted for the labelled DNA samples). GlnBP(111-192) at 0.8 nM and dsDNA at 0.04 nM were incubated for 5 and 1 minutes, respectively.

For single-molecule data collecting, imaging buffer (PBS, pH 7.4) containing 2 mM Trolox for protein. For dsDNA we used PBS buffer in combination with an oxygen scavenging system (pyranose oxidase at 3 U/mL, catalase at final concentration of 90 U/mL, and 40 mM glucose). After that, the chambers were sealed with Silicone Isolators^{TM} Sheet Material (Grace Bio-labs). All the single-molecule investigations were done at room temperature.

3.2.9 TIRF microscopy: smFRET measurements and data analysis.

Single molecule TIRF measurements were conducted on a homebuilt microscope using an Olympus iX71 inverted microscope body. Light from a 532 nm continuous wave laser (532 nm OBIS, Coherent) was transmitted off-axis onto the back-focal plane of a microscope objective (UAPON TIRF 100X 1.49NA, Olympus) via a dual band dichroic beam splitter (TIRF Dual Line Beam splitter zt532/640rpc, AHF Analyse Technik) to generate total internal reflection at the glass-water interface. Fluorescent emission was then split spectrally using a Dual View System (DV2, Photometrics) equipped with a dichroic beam splitter (zt640rdc, AHF Analyse Technik). The two emission channels were then spectrally filtered using emission filters (582/75 Brightline HC and 731/137 Brightline HC respectively, both AHF Analyse Technik). Image series were acquired using an EMCCD camera (C9100-13, Hamamatsu) in combination with the µManager[57] software.

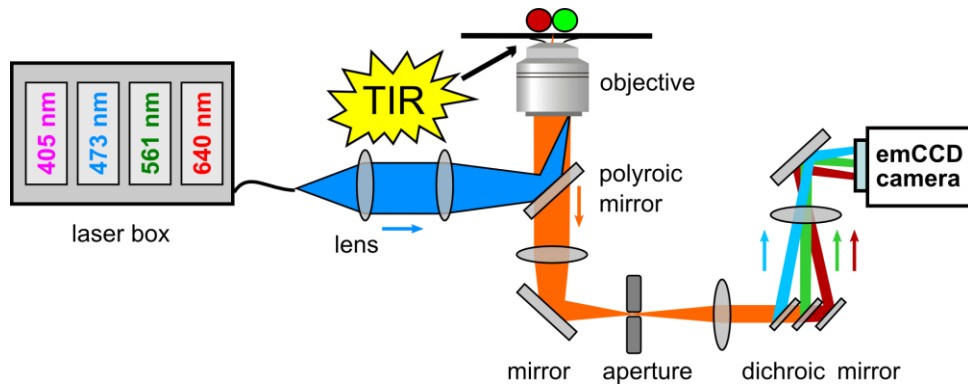**Figure 3.5.** Schematic of TIRF microscopy imaging for smFRET from the lab of Johannes.

The iSMS[58] software was used to retrieve and calculate traces of the donor and acceptor fluorescence intensity from consecutive fluorescent images.

4 Results

4.1 Targetable Conformationally Restricted Cyanines Enable Photon-Count-Limited Application

Diffusion-based single-molecule FRET (smFRET) has become a popular method to study structural changes and dynamics of biomacromolecules with high spatial and temporal resolution in aqueous solution. For smFRET assays, excellent photophysical properties of dye are a prerequisite. Synthetic fluorescent dye molecules are widely used in such assays. However, the performance and photon output of the popular cyanine dyes is often hampered by the inherent ability for *cis-trans* photoisomerization that can occur around the polymethine chain and lets to a reduction of quantum yield due to internal conversion. This can severely impact the information accessible via smFRET technique[59] and lead to a reduction of the quality of FRET efficiency histograms or limit temporal resolution and distance accuracy.

To address this issue, our collaborators from the Schnermann laboratory at NIH rigidized the polymethine dye core [10] to increase the quantum yield and the lifetime of cyanine chromophores (Cy5B and Cy5B-trisulfo). To validate the performance of conformationally restricted cyanine dyes, we performed smFRET measurements on the MalE variant which labelled with normally used acceptor dyes benchmarked with conformationally restricted cyanine dyes.

4.1.1 Establishment of protein model system: MalE(T36C-S352C).

MalE, a periplasmic component of an ABC transpoter[60], consists of two globular lobes (the N-terminal and the C-terminal domains) that can form a substrate binding pocket at their interface. To study the conformational changes of MalE via labelling with maleimide modified fluorophores, the double-cysteine

variant MalE (Thr36Cys-Ser352Cys) [34] was designed. The crystal structure of this variant was shown in Figure 4.1. The labeling positions on MalE were chosen such that the apo (open) conformation (in the absence of maltose) displayed lower FRET efficiency in comparison to the holo (closed) state (100 mM maltose) of the protein.
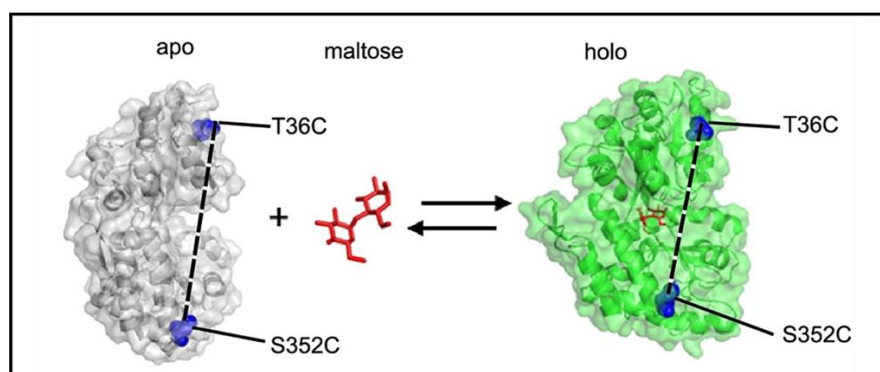
Figure 4.1 Crystal structure of MalE in apo (grey, pdb file:1omp) and holo (green, pdb file:1anf) where the labeling positions Thr36Cys and Ser352Cys are indicated in blue.

4.1.2 Protein labelling and purification with SEC.

The process of protein labelling involved the utilization of thiol-maleimide chemistry, which aimed to target the thiol group of amino acid cysteine through the use of maleimide-modified fluorophore dyes. By employing this technique, double-cysteine mutants of the MalE variant were labelled with distinct fluorophore pairs (AF555/AF647, AF555/ATTO647N, AF555/Cy5B and AF555/Cy5B-trisulfo), respectively (Figure 4.2). Consequently, the labelled MalE variant were purified with SEC and the chromatograms of labelled protein were displayed in Figure 4.2. For the further smFRET measurements, the fractions having the best overlap of protein, donor and acceptor absorption were used (as indicated by the grey areas).
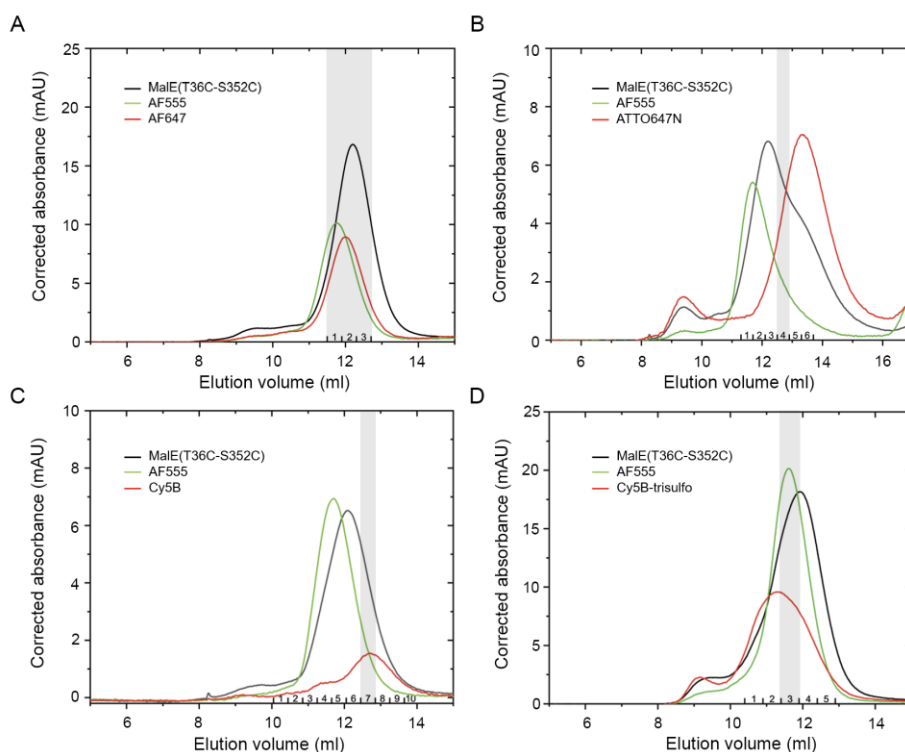
Figure 4.2. Size exclusion chromatography (SEC) of MalE mutants labeled with various fluorophore pairs. The MalE mutants labeled with various fluorophore pairs were purified using size-exclusion chromatography (SEC). The protein absorption was measured at 280 nm (black curves) and the donor dye (AF555) absorption at 555 nm. The acceptor dye absorption (red lines) was measured at 647 nm for AF647 and Atto647N, and at 688 nm for Cy5B and Cy5B-trisulfo. The following fractions were used for the experiments: (A) Fractions 1- 3, ~12.2 mL; (B) Fraction 4, ~12.7 mL; (C) Fraction 7, ~12.7 mL; (D) Fraction 3, ~11.4 mL.

4.1.3 Diffusion-based smFRET investigation of MalE.

Diffusion-based single-molecule FRET (smFRET) is a well-established method to study conformational changes[61] of biomacromolecules in aqueous solution at ambient temperature using microsecond alternating excitation (µsALEX)[7, 14, 62, 63]. µsALEX analysis is expected to show multiple species in the two-dimensional histogram (Figure 4.3) of apparent FRET E* (x-axis) and stoichiometry S* (y-axis). While donor-only (D$_{only}$, high S*, low E*) and acceptor-only subpopulations (A$_{only}$, low S, intermediate to high E*) are well separated from the donor-acceptor-containing proteins (DA), photophysical

artifacts such as blinking or bleaching manifest as bridges between the latter (denoted as donor and acceptor photophysics).[59, 64] Such unwanted photophysical behavior of either donor or acceptor dye can thus alter the "true" mean FRET-efficiency value of an observed species or broaden populations in the FRET efficiency histograms. While broadening is often interpreted as fast (sub-millisecond) structural dynamics, a change of FRET efficiency caused by photophysical effects might be assigned incorrectly to a longer distance.
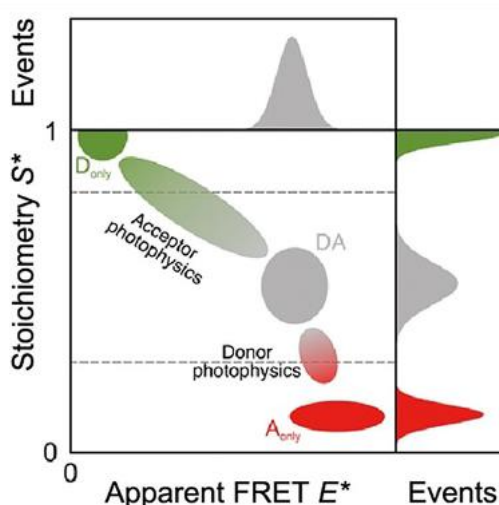
Figure 4.3. Schematic depiction of an E*-S* histogram E*-S* histogram obtained by µsALEX. Using µsALEX, the stoichiometry S* can be used to separate donor only (D_{only}), acceptor only (A_{only}), and the FRET species with both donor and acceptor fluorophore (DA). Bridge artifacts caused by unwanted donor or acceptor photophysics (blinking and/or bleaching) can result in artificial broadening of the FRET population or a shift of the extracted mean apparent FRET efficiency.

To evaluate the performance of Cy5B and Cy5B-trisulfo in smFRET measurements using µsALEX, the commonly-used dye combination (donor dye AF555 with acceptor AF647 and ATTO647N)[50] were benchmarked against the conformationally restricted sulfonated cyanine dyes. The µsALEX histograms of MalE variant labelled with different fluorophore pairs revealed that the protein adopted the (low FRET) apo conformation in the absence of ligand, which is

altered into the closed-liganded conformation when 100 mM maltose were added (Figure 4.4). Hence, the assay was validated by reproducing the earlier results and structural predictions[12].
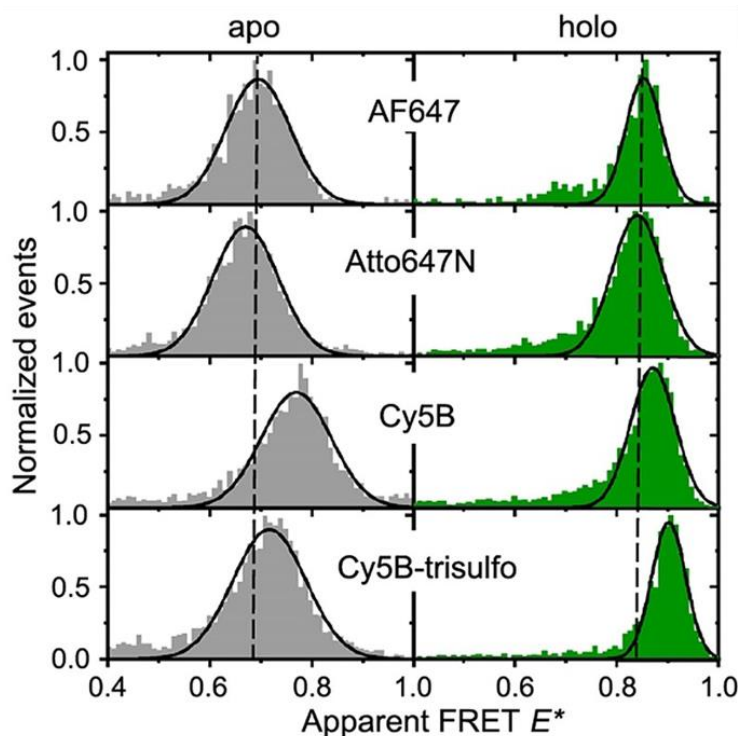
Figure 4.4 Apparent FRET efficiency E* histograms of MalE obtained from single molecule μsALEX FRET experiments. Different FRET acceptor fluorophores as indicated in the Figure panels were combined with the same donor fluorophore (AF555). E* histograms were recorded in the absence (apo) and presence of saturating ligand concentrations of 100 mM maltose (holo). Solid lines are the projections of 2D Gaussian fits to the data from which the mean apparent FRET efficiency and width of the histogram was determined (see also panel D). All histograms shown are projections from bursts with a stoichiometry between 0.3 and 0.7. See Figure S3 for full 2D datasets including intermediate ligand concentration.

Due to the spectral similarity between the acceptor dyes, all dye-pairs showed similar, yet not identical, mean FRET efficiencies and width with good histogram quality (that is, little bridge artifacts due to donor or acceptor photophysics, also see Figure 4.5). Indeed, the cleanest histogram was obtained for Cy5B-trisulfo as acceptor dye (Figure 4.4, bottom row) lacking any bleaching trail at FRET values lower than the peak. The expected response of the smFRET assays can be

observed upon the addition of 1.5 mM maltose, which corresponds to a fraction closed of 0.3-0.4 (Figure 4.5). This concentration is in proximity to the dissociation constant Kd for the interaction[12] between the protein and maltose.

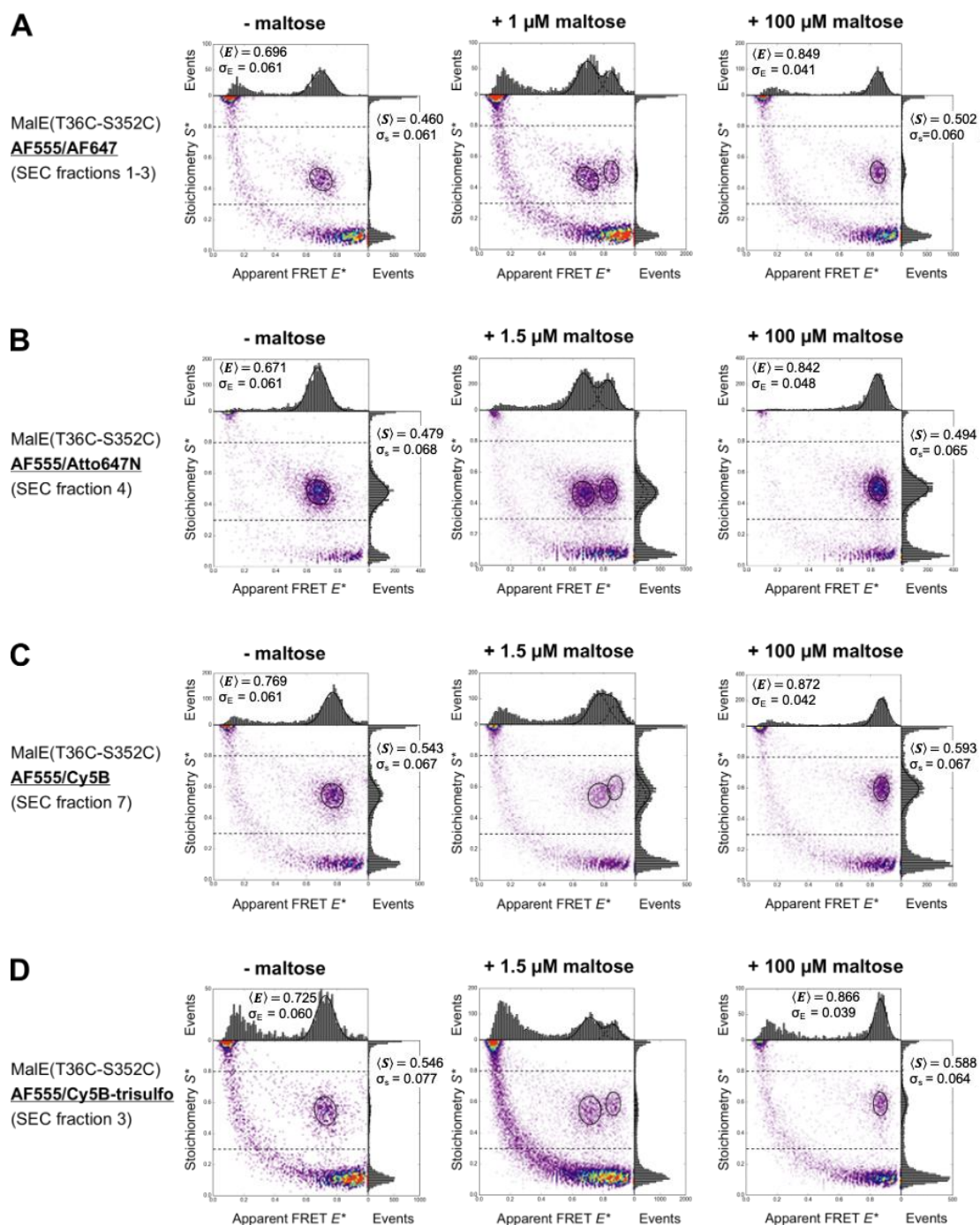**Figure 4.5 Maltose-induced conformational changes in MalE visualized by ALEX measurements.** ALEX-based E* - S* histograms of the MalE double-cysteine mutant labeled with various fluorophore pairs. First, the histograms of the apo (no maltose) and holo (100 μM maltose) state of the protein were fitted using a 2D gaussian distribution. Subsequently, these

two distributions were used to fit the intermediate ligand concentration. (A) MalE labeled with AF555- AF647 shows an open state at E* = 0.696 and a closed high FRET state at E* = 0.849 in the S5 presence of a saturating concentration of maltose. (B) MalE labeled with AF555-ATTO647N shows an open state at E* = 0.671 and a closed high FRET state at E* = 0.842 in the presence of a saturating concentration of maltose. (C) MalE labeled with AF555-Cy5B shows an open state at E* = 0.769 and a closed high FRET state at E* = 0.872 in the presence of a saturating concentration of maltose. (D) MalE labeled with AF555-Cy5B-trisulfo shows an open state at E* = 0.716 and a closed high FRET state at E* = 0.902 in the presence of a saturating concentration of maltose. At maltose concentrations around the Kd, both populations are similar as expected from the ligand affinity of the wild-type protein.

To benchmark the dyes further quantitatively against each other, the acceptor photon count rates at 60 μW green and 25 μW red laser excitation intensity were compared. Strikingly, a maltose dependent fluorophore brightness, which all dyes were similarly bright in the holo state (Figure 4.6 A), yet the Cy5B dyes were slightly less bright (by 5–10 kHz) in comparison with AF647 and ATTO647N in the apo state (Figure 4.6 A). This observation suggests that less FRET bursts can be retained for AF555-Cy5B-monosulfo and AF555-Cy5B-trisulfo compared to the other two fluorophore pairs (Figure 4.6 B). Nevertheless, the Cy5B derivatives showed a unique advantage over both AF647 and ATTO647N.
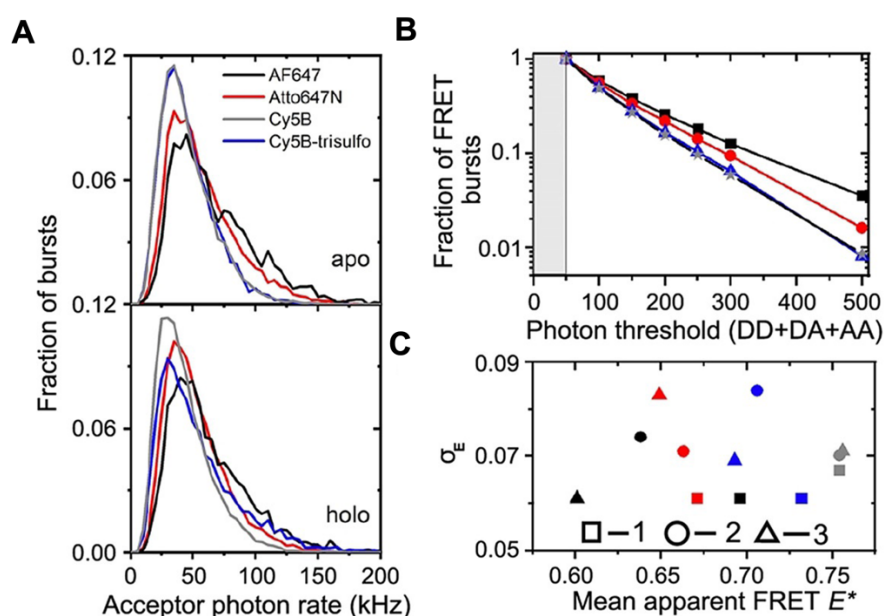
Figure 4.6. (A) Photon counting histograms (PCH) of the same data sets as in (Figure 4.4) obtained from direct acceptor excitation for the protein in the apo and holo state. Only bursts with an apparent FRET efficiency of 0.4-1 and a stoichiometry between 0.3 and 0.8 were used for the analysis. The acceptor photon count rate was determined by comparison of absolute number of detected photons and the respective burst length. (B) Fraction of bursts with intermediate stoichiometry values (0.3–0.7) where both donor and acceptor dye were present ("FRET bursts") as a function of increasing all photon threshold (DD=Donor emission after Donor excitation, DA=Acceptor emission after Donor excitation, AA=Acceptor emission after Acceptor excitation). The survival fraction of FRET bursts was normalized to the number of FRET bursts at a photon threshold of 50. All data were all recorded in the absence of ligand. The same colors were used as in panel B to indicate the different acceptor dyes.

The laser power dependence measurements were further performed to validate the stable photophysical property of structure restricted cyanine dyes against AF647 and ATTO647N (Figure 4.7). Due to the absence of trans-cis isomerization, the Cy5B dyes had strongly reduced bridge artifacts caused by the acceptor dye and was able to retain the mean E* position and width s_E of the population over the entire range of excitation powers studied (Figure 4.6 C, Figure 4.7)[59]. Also, Cy5B-trisulfo had only a small change of mean peak position, yet substantial change of the population width, which was similar to ATTO647N.
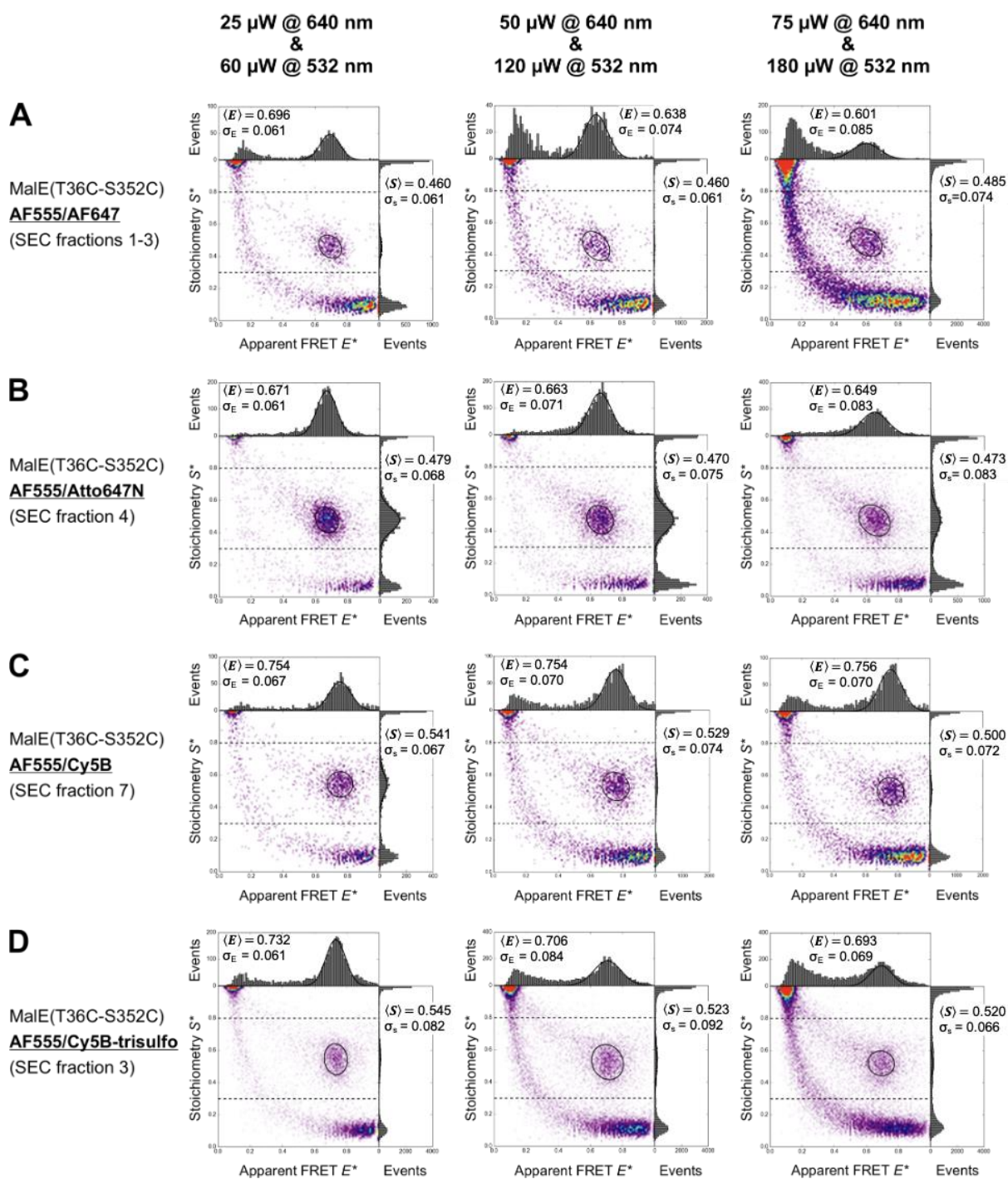
Figure 4.7 Single-molecule FRET histogram of MalE labeled with different fluorophore pairs under various laser powers: Three distinct excitation conditions were used, where the ratio of green-to-red laser intensity was kept constant. Each column was obtained using a different laser power, as is indicated above each row, while each column shows the histograms for a different dye pair. All data was recorded in the apo state (absence of ligand). All histograms were fitted independently (i.e., no parameters were fixed based on other measurements) to be able to extract the influence of the excitation power on the mean apparent FRET E* and width sE extracted via the 2D gaussian fit.

Overall, these observations establish Cy5B and Cy5B-trisulfo as useful alternatives to AF647 and ATTO647N in smFRET experiments, particular to reduce blinking and bleaching artefacts for maintaining correct mean FRET efficiencies. Additionally, the Cy5B dyes behave very well at higher laser powers and with the observed photon output, they are also suitable in cases where high temporal resolution is required. We should mention that the observed fluorophore performance may differ significantly for other biomolecular targets. Thus, alternative protein systems or nucleic acid targets should be tested in smFRET studies with Cy5B derivatives as acceptor dye (in combination with green absorbing donors) or as a donor dye for near infrared acceptors. We also suggest that the Cy5B derivatives might be particularly useful for (smFRET) assays, where interactions of nucleic acids and proteins are monitored, since conventional cyanine dyes often show (unwanted) environment-dependent fluorescence lifetimes[65, 66] which can be minimized for rigidized derivatives of Cy3B or Cy5B.[67, 68]

4.2 Dissecting Mechanisms of Ligand Binding and Conformational Changes in the Glutamine Binding Protein

Protein conformational dynamics play a crucial role in protein-ligand interactions. However, the underlying mechanisms of these interactions are often poorly understood. *E.coli* GlnBP is a typical periplasmic substrate binding protein (SBP), which can specifically bind L-glutamine. Crystallography studies have identified two main conformational states of GlnBP: an open (unliganded) state and a closed (liganded) state, corresponding to an induced-fit interaction. However, recent studies using single-molecule FRET spectroscopy imply that GlnBP can undergo intrinsic conformational changes both in the absence[41] and presence of substrate[44] and sample a broad range of conformational states, which would correspond more to a conformational selection model[43].

These results and conclusions were in stark contrast to the results obtained in previous work, where structurally related proteins from the amino acid transporter GlnPQ and its two ligand binding domains SBD1 and SBD2 were studied[12, 45]. Furthermore, inconsistencies in the NMR approach were identified by Kooshapur and co-workers[46], who found no evidence for the existence of additional conformers of GlnBP under apo, i.e., ligand-free conditions. Additionally, their NMR data on apo GlnBP show the existence of one single apo-open conformer, in agreement with a unique solved unliganded crystal structure of the protein. Similarly, MD simulations of SBD2 also suggest that it does not adopt the closed conformation in the absence of ligand. These simulations instead suggest that ligand binding to one of the two rigid domains precedes formation of the closed state, which is generally compatible with an induced-fit type binding mechanism[47]

Therefore, in this chapter, we characterize the biochemical and biophysical properties of GlnBP cysteine variants to investigate the mechanisms of ligand binding and conformational changes in the GlnBP.

4.2.1 Constructions, overexpression, and purification of GlnBPs.

For the study of the thermodynamic and kinetic aspects of ligand binding in GlnBP, the wild-type protein (GlnBP WT) and two double-cysteine variants GlnBP(111-192) and GlnBP(59-130) for analysis of conformational states via smFRET were produced. The crystal structure of these two variants were shown in Figure 4.8. V111C and G192C were mutation points on GlnBP(111-192), and T59C and T130C were mutation points on GlnBP(59-130). The mutant of GlnBP(59-130) was adapted from refs.[41, 44] Both GlnBP variants adopted an apo state in the absence of ligand and transferred to a holo state in the presence of ligand (Figure 4.8).
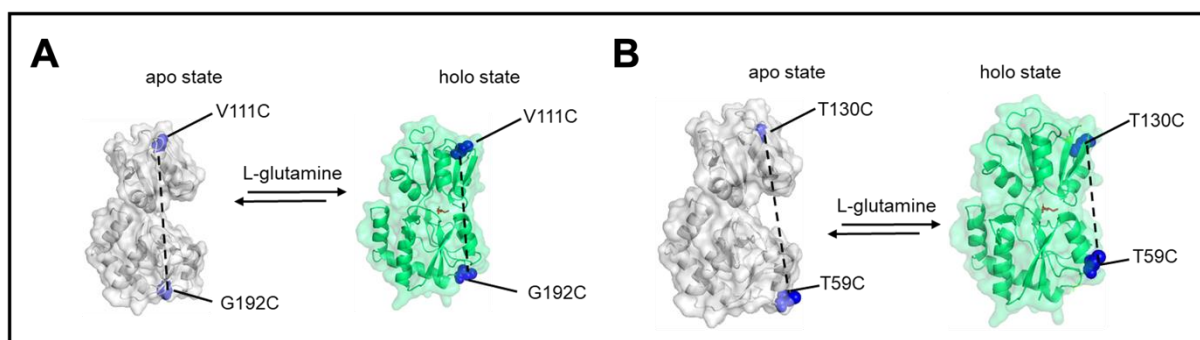
Figure 4.8 Crystal structure of GlnBP(111-192) and GlnBP(59-130). (A) Crystal structure of the ligand-free (grey structure) and ligand-bound GlnBP (green structure) where the labelling positions V111C and G192C are indicated in blue. (B) Crystal structure of the ligand-free (grey structure) and ligand-bound GlnBP (green structure) where the labelling positions T59C and T130C are indicated in blue.

In the first step, the GlnBP and both mutants were overexpressed to produce specific protein for subsequent experiments. Upon the introduction of the dedicated plasmids into *E. coli* BL21-pLysS cells, visible colonies could be observed on the agar plates. Then the plasmid was extracted and sequenced that indicated successful plasmid transformation (Fig. 4.9).
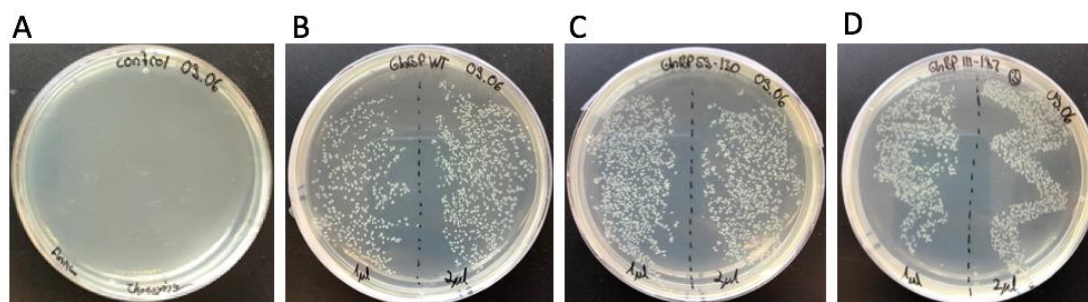
Figure 4.9: Agar-plates containing the E. coli BL21-pLysS cell colonies. (A) Control without colonies (B) Colonies containing the plasmid for the wild-type GlnBP, (C) Colonies containing the plasmid for GlnBP59-130, (D) Colonies containing the plasmid of GlnBP111-192.

After the overexpression, GlnBP WT and GlnBP variants were purified using affinity chromatography. Protein purity was assessed by Coomassie-stained SDS-PAGE analysis (Figure 4.10A). The left side of the gel is the protein ladder that indicated the size of the protein in kDa unit. The GlnBP and both mutants only showed one band, respectively, and had the same size (~26.8kDa), which indicated the high quality of purity. As reported previously, GlnBP copurifies with bound glutamine[69].Therefore, the unfolding and refolding processes were performed to remove the ligand in the protein stock. To confirm that the refolding process did not form multimers of GlnBP, the SEC chromatograms of refolded GlnBPs were compared with the unprocessed protein, individually. As showed in Figure 4.10B, the elution volume and shape of the GlnBP before and after refolding matched very well, which prove the monomeric state and proper folding of the GlnBPs.
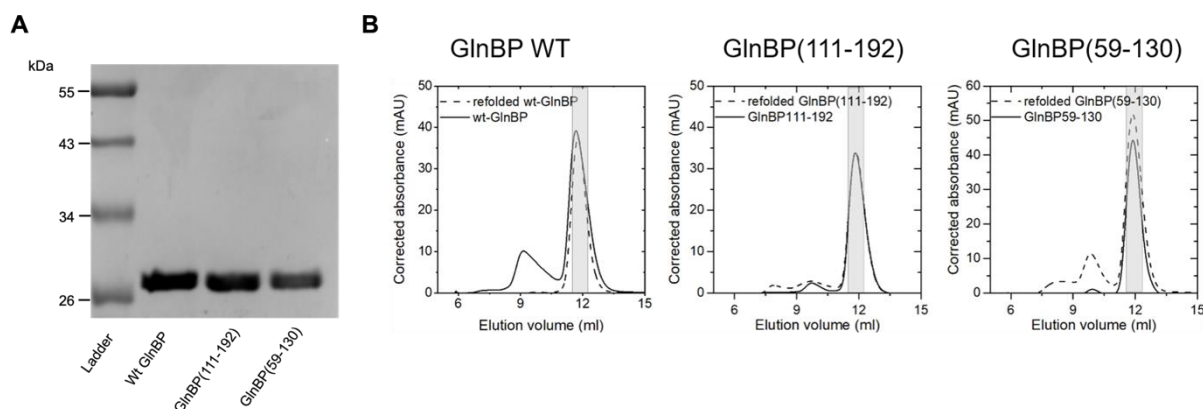
Figure 4.10. Biochemical characterization and size exclusion chromatography (SEC) of refolded GlnBP WT and GlnBP variants. (A) Coomassie-staining SDS-PAGE analysis of GlnBP purity. Lane 1, molecular mass ladder with sizes of relevant proteins indicated in kDa; lane 2, purified GlnBP WT; lane 3, purified double-cysteine variant GlnBP(111-192); lane 4, purified double-cysteine variant GlnBP(59-130). (B)The GlnBP WT and GlnBP variants were unfolded with 6M Guanidine Hydrochloride and then refolded via dialysis over two days in PBS buffer (pH 7.4, 1 mM DTT). The selected fractions (grey shaded area) were collected and used for ITC experiments. The protein absorption was measured at 280 nm.

4.2.2　Binding affinity characterization using ITC.

To assess the binding affinity of GlnBP WT and the two GlnBP cysteine variants for L-glutamine, the ITC[70] experiments were conducted. ITC is a label-free quantification technique used in studies of a wide variety of biomolecular interactions. It can directly measure heat transfer that enables accurate determination of binding constant (Kd), reaction stoichiometry (n), enthalpy (ΔH) and entropy (Δs). This provides a complete thermodynamic profile of the molecular interaction. The refolded GlnBP WT showed a Kd for L-glutamine of 22 ± 7 nM (Figure 4.10A), similar to the Kd values of both cysteine variants (Figure 4.10B/C). The binding site of GlnBP WT and two mutants were around 1 which indicated that the binding ratio is 1:1. These values were in agreement with previously published data[37]. This verifies that the unfolding and refolding

process as well as cysteine substitutions did not impact the biochemical properties of GlnBP.

Figure 4.11 Investigating binding affinity of refolded GlnBP WT, refolded GlnBP(111-192) and GlnBP(59-130) using Isothermal titration calorimetry (ITC) measurements.. The graphs depicted the changes in heat (DP, top) and enthalpy (ΔH, bottom), due to each injection of L-glutamine into the sample cell, as function of time (top x-axis of each graph) and molar ratio of refolded protein and ligand (bottom x-axis), separately. All ITC experiments were repeated three times and performed without fluorophore labelling. (A) The mean binding affinity of the refolded GlnBP WT is 17 ± 7 nM and the binding ratio is around 1. (B) Ligand-binding affinities of refolded, unlabelled GlnBP(111-192) was determined by ITC with a $K_d =$ 35 ± 5 nM for L-glutamine (mean value from N = 3 with standard deviation), which is in agreement with previous reports[37]. The free energy of binding was ΔG = -42.6 kJ/mol with the enthalpy (ΔH = -62.3 kcal/mol) and entropy contributions $-T^*\Delta S$ (19.9 kcal/mol). (C) The mean binding affinity of the refolded GlnBP(59-130) is 28 ± 4 nM and the binding ratio is around 0.9.

The binding affinity between L-arginine and refolded GlnBP mutants was also investigated using ITC measurements. GlnBP(111-192) mutant showed a Kd for L-arginine ~421 ± 292 μM (Figure 4.12A) and GlnBP(59-130) mutant showed a Kd for L-arginine ~206 ± 49 μM (Figure 4.12B). The binding site was fixed as 1 to fit the data. According to the ITC binding curves and results, the standard

deviation was huge that it is difficult to distinguish whether the two GlnBP mutants can bind the L-arginine or not. Therefore, we probed the conformational states of refolded GlnBP mutants using solution-based µsALEX measurements in chapter 4.23.
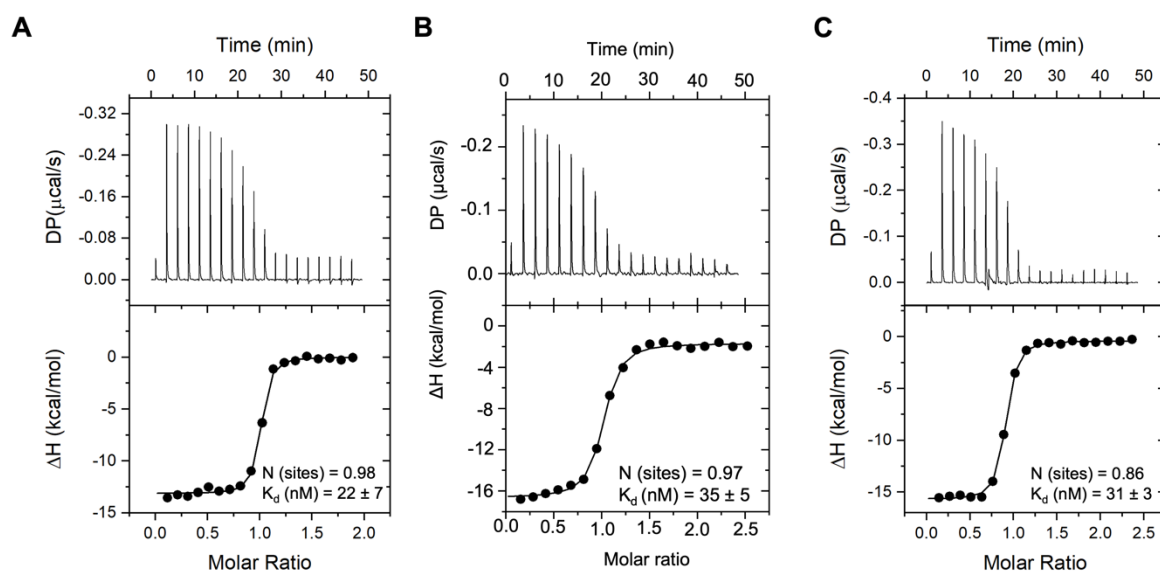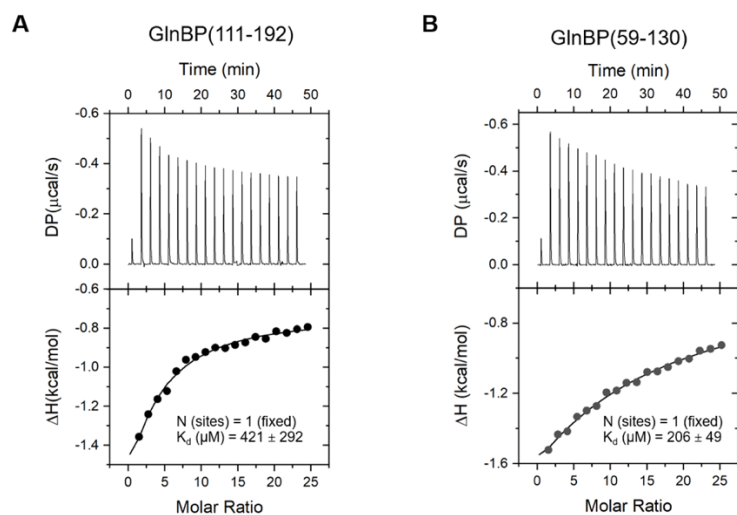

Figure 4.12. Investigating L-Arginine binding affinity of refolded GlnBP(111-192) and GlnBP(59-130) variants using Isothermal titration calorimetry (ITC) measurements. The graphs depicted the changes in heat and enthalpy with the injection of the L-Arginine against the time and molar ratio of refolded protein and ligand, separately. All the ITC experiments were repeated three times and performed without fluorophore labelling. (A) The average binding affinity of the refolded GlnBP(111-192) is 206 ± 49 µM. (B) The average binding affinity of the refolded GlnBP(59-130) is 412 ± 29 µM. The binding ratio (sites) is manually fixed to 1.

4.2.3 Protein labelling and analysis of conformational states of freely diffusing GlnBP.

After an assessment of the thermodynamic ligand binding characteristics of GlnBP, the conformational states and changes associated to ligand binding via smFRET were characterized using µsALEX microscopy. This method allows to study biomacromolecules in aqueous solution at ambient temperature to identify conformational changes, heterogeneity, small sub-populations and determine microscopic rates of conformational change.[7, 14, 71] smFRET relies on

fluorescently labelled molecules traversing a confocal excitation volume to generate short millisecond fluorescence bursts. Therefore, the two distinct GlnBP variants: GlnBP(111-192) and GlnBP(59-130) were labelled with various fluorophore pairs via thiol-maleimide chemistry. Here, the thiol group of the cysteine on the protein was targeted by maleimide-modified fluorophores. The labelled proteins were purified with SEC, as they were shown in Figure 4.13. The fluorophore peaks overlapped with the protein peak validating that the fluorophores were well labelled on protein. The selected fractions in grey colour indicated the good quality of labelling and were selected for further smFRET measurements.
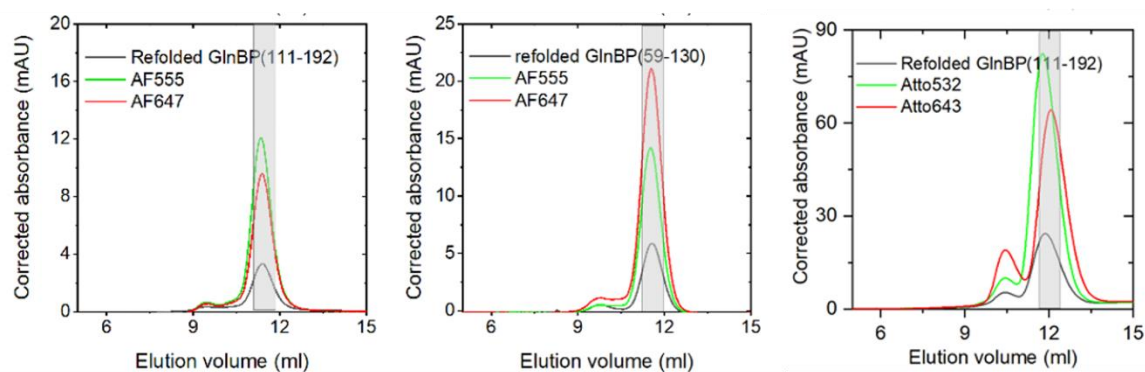
Figure 4.13 Size exclusion chromatography (SEC) of GlnBP variants labelled with distinct fluorophore pairs. For the solution-based smFRET measurements, the selected fractions (grey shaded area) having the best overlap of protein, donor, and acceptor absorption were used. The protein absorption was measured at 280 nm (black curves) and the donor dye (AF555) absorption at 555 nm or donor dye (Atto532) absorption at 532 nm. The acceptor dye absorption (red lines) was measured at 647 nm for AF647 and 643 nm for Atto643.

Subsequently, the refolded variants of GlnBP, namely GlnBP(111-192) and GlnBP(59-130), were studied using smFRET experiments in freely-diffusing conditions. Two different combinations of dye pairs were utilized to ensure that any observed effects were not dependent on position or fluorophore. The FRET assays were designed such that the inter-dye distance of the apo-state displays a lower FRET efficiency compared to the holo-state of the protein. Solution-based

μsALEX data of GlnBP mutants labelled with AF555/AF647 are shown with an all-photon burst search[49] in Figure 4.14A/B. The apo- and holo-states of GlnBP(111-192) showed a clear population of DA-labelled protein at S*-values of ~0.5, with two distinct mean E* values for the apo (low FRET, 0.51) and holo (high FRET, 0.68) states, which indicated that the protein adopted a conformationally closed state when adding 500 nM L-glutamine in the sample. Furthermore, no other substates were observed in both states. The same measurements were performed on GlnBP(59-130) using μsALEX microscopy. This mutant also displayed an apo-state (low FRET, 0.74) in the absence of ligand and a holo-state (high FRET, 0.89) when 500 nM L-glutamine was added. The varying residues positions on GlnBP are attributed to the differences in FRET efficiencies between the two mutants.
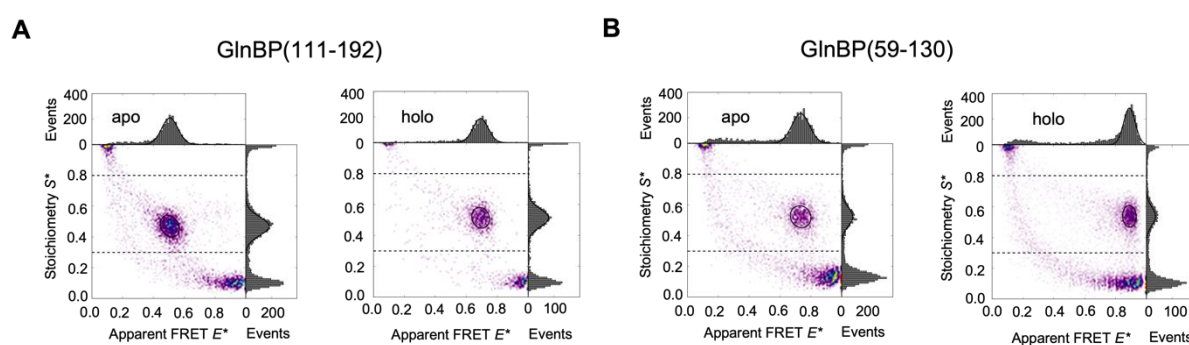
Figure 4.14 Typical μs-ALEX-based E*-S* histograms of the refolded GlnBP double-cysteine variants labelled with AF555 and AF647. (A) The apo (open) state of GlnBP(111-192) in the absence of L-glutamine. (B) The holo (closed) state of GlnBP(111-192) in the presence of L-glutamine (500 nM). (C) The apo (open) state of GlnBP(59-130) in the absence of L-glutamine. (D) The holo (closed) state of GlnBP(59-130) in the presence of L-glutamine (500 nM).

Then, the binding assays of the GlnBP mutants with L-arginine were performed via smFRET using μsALEX microscopy. However, both mutants did not show conformational changes after adding high concentration of L-arginine into the

samples in contrast with no ligand sample (Figure 4.15 A/B). Therefore, we concluded that the GlnBP cannot bind with L-arginine.
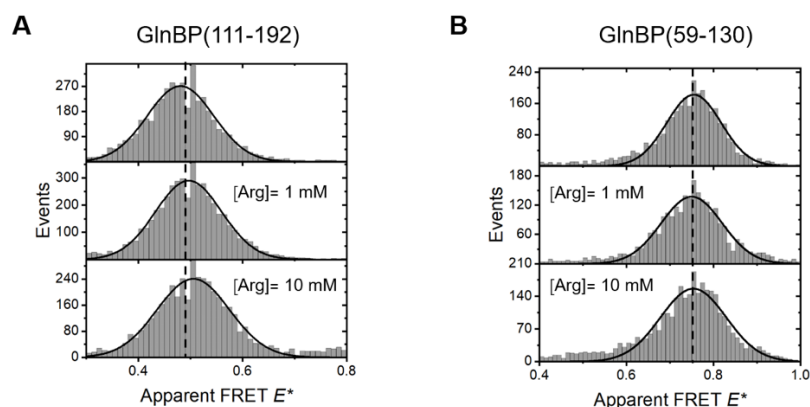
Figure 4.15. Conformational states of refolded GlnBP variants probed by solution-based μsALEX measurements reveal identical conformations. (A) Apparent FRET efficiency histograms of refolded GlnBP(111-192) in the absence (first row) and presence of L-arginine. (B) Apparent FRET efficiency histograms of refolded GlnBP(59-130) in the absence (first row) and presence of L-arginine.

Besides the μsALEX can check the conformational changes of SBPs, the μsALEX measurements can also investigate the binding affinity of SBPs. To further validate the binding affinity of GlnBP against the Kd values got form ITC, the full L-glutamine titration of GlnBP(111-192) labelled with AF555/AF647 was performed on μsALEX microscopy. The results were shown in Figure 4.16. First, the histograms of the apo (no L-glutamine) and holo (500 nM L-glutamine) states of the protein were fitted using a 2D gaussian distribution. Subsequently, these two distributions were used to fit the intermediate ligand concentration. According to the results, the closed population increased stepwise with the addition of L-glutamine. Refolded GlnBP(111-192) labelled with AF555-AF647 shows an open state at E* = 0.507 and a closed high FRET state at E* = 0.694 in the presence of a saturating concentration of L-glutamine. And the measurements were repeated three times.

Figure 4.16. L-glutamine-induced conformational changes in refolded GlnBP(111-192) visualized by μs-ALEX measurements. ALEX-based E*-S* histograms of the refolded GlnBP(111-192) double-cysteine mutants labelled with AF555-AF647 fluorophore pairs. Refolded GlnBP(111-192) labelled with AF555-AF647 shows an open state at E* = 0.507 and a closed high FRET state at E* = 0.694 in the presence of a saturating concentration of L-glutamine.

The full L-glutamine titration of GlnBP(59-130) labelled with AF555/AF647 was also performed on μsALEX microscopy. First, a 2D gaussian distribution was used to fit the histograms of the apo (no L-glutamine) and holo (500 nM L-glutamine) states of the protein. The intermediate ligand concentration was then fitted using apo and holo distributions. The results were shown in Figure 4.17. It was evident that the upper-left quadrant of the E*-S* histogram depicted a histogram, representing the donor-only population that were solely attributed to the efficiency of fluorophore labelling. The population in the lower-right corner represented the GlnBP which was labelled only by acceptors. These observations underscored the need to account for the impact of labelling efficiency on the resulting data. All measurements were repeated three times.
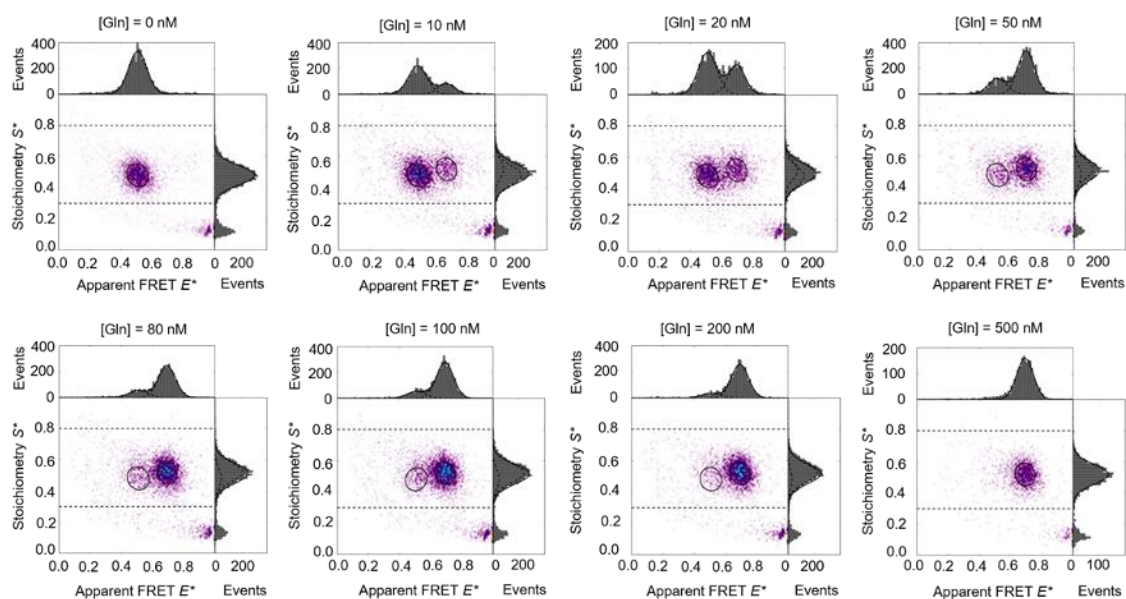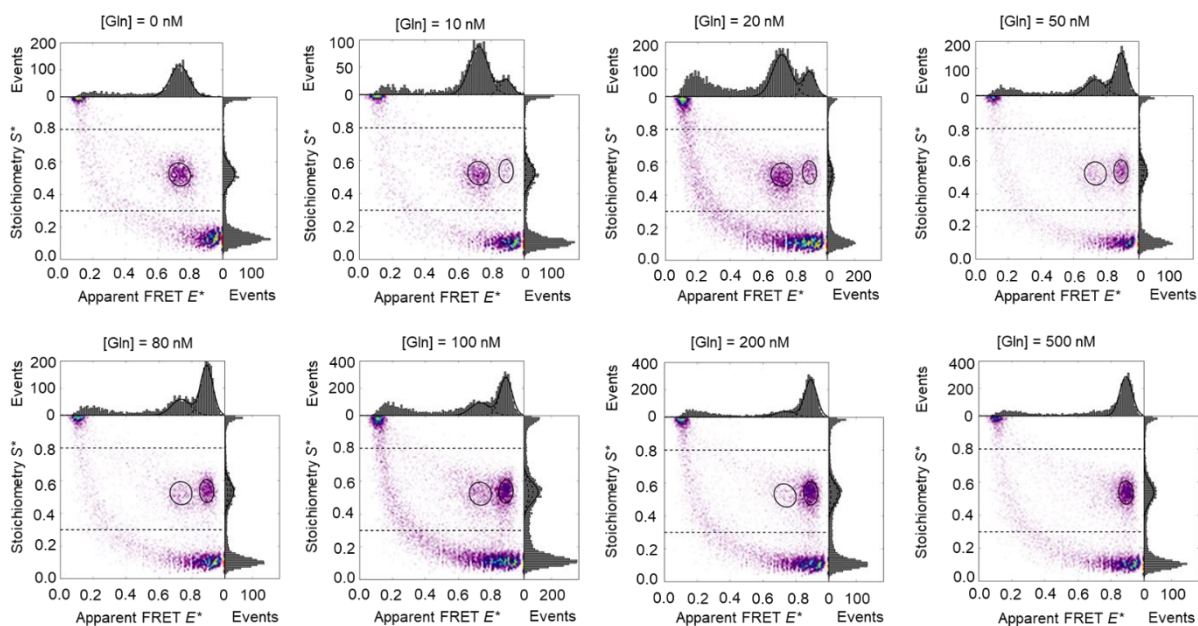
Figure 4.17 L-glutamine-induced conformational changes in refolded GlnBP(59-130) visualized by µsALEX measurements. ALEX-based E*-S* histograms of the refolded GlnBP(59-130) double-cysteine mutants labelled with AF555-AF647 fluorophore pairs. First, the histograms of the apo (no L-glutamine) and holo (500 nM L-glutamine) states of the protein were fitted using a 2D gaussian distribution. Subsequently, these two distributions were used to fit the intermediate ligand concentration. Refolded GlnBP(59-130) shows an open state at E* = 0.735 and a closed high FRET state at E* = 0.891 in the presence of a saturating concentration of L-glutamine.

To extract the binding affinity from the full ligand titration on µsALEX measurements, The fraction closed, i.e., the fraction of liganded protein, was determined from the ratio of the area of the high-efficiency peak and the total peak area from the projections in the apparent FRET efficiency. The fraction bound as a function of ligand (L-glutamine) concentration was fitted with the Hill equation using Origin 2016 (Origin Lab Corp, Northampton, MA), with the maximum number of binding sites fixed to 1. The final binding affinity result of GlnBP (111-192) and GlnBP(59-130) were in the range of 20-50 nM (Figure 4.18) which was fully consistent with ITC results (Figure 4.11). The measurements were repeated three times.
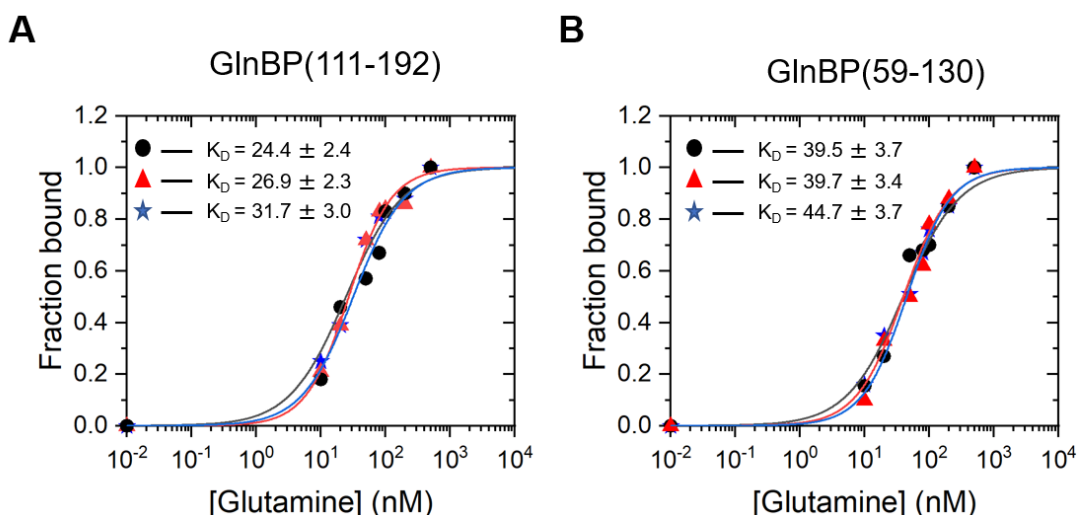
Figure 4.18. Investigating biding affinities of fluorescently labelled GlnBP variants using smFRET measurements. The binding curves are an evolution of the L-glutamine-induced conformational changes for GlnBP mutants from μsALEX using AF555 and AF647.

Our results are thus in agreement with the idea that GlnBP mainly exists in a single state – the open conformation – in the absence of L-glutamine. The correlation of the ligand concentration dependence in ITC and smFRET on the other hand strongly suggest that ligand binding and conformational change (into the closed state) are correlated.

4.2.4   Accessible volumes simulation.

To further support these conclusions, in particular the agreement of FRET efficiencies with the distances expected from the ligand-free and ligand-bound crystal structures, a quantitative comparison was conducted. Here, we assessed the inter-dye distances calculated from dye accessible volumes (AV) based on the structural models of apo and holo proteins and those obtained from experimental smFRET measurements. Such a quantitative approach is useful to understand whether inter-dye distances in either apo- or holo-states, which were measured in our smFRET experiments, match the crystal structure predictions. Any

discrepancies between these inter-dye distances in a particular state might imply fast conformational sampling in this state. For dye AV calculations, the FPS method was used, which was established by the Seidel lab[72]. The experimental data were corrected for setup-dependent parameters according to refs.[73, 74] to obtain accurate FRET values. Using a Förster distance of 5.1 nm for AF555/647, a good match between structural models and our data in terms of predicted and calculated inter-dye distance for both mutants were found (Figure 4.19, Table 1).
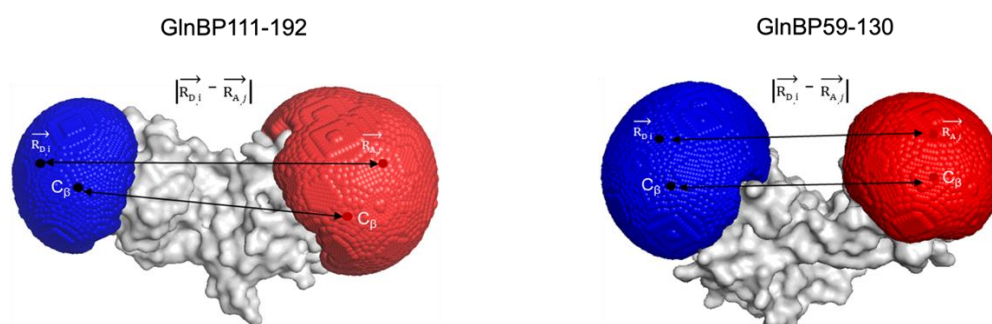
Figure 4.19. Dye accessible volume simulations of GlnBP(111-192) and GlnBP(59-130). A simulation of accessible volume for AF555 and AF647 at labelling position 59 and 130 on GlnBP. <RDA> is the distance between donor and acceptor accessible volume.

Table 1. Inter-dye distance comparison.

Distance [Å]	GlnBP(111-192) apo	GlnBP(111-192) holo	GlnBP(59-130) apo	GlnBP(59-130) holo
C_β-C_β	52	42	48	32
<R$_{DA}$>	70 ± 8	60 ± 9	57 ± 10	35 ± 10
<R> (μsALEX)	64 ± 1	54 ± 1	57 ± 1	45 ± 1

4.2.5 Screening for fast conformational motion via analysis of "within-burst" FRET dynamics.

Since intrinsic conformational dynamics might occur rapidly, resulting in temporal averaging of multiple conformational states within bursts, smFRET data were analyzed for "within-burst" FRET dynamics using BVA and mpH^{2}MM methods. These analyses provide access to FRET-dynamics that occur on timescales as rapid as a few alternation periods in the tens of μs up to the length of the burst, i.e., a few ms, which allows us to assess the static or dynamic character of GlnBP conformational states.

Following dual-channel burst search (DCBS)[49] and selection of μsALEX data of GlnBP(111-192) with ATTO532/ATTO643 as FRET donor and acceptor dyes, The investigation began by examining whether single-molecule bursts accumulate in different subpopulations based on their apparent FRET E* and S* values (Figure 4.20B/C). In the absence (Figure 4.20B/C, apo) and presence of saturating glutamine concentrations (Figure 4.20B/C, holo), single, predominant mid- and high-FRET population are present, respectively. At lower glutamine concentrations around the Kd value (20 nM), two subpopulations are clearly observed with similar mean E* values as those in apo and in holo states (Figure 4.20 B/C, Kd). This implies that GlnBP is open in the absence of glutamine, closed with high concentrations, and either in an open mid-FRET state (potentially ligand-free), or it is in a closed high-FRET state (potentially ligand-bound) at intermediate concentrations.

Burst variance analysis (BVA) of the data suggests that under each of the measurement conditions, the holo state of GlnBP(111-192) labelled with ATTO532/ATTO643 undergo dynamic changes in E* (Figure 4.20A, holo), while traversing the confocal excitation volume. In BVA "within-burst" E*-dynamics are identified as an elevated standard deviation of the apparent FRET efficiencies, σ(E*), beyond what is expected from photon statistics (σ(E*) triangle values larger than the semicircle). Hence, these single molecules exhibit within-burst

FRET-dynamics at times slower than the typical photon detection times (a few µs) and faster than typical burst durations through the confocal excitation volume (a few ms). A closer look at the BVA plots shows that these within-burst dynamics occur mostly between the predominant FRET subpopulations and minor subpopulations found at very low E* values.
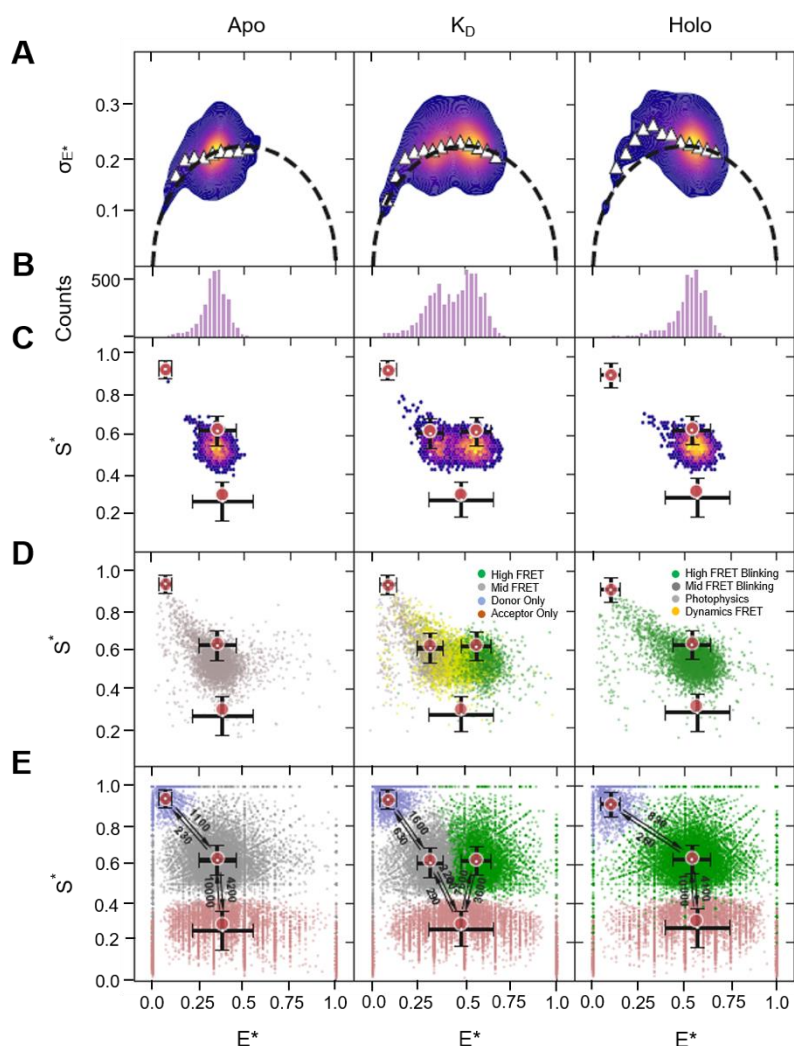
Figure 4.20. Screening GlnBP for rapid within-burst FRET dynamics. Confocal-based single-molecule FRET results for GlnBP(111-192) labelled with Atto532 and Atto643, in the apo state (left panels), near the K_d (middle), and in the holo state (right). (A) Burst variance analysis (BVA) showing a weak signature of within-burst FRET dynamics in the low E* regime. (B) Histograms of E* values of bursts, (C) E* versus S* 2D histograms of bursts, (D) 2D scatter plots of bursts classified by mpH^{2}MM, with colours corresponding to which state(s) are present within the bursts as determined with the Viterbi algorithm. Locations of states are given by red circles, and black crosses represent the standard deviation of E* and S* values of dwells within

each state. (E) E* versus S* 2D scatter plots of dwells in mpH^{2}MM-detected states within bursts detected by the Viterbi algorithm. Red circles and black crosses are same as in (D). Arrows and adjacent numbers indicate transition rates in s^{-1}. Transitions with rates less than 100 s^{-1} are omitted since such slow transitions are improbable to occur within single-molecule bursts with durations shorter than 10 ms and are most probably a mathematical outcome of the mpH^{2}MM framework. The dispersion of the E* and S* values of dwells in mpH^{2}MM-detected states are due to the short dwell times in these states, where the shorter the dwell time in a state is, the lower the number of photons it will include, and hence the larger the uncertainty will be in the calculation of E* and S* values of dwells. E* and S* are E* and S* values uncorrected for background, since in mpH^{2}MM all photons within bursts are taken into account, including ones that might be due to background.

To provide a potential answer to the question of what type of within-burst FRET-dynamics are observed in the BVA plots (conformational motion of GlnBP or photophysical dynamics of the dyes), further analyses of the burst photon arrival times data using multi-parameter photon-by-photon hidden Markov modelling (mpH^{2}MM)[51] were performed. This approach identifies the most-likely state model that describes the experimental results based on how E* and S* values may change within single-molecule bursts. For this analysis, (i) the most-likely number of states and their mean E* and S* values were reported (Figure 4.20C/E, red dots). (ii) We investigate whether molecules traversing the confocal excitation volume are fully static and only in the mid-FRET state or high-FRET state, or they undergo dynamic FRET-changes including transitions of mid/high-FRET states with photo-blinking dynamics or dark donor or acceptor states (Figure 4.20D). (iii) We finally report on E*/S* values for parts of bursts with dwells in one of the identified states and the rate constants of transitioning between them (Figure 4.20E). These analyses confirmed that among the two types of dynamic transitions that influence the burst-based E* and S* values, these are mostly donor or acceptor photo-blinking dynamics between bright and dark states. Such behavior is irrelevant to understand the conformational changes in GlnBP but does

influence the mean FRET efficiency values if not decoupled. This might explain the 0.3-0.5 nm deviations observed between experimental and modelled distances in Figure 4.19. Importantly, no dynamic transitions occur between the mid-FRET and high-FRET states at timescales shorter than 10 ms (i.e., with rate constants higher than 100 s^{-1}).

A similar behavior is observed for GlnBP(111-192) with AF555 and AF647 as fluorescent labels, yet within-burst dynamics become more pronounced (Figure 4.21). A limiting case is observed in GlnBP(111-192) with AF555 and AF647, with FRET dynamics between the predominant mid- and high-FRET states at the few ms timescale.

Figure 4.21. Screening GlnBP(111-192) for rapid within-burst FRET dynamics. Confocal-based single-molecule FRET results for GlnBP doubly labeled at residues 111 and 192 with

AF555 and AF647, in the apo state, near the K_D, and holo state. (A) Burst variance analysis showing a weak signature of within-burst FRET dynamics. (B) Histograms of E* values of bursts, (C) E* versus S* 2D histograms of bursts, (D) 2D scatter plots of bursts classified by mpH^{2}MM, with colors corresponding to which state(s) are present within the burst as determined with the Viterbi algorithm. Locations of states are given by red circles, and black crosses represent the standard deviation of E* and S* values of dwells within each state. (E) E* versus S* 2D scatter plots of dwells in mpH^{2}MM-detected states within bursts detected by the Viterbi algorithm. Red circles and black crosses are same as in (D). Arrows and adjacent numbers indicate transition rates in s^{-1}. Transitions with rates less than 100 s^{-1} are omitted since such slow transitions are improbable to occur within single-molecule bursts with durations shorter than 10 ms and are most probably a mathematical outcome of the mpH^{2}MM framework. The dispersion of the E* and S* values of dwells in mpH^{2}MM-detected states are due to the short dwell times in these states, where the shorter the dwell time in a state is, the lower the number of photons it will include, and hence the larger the uncertainty will be in the calculation of E* and S* values of dwells. E* and S* are E* and S* values uncorrected for background, since in mpH^{2}MM all photons within bursts are considered, including ones that might be due to background.

The μsALEX measurements of GlnBP(59-130) were also analyzed by BVA and mpH^{2}MM analysis. Strikingly, within-burst dynamics are very prominent in GlnBP(59-130), particularly with AF555 and AF647 as fluorescent labels (Figure 4.22)
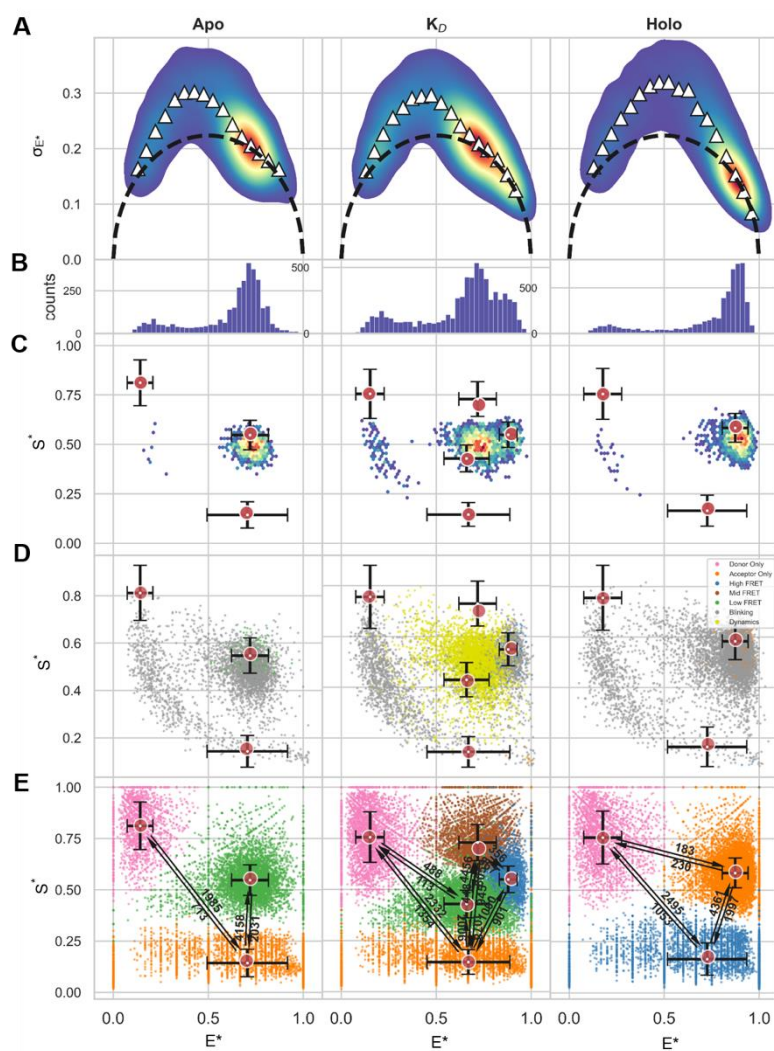
Figure 4.22. Screening GlnBP(59-130) for rapid within-burst FRET dynamics. Confocal-based single-molecule FRET results for GlnBP doubly labeled at residues 59 and 130 with AF555 and AF647, in the apo state, near the K_D, and holo state. (A) Burst variance analysis showing a weak signature of within-burst FRET dynamics. (B) Histograms of E* values of bursts, (C) E* versus S* 2D histograms of bursts, (D) 2D scatter plots of bursts classified by mpH^{2}MM, with colors corresponding to which state(s) are present within the burst as determined with the Viterbi algorithm. Locations of states are given by red circles, and black crosses represent the standard deviation of E* and S* values of dwells within each state. (E) E* versus S* 2D scatter plots of of dwells in mpH^{2}MM-detected states within bursts detected by the Viterbi algorithm. Red circles and black crosses are same as in (D). Arrows and adjacent numbers indicate transition rates in s^{-1}. Transitions with rates less than 100 s^{-1} are omitted since such slow transitions are improbable to occur within single-molecule bursts with durations shorter than 10 ms and are most probably a mathematical outcome of the mpH^{2}MM framework. The dispersion of the E* and S* values of dwells in mpH^{2}MM-detected states are due to the

short dwell times in these states, where the shorter the dwell time in a state is, the lower the number of photons it will include, and hence the larger the uncertainty will be in the calculation of E* and S* values of dwells. E* and S* are E* and S* values uncorrected for background, since in mpH2MM all photons within bursts are considered, including ones that might be due to background.

First and foremost, in all measurement conditions, the photo-blinking dynamics occur mostly on few ms to sub-millisecond timescales (Figure 4.20-Figure 4.22). Therefore, the blinking dynamics likely account also for the signature of within-burst dynamics shown by BVA.

Most importantly, mpH^{2}MM identifies single apo and holo E*-states, which describe the open mid-FRET and closed high-FRET conformations of GlnBP. Only in the presence of low (near Kd) concentrations of glutamine two FRET states are identified that could interconvert on timescales slower than 10 ms. Notably, the mean E* and S* values of the FRET states are slightly dissimilar to the centers of the burst-based E* and S* populations, owing to the effect of the rapid photo-blinking dynamics within bursts, which lead to averaging the E* and S* values of the FRET states with those of the photo-blinked states. Additionally, in the presence of near-K_D concentrations of glutamine, the FRET dynamics occur in the few ms timescale or even slower, which may contribute only slightly to the signature of FRET dynamics in BVA.

In conclusion, if intrinsic conformational dynamics existed in apo GlnBP, it could only be between the highly populated FRET conformation we identify and another conformation that is populated way below the sensitivity of our measurement and analysis (potentially below 5-10% populations). Thus, that indicated that the majority of the conformational dynamics in GlnBP is induced by glutamine, most probably as a result of its binding to GlnBP.

4.2.6 MFD-PIE measurements and burst-wise FCS analysis of GlnBP(111-192) labelled with Atto532/643.

Since our previous analysis could only study the time-regime down to about 100 µs we used another approach to see whether GlnBP is dynamic on faster timescales. MFD-PIE[54] is a cutting-edge technique that has been widely applied in the field of single-molecule imaging. MFD-PIE enables simultaneous imaging of two different fluorophores with different fluorescence lifetimes, which allows for the investigation of multiple molecular interactions within a single system. This feature provides a more comprehensive understanding of the dynamics of molecular interactions and their underlying mechanisms.

In Figure 4.23, two-dimensional plots were shown of the FRET efficiency (E) versus fluorescence lifetime of the donor in the presence of acceptor ($\tau_{D(A)}$) for both apo and holo states of GlnBP with labels ATTO532/ATTO643. The linear relationship between E and $\tau_{D(A)}$ defines the static FRET line (Figure 4.23A, black lines). When the labelled molecules show dynamics faster than the diffusion time, the species weighted averaged calculations of the FRET efficiency causes a bias towards longer lifetimes for donor, due to the higher brightness values of low-FRET species.[75] Therefore, in case of fast switching between various conformations (seen as distinct FRET efficiencies), a population shift occurs towards the right of the static FRET line. As can be observed from the plots (Figure 4.23A), the FRET populations for both apo and holo GlnBP are on the static FRET line, suggesting the absence of fast conformational changes < ms. This interpretation was further confirmed by burst-wise FCS analysis (Figure 4.23B). For this autocorrelation functions of donor (Figure 4.23B, green curves) and acceptor (Figure 4.23B, red curves) signals as well as the cross-correlations between donor and FRET signal (Figure 4.23B, black curves) were calculated. Conformational dynamics are expected to manifest as anticorrelation contribution in the cross-correlation function between channels due to fluctuations in FRET efficiencies appearing that occur faster than the diffusion time.[76] The burst-wise

FCS analysis resulted in flat cross-correlation functions (Figure 4.23B, black lines) for apo and holo states indicating the lack of microsecond dynamics down to the time-resolution of the experiments on the order of 100 ns.
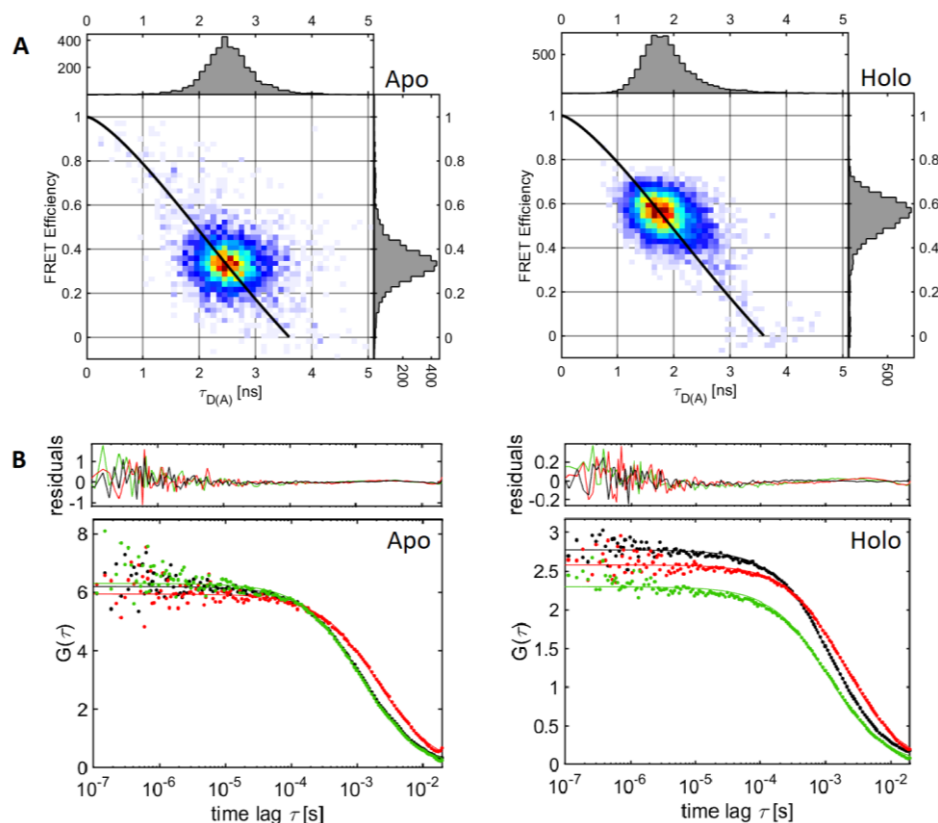
Figure 4.23 (A) Two-dimensional histogram of FRET efficiency (E) versus donor lifetime in presence of acceptor (τD(A)) for apo and holo GlnBP. The populations lie on the static FRET line (black) indicating the absence of conformational dynamics taking place at the sub-millisecond time range. (B) Analysis of conformational dynamics using burst-wise FCS for apo and holo states. The autocorrelation functions of the detected donor (DDxDD) and acceptor signal (AAxAA) are displayed in green and red, respectively. The cross-correlation function between donor and FRET signal (DDxDA) is shown in black.

The combined analysis of the ligand-free and ligand-bound states of GlnBP via ITC and smFRET strongly suggests that conformational changes in GlnBP (mostly) occur in the presence of ligand. Meanwhile, the data excludes any conformational dynamics of apo- and holo-GlnBP on timescales between 100 μs and 10 ms via mpH^{2}MM and even down to 100 ns via MFD-PIE and FCS (Figure

4.23). Furthermore, in the absence of glutamine the findings rule out that apo GlnBP can adopt (semi-)closed conformations on the timescale > 10 ms that are of high abundance > 5%, all in stark contrast to previous findings in refs. [41, 43, 44]

4.2.7   Studies of surface immobilized GlnBP via TIRF microscopy.

Based on a combined structural, biochemical, and biophysical analysis of GlnBP, no evidence for ligand-independent intrinsic conformational dynamics on timescales between 100 ns and 10 ms was found (see previous sections). Notably all these data are in strong contrast to findings (and interpretations) made in refs. [41, 43, 44], where smFRET was conducted with surface immobilized GlnBP using TIRF microscopy. To understand the discrepancies between these findings, TIRF-microscopy with surface-immobilized GlnBP were performed to characterize the protein and its conformational dynamics on slower timescales (i.e., >100 ms) and to screen for rare conformational events, which are better observed in surface-immobilized smFRET experiments due to longer observation times. Notably, TIRF microscopy was also used in published studies with conflicting results[41, 43, 44].

To exclude the influence of small molecule chemicals on the conformational state of GlnBP, we initially performed control experiments via µs-ALEX by screening buffer and experimental conditions that could impact the GlnBP conformation via possible contaminations. First, the normal µsALEX measurements of refolded GlnBP labelled with LD555/LD655 in PBS buffer (pH 7.4) using conventional microscope glass slides (Figure 4.24A) and using TIRF chamber (Figure 4.24B) were measured. No additional populations were found. Subsequently, the PBS buffer containing 40 mM glucose (Figure 4.24C), 50 nM Ni^{2+} (Figure 4.24D), pyranose oxidase/catalase (POC) (Figure 4.24E) and protocatechuate-

dioxygenase (PCD)/3,4-protocatechuicacid (PCA) (Figure 4.24F) were used for the ALEX measurements. Strikingly, various buffer additives used for oxygen depletion can cause apparent "closing" of GlnBP even when the protein is studied in solution (Figure 4.24E/F). Since this could be misinterpreted as intrinsic closing of GlnBP(111-192), consequently, these additives had to be omitted. Therefore, Only PBS buffer (pH 7.4) containing 2 mM Trolox as a photostabelizer was used, and GlnBP was surface immobilized via the biotin-NTA interaction facilitated by Nickel (II).
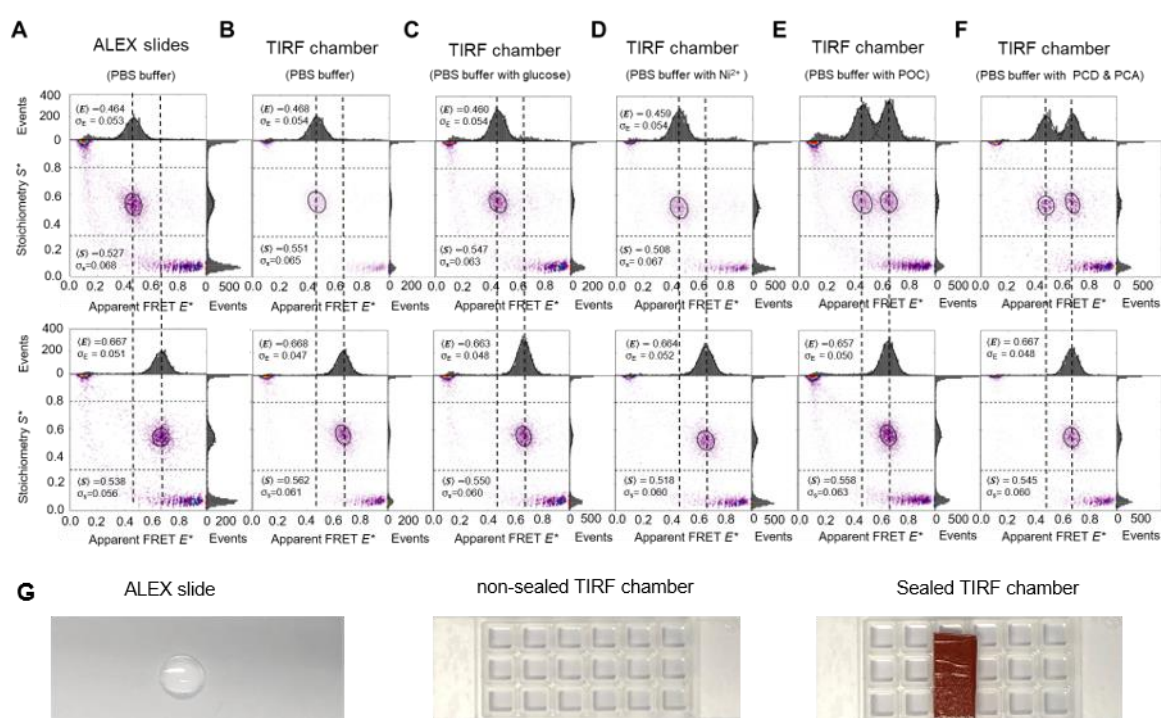
Figure 4.24. Effects on conformation of GlnBP(111-192) under various conditions. Due to the high binding affinity of GlnBP for L-glutamine, several control experiments under different conditions were performed to exclude artifacts induced by the reagents present in each set of experiments. The ALEX experiments of the refolded GlnBP(111-192) double-cysteine variant labelled with LD555-LD655 fluorophore pairs were measured in PBS buffer (pH 7.4) using conventional microscope glass slides (A) and using TIRF chamber (B). The PBS buffer containing (C) 40 mM glucose, (D) 50 nM Ni^{2+}, (E) pyranose oxidase/catalase (POC) and (F) protocatechuate-dioxygenase (PCD)/3,4-protocatechuicacid (PCA) was used for the ALEX measurements. (G) The conventional glass coverslips used in μs-ALEX experiments (top figure) and TIRF chambers (sticky-Slide 18 well, Ibidi; non-sealed chambers, middle figure; sealed,

bottom figure) glued on top of PEG-/biotin-PEG-silane microscope glass coverslips used in the TIRF experiments.

At first, a biotin-modified double-stranded DNA (dsDNA), which was labelled with Cy3B (donor) and Atto647N (acceptor) in 13 bp distance was studied (Figure 4.25A). And this can be used as a reference sample to allow a direct comparison of µs-ALEX and TIRF data (Figure 4.25A-C). For this, the dsDNA was immobilized on a PEG-coated glass surface via streptavidin-biotin interactions. The dsDNA sample displays an apparent FRET efficiency E* of ~0.64 for in-solution measurements (Figure 4.25B, µs-ALEX), which agreed well with the analysis of surface-immobilized molecules on the TIRF microscope having a mean E* of 0.62 (Figure 4.25C). The red trace in Figure 4.25C indicated the fluorescence intensity of acceptor, the green trace represented the donor intensity, and the black was the FRET efficiency.
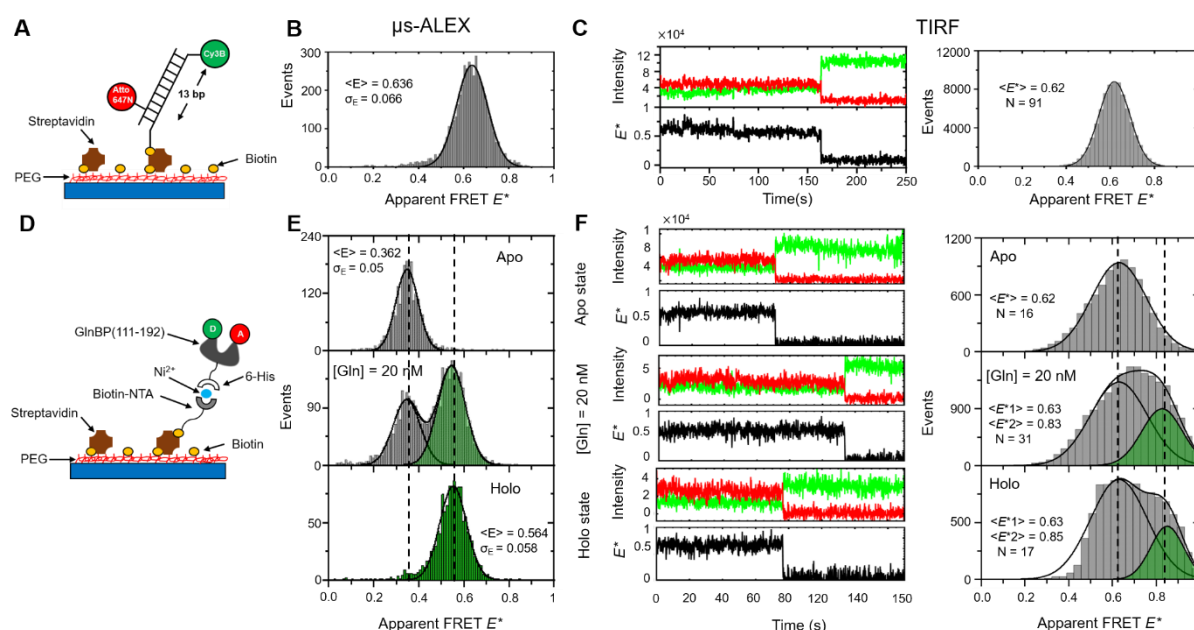
Figure 4.25. Comparing smFRET measurements of biotin-modified dsDNA and GlnBP(111-192) using diffusion-based µsALEX versus TIRF microscopy. (A) Schematic view of dsDNA labelled with Cy3B and Atto647N for smFRET characterization on PEGylated coverslips. (B) Typical µs-ALEX-based E*-S* histograms of the biotin-modified dsDNA labelled with Cy3B and Atto647N. (C) Representative fluorescence time trace of respective single emitter of the biotin-modified dsDNA sample under continuous wave excitation of ~500 µW at 532 nm and the FRET histograms of all analyzed molecules and the FRET histograms

of all measured molecules combined. (D) Schematic view of the refolded GlnBP(111-192) labelled with Atto532-Atto643 for smFRET characterization. (E) Typical µs-ALEX-based E*-S* histograms of the refolded GlnBP(111-192). (F) Representative fluorescence time trace of respective single emitter of the refolded GlnBP(111-192) under continuous wave excitation of ~500 µW at 532 nm and the FRET histograms of all analyzed molecules.

The fluorescence time traces of the dsDNA samples on TIRF were shown in Figure 4.26. The green traces indicated the signal of donor, red traces indicated the signal of acceptors and the black one represented the FRET efficiency.
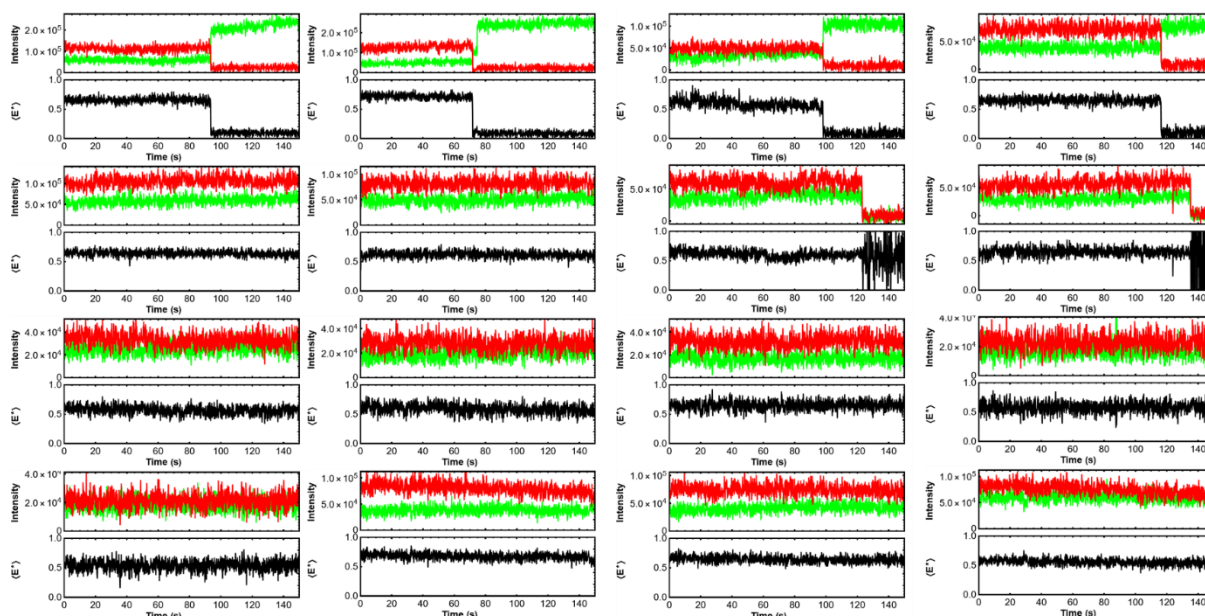
Figure 4.26. Representative fluorescence time traces of respective single emitter of biotin-functionalized DNA labelled by maleimide-modified derivatives Cy3B and Atto647N (13bp inter-dye distance). All measurements were done in oxygen scavenging buffer (3 U/ml of pyranose oxidase, 90 U/ml of catalase and 40 mM glucose, PBS buffer, pH 7.4). Laser power: 500 µW.

Then, the conformational states and changes of the GlnBP variants with TIRF microscopy were investigated. The refolded GlnBP(111-192) was labelled with commercial maleimide derivatives of ATTO532 (as donor) and ATTO643 (as acceptor) (Figure. 4.25D). Both donor and acceptor fluorescence were recorded

using a dual-view split on an EMCCD camera with a 100 ms integration time per frame. Under continuous wave excitation of approximately 500 µW at 532 nm, traces lasting multiple tens of seconds with good signal-to-noise and signal-to-background ratios were obtained. Because there was no millisecond alternation of green and red laser excitation, it was verified that the signal-sum of the donor and acceptor channels remained constant as a function of time for each molecule, and traces that did not meet this condition were discarded.

According to the results, the conformational states of GlnBP were strongly altered upon surface immobilization (Figure 4.25F), i.e., the E* values of GlnBP in apo/holo-state was significantly higher than in solution. Furthermore, GlnBP did not retain its biochemical activity on the glass coverslips (i.e., < 50 % of all GlnBP molecules showed a shift of conformational states upon addition of the ligand (Figure 4.25F). The fluorescence time traces of the GlnBP on TIRF were shown in Figure 4.27
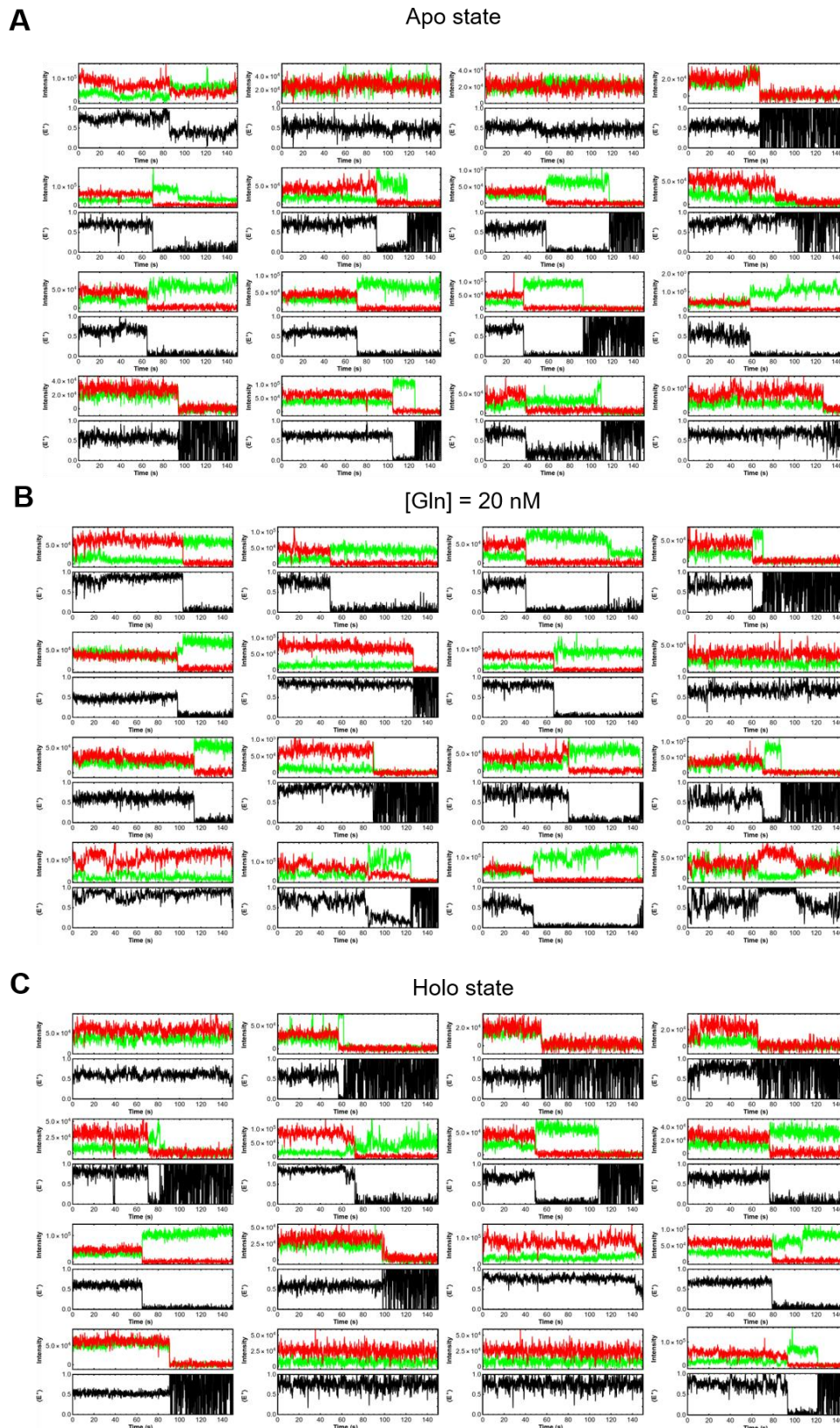
Figure 4.27. Examples of fluorescence time traces of respective single emitter of refolded GlnBP(111-192) labelled by maleimide-modified derivatives Atto532 and Atto643. All measurements were done in PBS buffer, pH 7.4 and 2 mM Trolox. Laser power with continuous 532 nm excitation: 200 µW.

To further eliminate the possibility that our experimental protocol is flawed, two previously studied proteins SBD1 and SBD2 were investigated on μsALEX and TIRF microscopy. First, the two proteins were labelled with ATTO532/ATTO643 respectively, and then purified with SEC (Figure 4.28 A/D). Subsequently, both labelled proteins were studied on μsALEX, they adopted an apo state without ligand and a closed conformation with high concentration of ligand (Figure 4.28B/E). Finally, the two proteins were measured on TIRF microscopy, and the FRET efficiency were internally consistent with the μsALEX data (Figure 4.28 C/F), which indicated that GlnBP cannot be immobilized on the slides and its initial conformation would be impacted.
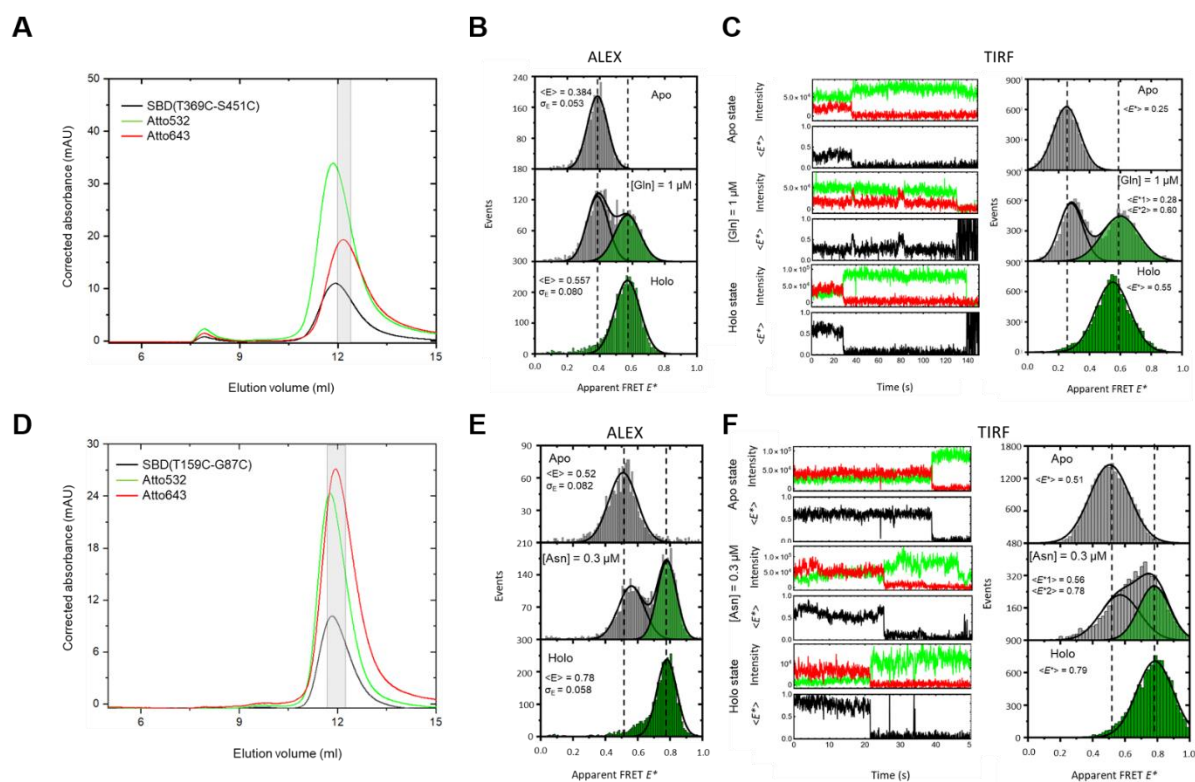
Figure 4.28. (A) and (D) Size exclusion chromatography (SEC) of SBD(T369C-S451C) and SBD(T159C-G87C). The selected fractions (grey shaded area) were collected and used for the solution-based smFRET measurements. The selected fractions (grey shaded area) having the best overlap of protein, donor, and acceptor absorption were used. The protein absorption was measured at 280 nm (black curves) and the donor dye (Atto532) absorption at 532 nm. The acceptor dye absorption (red lines) was measured at 643 nm for Atto643. (B) and (E) Typical μs-ALEX-based E*-S* histograms of the SBD(T369C-S451C) and SBD(T159C-G87C). (C)

and (F) Representative fluorescence time trace of respective single emitter of the SBD(T369C-S451C) and SBD(T159C-G87C) and the FRET histograms of all measured molecules.

In summary, the obtained TIRF data suggests that surface immobilized GlnBP adopts an altered conformational state that is (at least partially) non-functional. Thus, TIRF studies of the labelled protein cannot be used for mechanistic studies of GlnBP due to the artefactual nature of the data and the fact that part of the observed GlnBP are likely in a non-native states, which renders previous results questionable[41, 43, 44].

4.2.8 Toward an elucidation of the ligand binding mechanism via monitoring ligand binding and dissociation kinetics.

To complement the available information on conformational changes, surface plasmon resonance (SPR) spectroscopy was performed to obtain kinetic information on the association and dissociation steps of ligand binding. For this the GlnBP was immobilized on a sensor chip via its His-tag to monitor its interaction with glutamine. Even though GlnBP became partially inactive during immobilization for smFRET in TIRF microscopy (see previous section), we reasoned that non-functional GlnBP will not be observed in SPR since only functional protein can contribute to the overall signal changes. It is important to highlight that SPR and smFRET have a distinct ability to monitor protein ligand complex formation. SPR exclusively monitors a mass increase in the vicinity of the chip, i.e., on the immobilized protein and with that protein-ligand interaction. Since conformational changes are not seen, SPR can monitor formation of final CL state for the CS mechanism, but only the intermediate OL complex formation for IF. It is inverse for smFRET which allows to follow formation of the CL state for IF, but it cannot discriminate between C and CL state in the CS mechanism and would here monitor an intermediate state C in the ligand binding pathway.

In SPR, GlnBP showed specific and stable interaction with glutamine based on the magnitude of the equilibrium RU response as a function of glutamine concentration (Figure 4.29A). Analysis of the concentration-dependent maximal RU units and fitting to a simple Hill binding model with no cooperativity yields a Kd of 21 nM (Figure 4.29B). The overall maximal response of around 3 RU, indicates a 1:1 stoichiometry of glutamine assuming a monomeric state of GlnBP. The association experiments were conducted under pseudo-first order conditions ([Gln] = const.) due to the applied flow and showed a positive (linear) correlation between the observed association rates k_{obs} and the ligand concentration (Figure 4.29C). Under these conditions, a Langmuir model can be applied in which all rate constants can be determined considering that the equilibration takes place with the observed concentration dependent association rate $k_{obs} = k_{on}*[Gln] + k_{off}$ and dissociation follows a first order decay with k_{off}: concentration dependent second order rate constant $k_{on} = (4.5 \pm 2.3)*10^6\ M^{-1}\ s^{-1}$ and first order dissociation rate $k_{off} = (5.4 \pm 2.2)*10^{-2}\ s^{-1}$ (Figure 4.29A). Based on these values we obtained a kinetically derived dissociation constant ($K_d = k_{off}/k_{on}$) of 18 ± 16 nM as an internal control, which agreed well with all other data presented here.
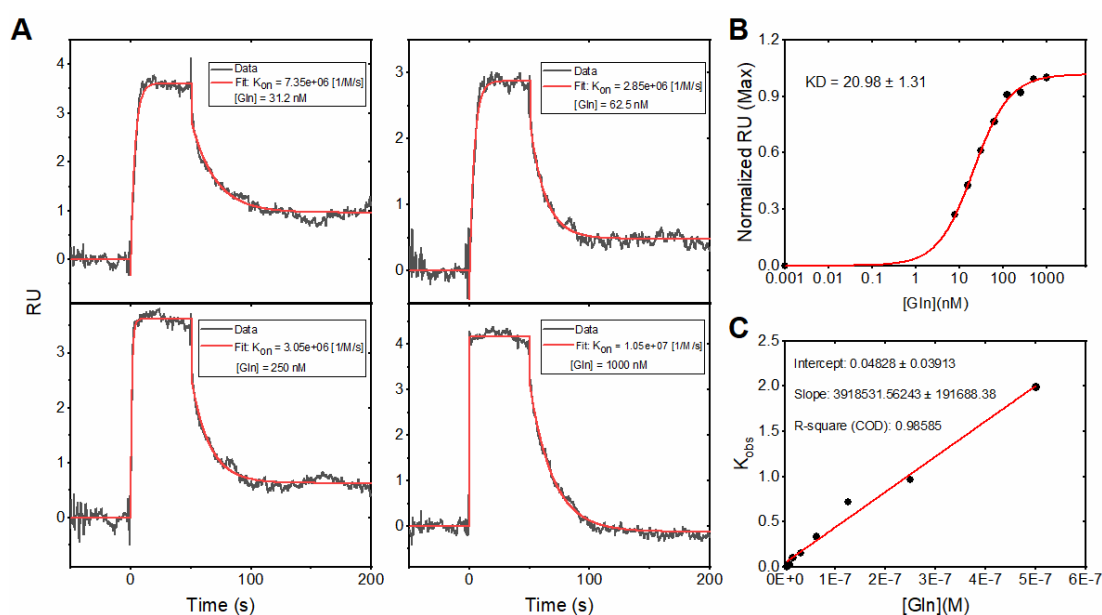
Figure 4.29 Kinetic analysis of ligand binding and dissociation in GlnBP using SPR. (A) SPR sensorgram for association, equilibrium, and dissociation phases for four different ligand

concentrations as indicated. Globally derived k_{on} and k_{off} rate constants from the Langmuir model are indicated in the respective panel. (B) Determination of K_d values from normalized equilibrium responses of the SPR from single-cycle kinetics. (C) Linear correlation between glutamine concentration and observed equilibrium rate.

While the obtained SPR results match all other data presented seemingly, the positive (linear) correlation between the observed association rates k_{obs} and the ligand concentration (Figure 4.29C) implies a kinetic scheme for a reversible single-step binding process. Any process with higher complexity, i.e., two-step binding with conformational change where rate constants for both processes are in a similar range, should show sigmoidal behaviour of k_{obs} vs. [Gln]. This suggests to us that conformational motion is much faster in GlnBP than ligand binding to the protein itself.

4.2.9 Accessibility of the ligand binding pocket for solvent and ligand in the closed conformation of GlnBP.

To further describe the expected binding behavior of the substrate, Gln, to the protein, GlnBP, docking calculations of Gln to GlnBP was performed in its open and closed conformations (Figure 4.30). The GlnBP structure that represents the open conformation is the one reported under pdb code 1GGG. The GlnBP structure that represents the closed conformation is the one reported under pdb code 1WDN, with the bound Gln substrate taken out of the file.
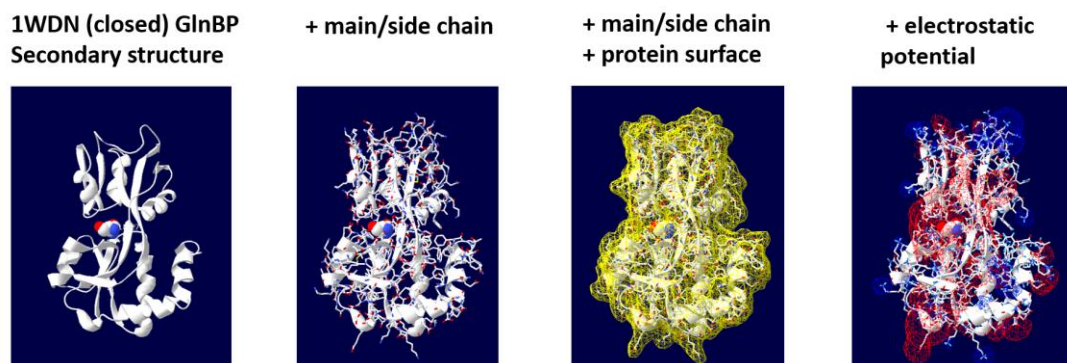
Figure 4.30. The structure of holo-GlnBP with optimized docking of Gln. The figure reports the optimized results of docking Gln onto the crystal structure of GlnBP in Holo form, after the Gln substrate was removed from the structure, and presented back as a docking ligand using the SwissDock web server. From left to right: (i) the Gln is docked onto the correct binding pocket within the closed conformation of GlnBP, (ii) amino acid side chains are wrapping the docked Gln from all directions, (iii) and indeed the protein surface covers the docked Gln, and (iv) the residues covering the docked Gln seem to carry a net negative charge.

Then, we used the 3D conformer structure of Gln as the ligand to be docked onto the structures of GlnBP. We used the SwissDock web server to perform the docking procedure.[77, 78] The results show that (i) while Gln can dock to many sites on GlnBP, the results that yield the lowest binding free energy are when it docks onto its cognate binding site, both in the open and closed conformation (Figure 4.30, Figure 4.31); (ii) the calculated binding free energy of Gln to GlnBP in the optimized docking site leads to a dissociation constant of 20 uM in the open conformation and 230 nM in the closed conformation (Figure 4.31), about two orders of magnitude stronger; (iii) The stronger binding free energy is due to the larger amount of GlnBP residues the docked Gln interacts with in the closed conformation relative to in the open conformation; (iv) the binding pocket in GlnBP seems to surround the docked Gln from all directions (Figure 4.30), which implies that the it is less probable to assume Gln can reach the binding pocket in the closed conformation. Instead, it is more probable that the Gln can reach its binding site in GlnBP when it is not yet fully closed.

1GGG (open) GlnBP
Gln SwissDock result – K_D = 20 μM

1WDN (closed) GlnBP
Gln SwissDock result – K_D = 230 nM
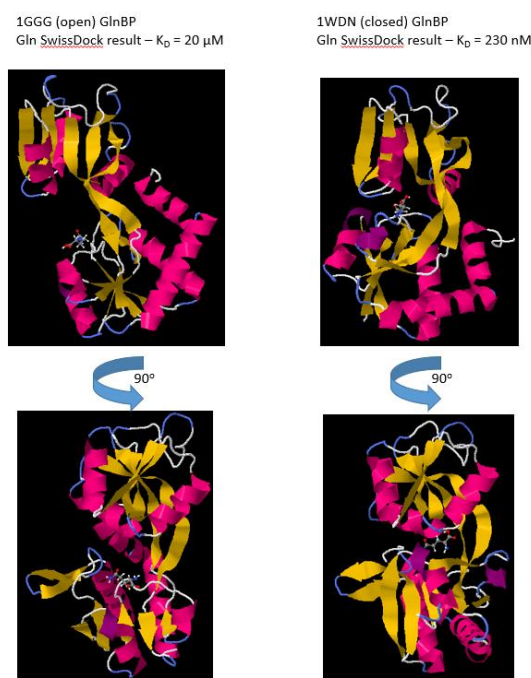
Figure 4.31. Optimized docking of Gln to GlnBP in its open and closed conformations. Using the SwissDock web server, the molecule Gln was docked onto the crystal structures of GlnBP in its open (pdb:1GGG) and closed (pdb:1WDN; with the Gln substrate taken away) conformations, and the optimized docking sites as well as the calculated dissociation constant are shown (dissociation constant is calculated out of the binding energies reported in the docking results). The preferred docking of Gln is the same site within GlnBP. The difference is that while in the open conformation Gln binds to one domain with the other as a distant domain, in the closed conformation the other domain closes on top of the docked Gln. Following the calculated binding energies from the optimized docking results, while the dissociation constant of Gln to GlnBP is 20 uM in the open conformation, in the closed conformation it is 230 nM.

Overall, these data are fully compatible with the idea that GlnBP uses ligand-binding mechanism where the ligand induces the relevant conformational change due to the full consistency data of all data with the characteristics of an induced fit. This, however, also reveals strong discrepancies between our TIRF data (and interpretations) on GlnBP and those reported by others[41, 43, 44]. According to our studies, it is much likely that GlnBP binds with L-glutamine via an induced-fit mechanism.

5   Discussion and conclusion

5.1 Discussion and conclusion of the performance of conformationally restricted cyanine dyes in smFRET.

With the development of single-molecule fluorescence imaging microscopy, it turned out to be essential to improve fluorophore properties including photostability via suppression of dark states to monitor single molecules in advanced microscope [79-81]. Cyanines have been dyes of choice in many modern techniques. However, its applications in single-molecule fluorescence microscope measurements are limited due to its inherent *trans-cis* isomerization [21], which could lead to blinking dynamics on the microsecond time scale. Therefore, our collaborators optimized the synthesis and evaluation of conformationally restricted pentamethine cyanines to improve its photostability. Therefore, the structure restricted cyanine dyes cannot have the *trans-cis* transition that could improve the photostability.

5.1.1   Are the conformationally restricted cyanine dyes much stable than normally used dyes on smFRET?

Here, to prove the stability of the conformationally restricted cyanine dyes, the solution-based smFRET measurements were performed using double-cystein MalE variant (Thr36Cys-Ser352Cys), which adopts an open state and a closed state in the absence and presence of ligand and is labelled with commonly used maleimide-modified fluorophore pairs (donor fluorophore AF555 and acceptor fluorophores AF647, Atto647N, Cy5B-monosulfo and Cy5B-trisulfo), to characterize and compare the properties of acceptor dyes.

The cleanest 2D-E*-S histograms, which shows very low indications of photo bleaching, were obtained by using Cy5B-trisulfo (Figure 4.4). To further compare the acceptor fluorescent dyes quantitatively, the acceptor photon count rates with powers of 25 μW for the red excitation laser and 60 μW for the green laser

excitation laser were analyzed. The results confirmed that all the acceptor dyes have similar brightness in the ligand-free state of MalE, but Cy5B dyes showed less brightness than AF647 and Atto647N fluorophores in the ligand-bound state of MalE (Figure 4.4, Figure 4.6A/B). Hence, this suggested that less FRET burst can be obtained for AF555-Cy5B-monosulfo and AF555-Cy5B-trisulfo.

5.1.2 The advantages of cyanine dyes under higher laser power.

Nevertheless, the laser power dependence experiments were conducted on µsALEX microscopy. According to the laser power dependence on solution-based smFRET measurements, it can validate that Cy5B fluorescent dyes showed the unique advantage among both Atto647N and AF647 acceptor dyes due to the absence of *trans-cis* isomerization. In the open state of MalE, Cy5B derivatives showed reduced bridge artifacts and maintain the mean E^* position and width σ_E of the population over the entire range of excitation power studied (Figure 4.6C, Figure 4.7). In addition, Cy5B-trisulfo has a small deviation in the peak position but was similar to the one using the Atto647N fluorophore.

Conclusively, all the findings suggested that Cy5B derivatives can be utilized as suitable alternatives to AF647 and Atto647N in solution-based smFRET measurements. Furthermore, these fluorophores can be used to reduce the blinking and bleaching artifacts. Additionally, Cy5B fluorescent dyes behaved very well under the higher laser power condition, which maybe could be used in the high temporal resolution experiments.

5.2 Discussion and conclusion of ligand binding mechanism of GlnBP.

Conformational states of macromolecular complexes and changes thereof govern numerous cellular processes. While many conformational changes that are triggered by ligand have been characterized intensively it has also become evident that proteins exhibit prominent intrinsic structural dynamics without the involvement of ligands or other biomacromolecules[24, 26, 34, 82-90]. These observations gave rise to the idea that ligand-binding can proceed via distinct mechanistic pathways, i.e., ligand binding occurs before conformational change (induced fit, IF) or conformational change occurs before ligand binding (conformational selection, CS)[91].

5.2.1 Biochemical characterization of refolded GlnBP WT and GlnBP variants.

As reported previously, GlnBP copurifies with bound glutamine during overexpression. This could impact the initial conformational detection of GlnBP. Thus, the unfolding and refolding processes were conducted. First, considering the multimer formation during dialysis procedure, the refolded proteins were check via SEC which could validate the size of the protein to distinguish the complexes exit or not (Figure 4.10B). Second, to confirm the initial binding affinity of the refolded GlnBP WT and GlnBP variants, the ITC measurements could solve the question (Figure 4.11). The Kd values of refolded GlnBP and variant matched with the reported data. Given that, the unfolding/refolding and cysteine substitutions did not impact the biochemical properties of GlnBP.

5.2.2 Conformational motion of GlnBP variants using smFRET measurements.

Diffusion-based smFRET is a well-established method to study conformational changes of biomacromolecules in aqueous solution at ambient temperature. As shown previously, smFRET can be used to study SBP conformational heterogeneity, identify small sub-populations and determine microscopic rates for conformational change, which makes the technique an ideal complement for the biochemical analysis of GlnBP. According to the smFRET results of both mutants, the protein only transferred to a closed state when ligand (500 nM) was added (Figure 4.14). Furthermore, no detectable closed state population was observed in the absence of ligand. Importantly, a quantitative analysis of the closed state population as a function of ligand concentration allowed the determination of a ligand-protein affinity of 20-50 nM for all protein variants (Figure 4.18), which is consistent with our ITC results. The results are consistent with the idea that GlnBP mainly exists in a single state, the open conformation, in the absence of glutamine, and that the closed conformation only exists in the presence of the glutamine.

5.2.3 Surface-immobilized GlnBP changes its initial conformations using TIRF microscopy.

TIRF measurements can characterize the protein and its conformational dynamics on slower timescales (i.e., >100 ms). This strategy was appealing to us since we hoped to obtain information on rare conformational events, which are better observed in surface-immobilized smFRET experiments due to longer observation times.

Strikingly, in the analysis of immobilized donor-acceptor-labelled GlnBP, various buffer additives could influence the conformational state of GlnBP (Figure 4.24) and that the conformational states of GlnBP were strongly affected upon surface immobilization. Furthermore, GlnBP did not remain biochemically active on the

glass coverslips (Figure 4.25E/F), i.e., <50% of all molecules showed no ligand binding. But dsDNA (Figure S12) and control proteins SBD1 and SBD2 (Figure S15), which measured on the same TIRF microscopy, where both μsALEX (freely diffusing GlnBP) and TIRF data (immobilized GlnBP) were internally consistent (Figure 4.25B/C, Figure 4.26). It was concluded that the TIRF data generated for GlnBP was not suitable for mechanistic interpretation.

5.2.4 The SPR could distinguish the binding mechanism?

To advance further checking the dissection of GlnBP binding mechanism, the available kinetic information on ligand binding and conformational changes were performed using SPR (Figure 4.27). The kinetic hallmark of the CS mechanism is a reduction of the observed equilibration rate k_{obs} for protein-ligand complex formation for increasing ligand concentrations in contrast to increasing k_{obs} values for IF[91-94]. Such a diagnostic contrast is, however, only seen under pseudo-first order conditions and the rapid equilibrium approximation where binding and dissociation are assumed to be fast compared to conformational changes. In SPR, we find linearly increasing k_{obs} for increasing ligand concentration, which suggests that either IF or CS could be active, but also that conformational is fast in comparison to ligand binding. Thus, to be able to exclude limiting scenarios, the SPR measurements should be repeated, and the data would be further deeply analysed to get more information to decipher the binding mechanism of GlnBP.

Based on all presented results, their internal consistency and also the reports of others[45-47, 61], we render it implausible that apo-GlnBP shows slow prominent intrinsic conformational motions into (semi-)closed in the absence of ligand or that the closed holo-state fluctuates in the presence of high-ligand concentrations as reported by Wang, Yan and co-workers[41, 43, 44]. In all our assays, ligand binding and conformational motion are highly correlated, and any FRET dynamics could be traced back to photophysical origin. All this still leaves us,

however, with the question about the ligand binding mechanism (IF/CA) used by GlnBP.

Often, the existence of a ligand-free protein conformation is taken as an indicator for CS as a dominant pathway[95]. Importantly, the first prerequisite for this mechanism to be active is a steric one. If a protein fully engulfs the ligand in its closed conformation, a CS mechanism cannot be realized via a simple two-state system, since the ligand is not able to diffuse into the binding pocket. For GlnBP – as for many other binding proteins[96] – the open conformation seems much more likely to bind substrate than the closed. So, the existence of a ligand-free protein conformation that structurally resembles a ligand-bound form is a necessary, but insufficient evidence for the operation of a CS mechanism, as ligand binding may not proceed via this conformation at all. Whether a ligand-free closed (or near closed) conformation[97] can be observed depends on the magnitude of its equilibrium probability as well as the sensitivity of the techniques used to probe it. Nevertheless, an inability to detect such ligand-free (closed) conformations is often taken as an indicator for IF as a dominant pathway, again based on insufficient evidence. We clearly state that for GlnBP there will be intrinsic conformational changes, which we were, however, not able to detect.

In smFRET, we find, however no clear evidence for intrinsic conformational motion of apo-GlnBP. Such dynamics may, however, occur with low probability < 5 % and might occur on very fast timescales < 100 µs or slow timescales > 10 ms. To be able to exclude limiting scenarios, we next discuss the plausibility of the hypothetical scenario for CS to occur in GlnBP: If GlnBP used the CS, the apo-GlnBP would need to show sampling of the (semi-)closed conformation with rates < 1-10 s^{-1} with low abundance (<5 %) since we were not able to detect this state (or transitions into the state) in our smFRET experiments. Overall, the GlnBP is very likely to use the "induced-fit" binding mechanism.

6   Summary & Outlook

6.1   Summary

Diffusion-based smFRET[7, 14, 71] has become a general method for studying the conformational dynamics and structural changes of SBPs, an application in which brightness and dye stability play important roles. In smFRET measurement, the bleaching and blinking of fluorescent dyes can lead to an artificial shift in the efficiency of FRET and, thus, the determined distance between donor and acceptor fluorophores. Therefore, in this work, we compared the target conformationally restricted cyanine dyes (Cy5B-monosulfo and Cy5B-trisulfo) with the commonly used maleimide-modified AF647 and Atto647N on MalE, which is considered as a protein system. We summarize that Cy5B fluorescent dyes cannot improve photon output compared to AF647 and Atto647N in smFRET measurements, but Cy5B fluorophores reduce blinking and bleaching artifacts and preserve narrow FRET peaks. In addition, Cy5B fluorescent dyes behaved very well at higher laser powers, making these fluorophores suitable for extracting accurate distances from complex bimolecular systems when higher laser power or higher temporal resolution is required.

Protein conformational dynamics play a crucial role in protein-ligand interactions. However, the underlying mechanisms of these interaction are often poorly understood. Recent studies concluded that *E. coli* GlnBP, a typical PBP, which can bind *L*-Gln, undergoes intrinsic conformational changes using smFRET microscopy. This intrinsic conformational flexibility is highly unexpected considering everything we know about SBPs. Thus, we performed ITC, solution-based smFRET experiments, BVA and mpH^{2}MM analysis, MFD-PIE microscopy and surface-immobilized smFRET measurements for a detailed study on GlnBP to decipher its intrinsic conformational dynamics. Overall, our study highlights the relevance and necessity of obtaining information on structural dynamics in proteins using an array of complementary techniques to assure proper function of

the non-native protein system under study. We conclude that GlnBP binds with L-Gln through the induced-fit mechanism and, in addition we suggest—supported by our experimental results— the existence of only two conformational states in solution, i. e. an open and a closed conformational state. Both conformational states are static in the absence and the presence of saturating ligand concentration. Furthermore, the open to closed conformational transition occurs slowly at low ligand concentrations.

6.2   Outlook

6.2.1   Alternative assays to assess biomolecular structure:

Structural dynamics of proteins can be seen by smFRET with the restriction that two-colour monitoring is required for the assay. A simplification would be to contact-induced fluorophore quenching which requires the observation of only one fluorescence colour. The self-quenching of two rhodamine derivatives (tetramethylrhodamines, TMR) can be used to detect the small conformational dynamics at the single molecule level[98]. During preparation of this thesis, I contributed to the development of such assays based on TMR-labelled biomacromolecules (DNA and proteins) samples (Figure 6.1) using fluorescence correlation spectroscopy (FCS) and μsALEX. Within the project, I collaborated with my colleague Rebecca Mächtel (see thesis) where more details on this project are described.
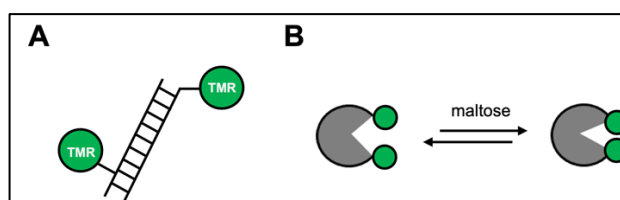

Figure 6.1 (A) The schematic of the DNA sample labelled with identical TMR dye in various distance. (B) The MalE protein labelled with identical TMR dyes.

As reported before, two photophysical processes need to be considered in the assays seen in Figure 6.1. The identical TMR fluorophores in close proximity can stack and form a quenched dimer[98]. Also Förster resonance energy transfer (FRET), known as Homo-FRET, can be observed and allows e.g., for quantification of molecular clusters[99]. To investigate the distance relation of both processes between the two TMR fluorophores, we designed a series of DNA samples which are labelled with two identical TMR fluorophores at various positions to obtain information on molecular brightness using fluorescence correlation spectroscopy (FCS)[100].

Figure 6.2. Fluorescence correlation spectroscopy (FCS) measurements of DNA samples labelled with identical TMR fluorophores. B: brightness, N: molecule number in the confocal volume, κ: aspect ratio, τ_D: diffusion time and T: triplet fraction.

As shown in Figure 6.2, we employed FCS to measure the TMR labelled DNA samples in which the brightness, molecule concentration, aspect ratio, diffusion time and triplet fraction components were extracted (Figure 6.2). In contrast to the singly labelled DNA samples (Figure 6.3), T1T5-TMR and T5T7-TMR labelled DNA samples have lower brightness and higher triplet fraction due to the small distance between the identical TMR fluorophores. The parameters were summarized in the Table 6.2.
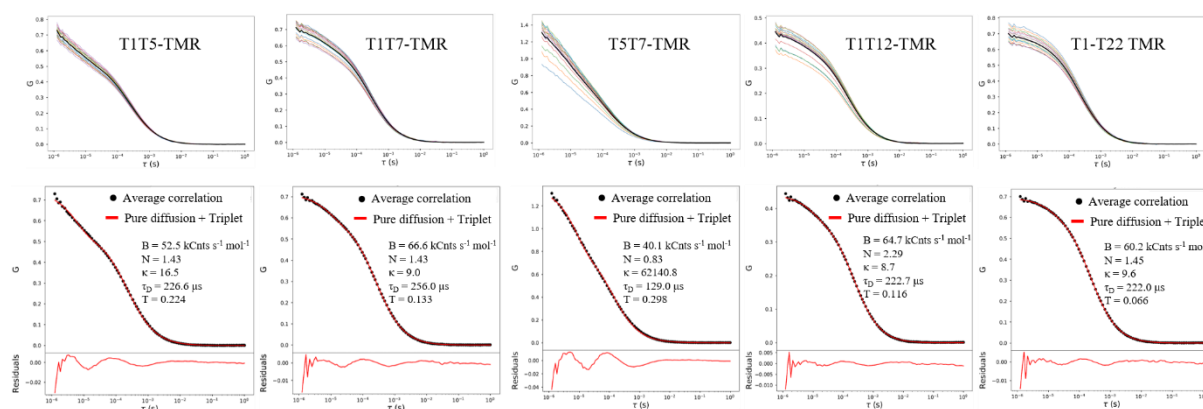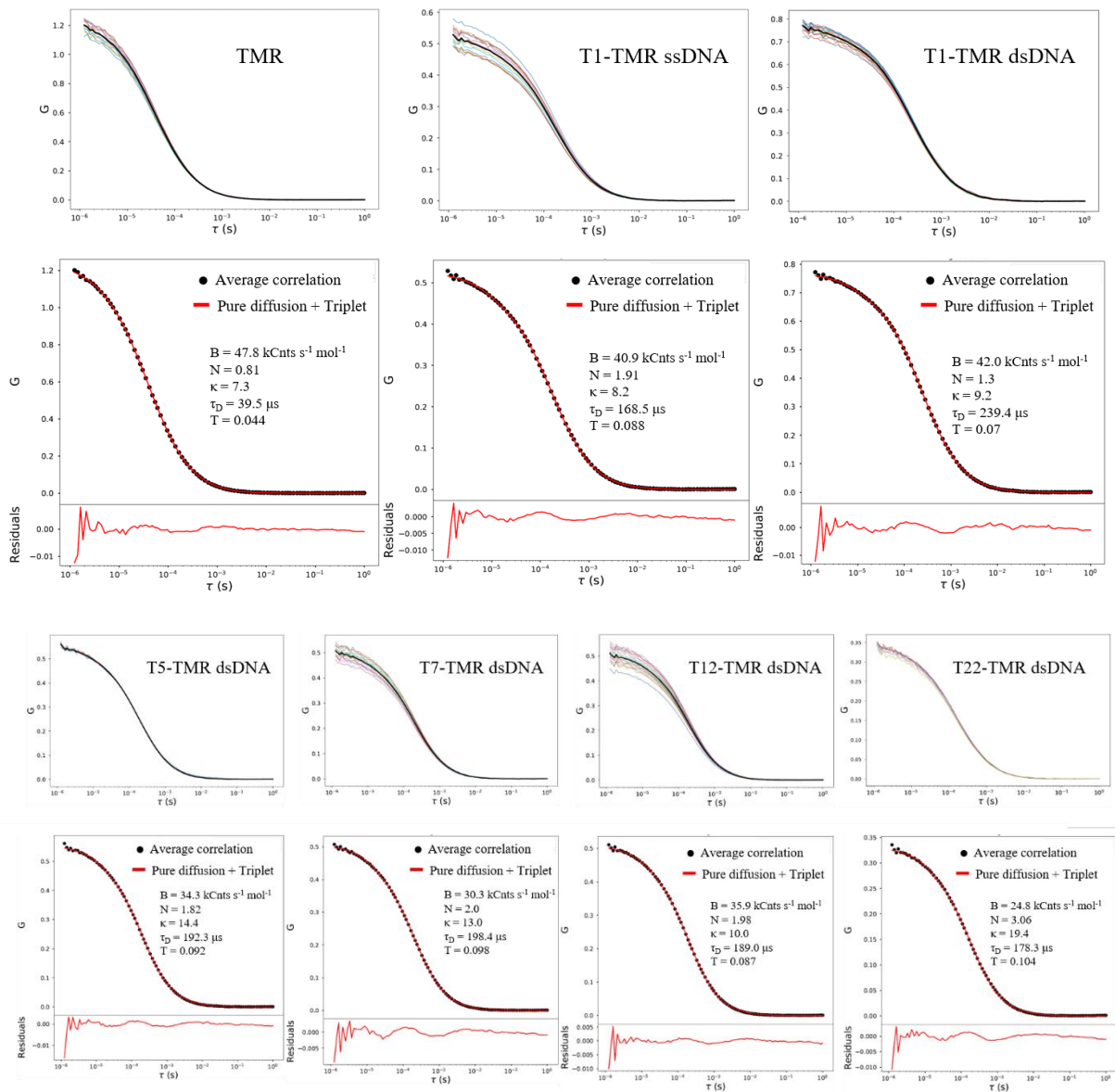
Figure 6.3. Fluorescence correlation spectroscopy (FCS) measurements of DNA samples labelled with identical TMR fluorophores. B: brightness, N: molecule numbers, κ: aspect ratio, τ_D: diffusion time and T: triplet fraction.

Table 2 FCS results of TMR-labelled DNA samples.

	TMR	T1-TMR ssDNA	T1-TMR dsDNA	T5-TMR dsDNA	T7-TMR dsDNA	T12-TMR dsDNA	T22-TMR dsDNA	T1T5-TMR dsDNA	T1T7-TMR dsDNA	T5T7-TMR dsDNA	T1T12-TMR dsDNA	T1T22-TMR dsDNA
Brightness (kCnts s^{-1} mol^{-1})	47.8	40.9	42	34.3	30.3	35.9	24.8	42.2	61.9	35.2	54	49.6
Diffusion time (μs)	39.5	168.5	239.4	192.3	198.4	189	178.3	224.3	238.3	126.8	216	212.9
Triplet fraction	0.044	0.088	0.07	0.092	0.098	0.087	0.104	0.224	0.14	0.303	0.1	0.067

Furthermore, Homo-FRET could be identified by evaluating the loss of fluorescence anisotropy and lifetime after polarized light excitation on the home-built microscopy. The samples labelled with two identical TMR dyes were measured, and the lifetime and anisotropy values were recorded (Figure 6.4). Meanwhile, the single labelled DNA samples were also measured which could be used as the control to compare the lifetime and anisotropy values with the double labelled samples.
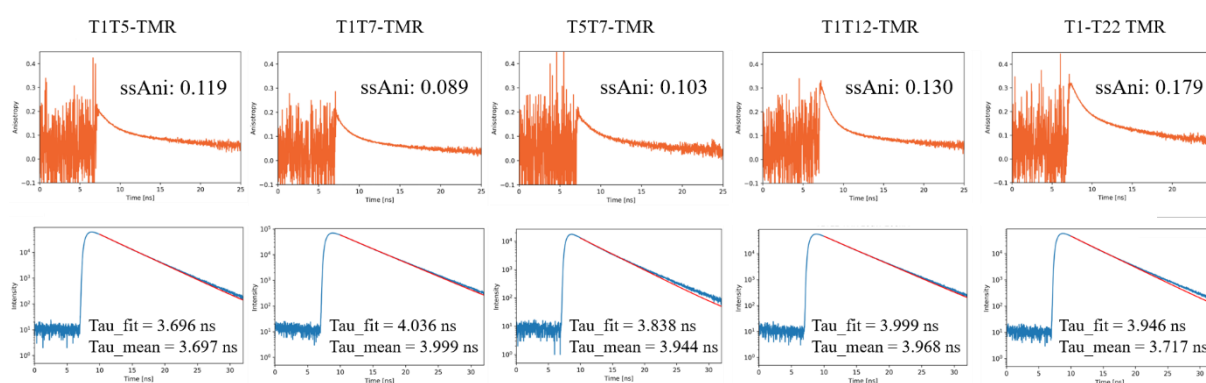

Figure 6.4 Anisotropy and lifetime measurements of DNA samples labelled with identical TMR fluorophores.

From the results, we could conclude that T1T5-TMR and T5T7-TMR labelled dsDNA samples show higher anisotropy and shorter lifetime compared with other ssDNA/dsDNA samples (Figures 6.5) because of the short distance and self-quenching. The parameters were concluded in Table 3.
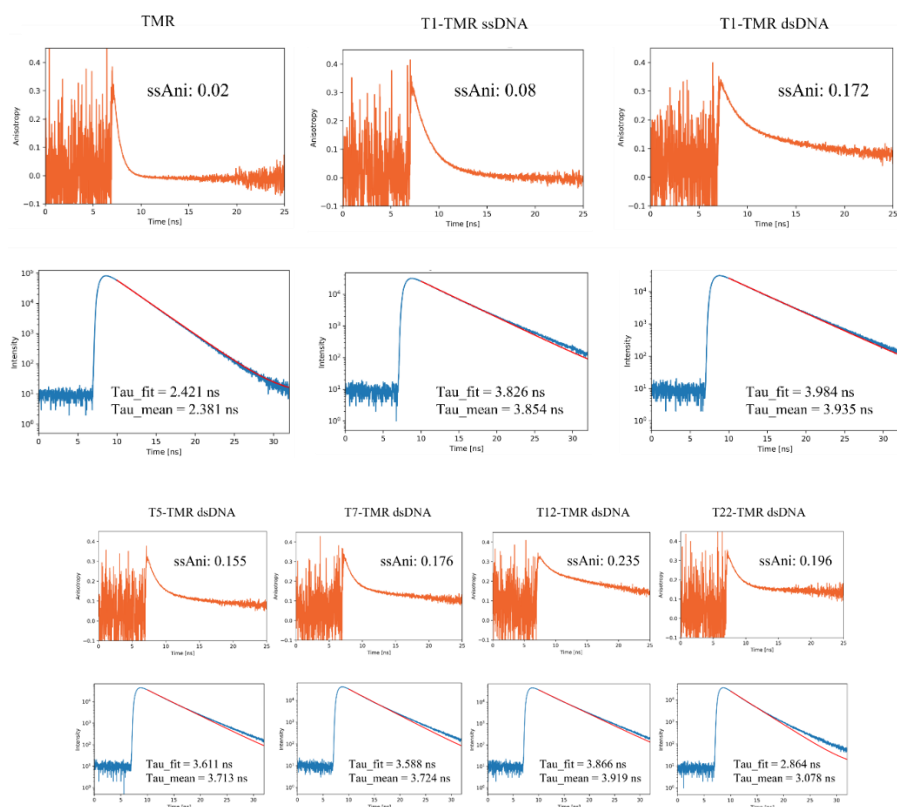
Figure 6.5 Anisotropy and lifetime measurements of DNA samples labelled with TMR fluorophores.

Table 3. Anisotropy and lifetime results of TMR-labelled DNA samples.

	TMR	T1-TMR ssDNA	T1-TMR dsDNA	T5-TMR dsDNA	T7-TMR dsDNA	T12-TMR dsDNA	T22-TMR dsDNA	T1T5-TMR dsDNA	T1T7-TMR dsDNA	T5T7-TMR dsDNA	T1T12-TMR dsDNA	T1T22-TMR dsDNA
Anisotropy	0.02	0.08	0.172	0.155	0.176	0.235	0.196	0.119	0.089	0.103	0.130	0.179
Lifetime (ns)	2.421	3.826	3.984	3.611	2.588	3.866	2.864	3.696	4.036	3.838	3.999	3.649

At current stage the systematics behind the distance dependence in the DNA samples (and proteins see PhD thesis of R. Mächtel) were not understood well-enough, so that further studies are required to use the self-quenching as an assay.

6.2.2 Improving photo budget of fluorophore via supramolecular chemistry:

Photostabilization is typically done in single-molecule assays as described in this thesis via triplet-state quenching using solution-additives or covalent coupling of these stabilizers. What has not been tested is the use of supramolecular chemistry approaches, which I also started to explore at the end of my thesis. Ferrocene is a potential candidate as photostabilizers because of its binding to a supramoelcular host and ability for triplet-state quenching. This approach would be to retain the benefits of organic fluorophores by incorporating them into a host that would increase their fluorescence intensity and photostability without considerably expanding their size [101].

Cucurbit[n]urils (CB[n]) are a class of macrocyclic host molecules that are commonly employed in synthetic and materials sciences due to their large size range and ability to complex various types of guest molecules in an aqueous environment. In particular, cucurbit[7]uril (CB7) is of interest due to its application on single molecule detection [101]. In addition, cucurbit[8]uril (CB8) also intrigues researchers because of its ability to host two guest moieties simultaneously [102]. Recently, we proposed two strategies to improve photo budget of fluorophore via supermolecular chemistry as described in (Figure 6.6).
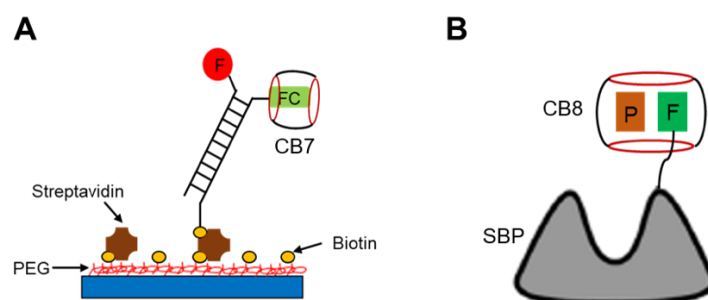

Figure 6.6. (A) Schematic view of dsDNA modified with fluorophore and Ferrocene (FC) for smFRET characterization on PEGylated coverslips. (B) SBP labelled with fluorophore conjugated with CB8 and photostablizer.

The quenching by the ferrocene occurs mainly via reductive and oxidative electron transfer on the ferrocenyl group. The CB7 could host the ferrocene the in the host that can block the electron transfer and improve the photon budget of fluorophores (Figure 6.6A). Cucurbituril has a large enough cavity to encapsulate both photostabilizers and fluorescent dyes at the same time, and it has been shown to boost dye brightness and photostability[103]. A compound combining cucurbituril, photostabilizer, and fluorophore is expected to have enhanced photophysical properties (Figure 6.6B). This concept could lead to the investigation of previously unknown mechanisms for innovative self-healing dyes.

To realize such approaches, we first characterized the binding of CB7 and CB8 with symmetric methyl viologens (M_2V) bearing electron-donating groups in a 1:1 and 1:2 binding fashion on the Job's plot (Figure 6.7B and D), respectively. The formation of such complexes led to interesting changes of their optical properties. We observed a uniform blue-shift in the absorption of the CB7-M_2V complexes relative to their UV/vis spectrum (Fig.6.7A) and decrease in the absorption of the CB8-M_2V complexes (Fig. 6.7).
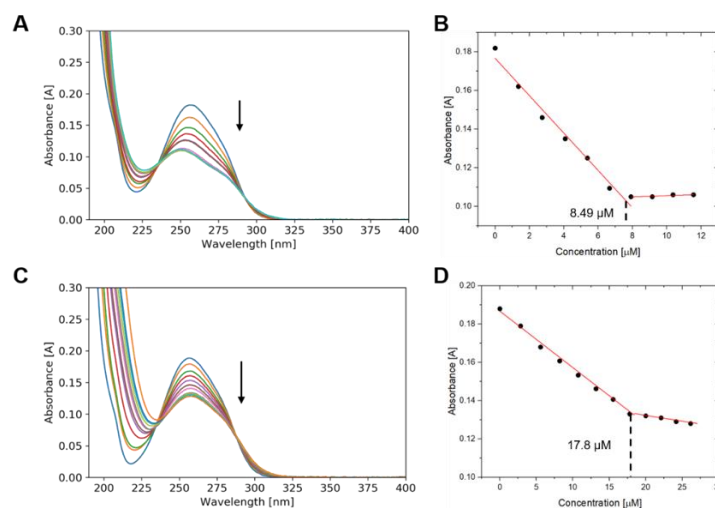
Figure 6.7. (A) Absorption studies for CB7-M_2V complexation on UV/vis spectrum. (B) Job's plot of CB7-M_2V complexation and the binding ratio is 1:1. (C) Absorption studies for CB8-M_2V complexation on UV/vis spectrum. (D) Job's plot of CB8-M_2V complexation and the binding ratio is 1:2.

To assess the binding affinity of CB7 for M$_2$V, (Dimethylaminomethyl)ferrocene (DAMF) and (Ferrocenylmethyl)trimethylammonium chloride (FTAC), we performed isothermal titration calorimetry (ITC) experiments (Figure 6.8). According to the ITC measurements, the binding affinity (Kd) and binding ratio could be extracted to evaluate the binding strength among the CB7 and specific substrate.
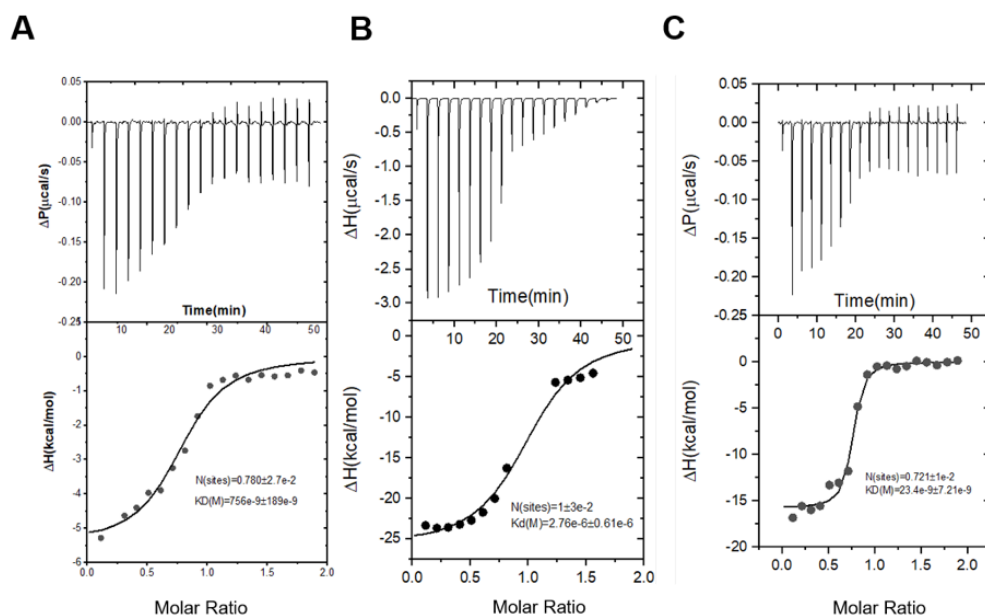
Figure 6.8. (A) Binding affinity measurements of CB7 for M2V, (B) DAMF and (C) FTAC.

Unfortunately, I have not finished this project before my graduation. Therefore, my colleague Siyu Lu will continue these experiments and further analyze the data in the future.

List of publications originating from this thesis

2   Patrick Eiring[+], Ryan McLaughlin[+], Siddharth S. Matikonda[+], **Zhongying Han**[+], Lennart Grabenhorst[+], Dominic A. Helmerich, Mara Meub, Gerti Beliu, Michael Luciano, Venu Bandi, Niels Zijlstra, Zhen-Dan Shi, Sergey G. Tarasov, Rolf Swenson, Philip Tinnefeld, Viktorija Glembockyte,* Thorben Cordes,* Markus Sauer* and Martin J. Schnermann*. Targetable Conformationally Restricted Cyanines Enable Photon-Count-Limited Applications. *Angew. Chem.* 2021, 133, 26889 – 26897.

[+] These authors contributed equally to this work.

2   **Zhongying Han**, Marija Ram, Sabrina Panhans, Anna Herr, Michael Isselstein, Sophie Brameyer, Kirsten Jung, Alessandra Narducci, Oliver Brix, Thomas Weikl, Ecenaz Bilgen, Don C. Lamb, Paul D. Harris, Eitan Lerner, Douglas Griffith, Niels Zijlstra* and Thorben Cordes*. Dissecting Mechanisms of Ligand Binding and Conformational Changes in the Glutamine Binding Protein (in final stage of preparation).

Acknowledgements

First, I would like to express my sincere gratitude to my supervisor Dr. Prof. Thorben Cordes, who supervised me through my doctoral studies. During my four years of Ph. D. I have learned a lot from you about research and the attitude of doing science. I also appreciate your help in revising my paper and thesis, which has been very beneficial to me. In addition, I am impressed by the activities and gatherings of the group.

I am also very grateful to Dr. Niels Zijlstra, who guided me when I first joined the group and helped me to get used to the group life and to learn some basic research knowledge in the new science field. Thank you very much for your active communication and problem solving when I encountered experimental problems. I am very impressed by the two years of working together.

In addition to that, I am very grateful to my colleagues Oliver Brix, Peng Zhou, Lei Zhang, Yuan Gu, Alessandra Narducci, Michael Isselstein, Christian Gebhardt, Douglas Griffith, Gabriel Moya, Marija Ram, Anna Herr and Liselotte van Dommelen, Rebecca Mächtel, for all the help you have given to me over these four years. It was four great years of working together. In addition to our lab work, we also went hiking and partied together. All of them will be wonderful memories to me.

I would also like to thank my Chinese Ph. D. friends in Germany, who helped me a lot in my daily life and impressed me with our travels together. I also wish you all the best in your research and life. I am sorry that I can't list all your names one by one due to the large number of friends.

I would also like to thank the China Scholarship Council (CSC) from the bottom of my heart for sponsoring my four years of study in Germany.

Finally, I would like to thank my families for your continuous support, which has allowed me to focus on my studies and research. I would also like to thank my

fiancée Jingxian Zhang. I am very sorry that I could not go back to be with you for three years because of the epidemic. But thank you for your understanding and support.

Thanks again to all of you, the temporary separation foreshadows the future meeting again. I hope you all have a wonderful future.

Reference

1. Fulyani, F., G.K. Schuurman-Wolters, A.V. Žagar, A. Guskov, D.-J. Slotboom, and B. Poolman, *Functional diversity of tandem substrate-binding domains in ABC transporters from pathogenic bacteria.* Structure, 2013. **21**(10): p. 1879-1888.

2. Hsiao, C.-D., Y.-J. Sun, J. Rose, and B.-C. Wang, *The crystal structure of glutamine-binding protein fromEscherichia coli.* Journal of molecular biology, 1996. **262**(2): p. 225-242.

3. Algar, W.R., N. Hildebrandt, S.S. Vogel, and I.L. Medintz, *FRET as a biomolecular research tool—understanding its potential while avoiding pitfalls.* Nature methods, 2019. **16**(9): p. 815-829.

4. Shrestha, D., A. Jenei, P. Nagy, G. Vereb, and J. Szöllősi, *Understanding FRET as a research tool for cellular studies.* International journal of molecular sciences, 2015. **16**(4): p. 6718-6756.

5. Stryer, L. and R.P. Haugland, *Energy transfer: a spectroscopic ruler.* Proceedings of the National Academy of Sciences, 1967. **58**(2): p. 719-726.

6. Ha, T., T. Enderle, D. Ogletree, D.S. Chemla, P.R. Selvin, and S. Weiss, *Probing the interaction between two single molecules: fluorescence resonance energy transfer between a single donor and a single acceptor.* Proceedings of the National Academy of Sciences, 1996. **93**(13): p. 6264-6268.

7. Lerner, E., T. Cordes, A. Ingargiola, Y. Alhadid, S. Chung, X. Michalet, and S. Weiss, *Toward dynamic structural biology: Two decades of single-molecule Förster resonance energy transfer.* Science, 2018. **359**(6373): p. eaan1133.

8. Herschel, J.F.W., *IV.'Αμόρφωτα, no. I.—on a case of superficial colour presented by a homogeneous liquid internally colourless.* Philosophical Transactions of the Royal Society of London, 1845(135): p. 143-145.

9. Berlman, I., *Handbook of florescence spectra of aromatic molecules*. 2012: Elsevier.

10. Eiring, P., R. McLaughlin, S.S. Matikonda, Z. Han, L. Grabenhorst, D.A. Helmerich, M. Meub, G. Beliu, M. Luciano, and V. Bandi, *Targetable Conformationally Restricted Cyanines Enable Photon - Count - Limited Applications*. Angewandte Chemie International Edition, 2021. **60**(51): p. 26685-26693.

11. Sauer, M. and M. Heilemann, *Single-molecule localization microscopy in eukaryotes*. Chemical reviews, 2017. **117**(11): p. 7478-7509.

12. de Boer, M., G. Gouridis, R. Vietrov, S.L. Begg, G.K. Schuurman-Wolters, F. Husada, N. Eleftheriadis, B. Poolman, C.A. McDevitt, and T. Cordes, *Conformational and dynamic plasticity in substrate-binding proteins underlies selective transport in ABC importers*. Elife, 2019. **8**: p. e44652.

13. Eiring, P., R. McLaughlin, S.S. Matikonda, Z. Han, L. Grabenhorst, D.A. Helmerich, M. Meub, G. Beliu, M. Luciano, and V. Bandi, *Targetable Conformationally Restricted Cyanines Enable Photon - Count - Limited Applications*. Angewandte Chemie, 2021. **133**(51): p. 26889-26897.

14. Lerner, E., A. Barth, J. Hendrix, B. Ambrose, V. Birkedal, S.C. Blanchard, R. Börner, H.S. Chung, T. Cordes, and T.D. Craggs, *FRET-based dynamic structural biology: Challenges, perspectives and an appeal for open-science practices*. Elife, 2021. **10**: p. e60416.

15. Albrecht, C., *Joseph R. Lakowicz: Principles of fluorescence spectroscopy*. 2008, Springer.

16. Sauer, M., J. Hofkens, and J. Enderlein, *Basic principles of fluorescence spectroscopy*. Handbook of Fluorescence Spectroscopy and Imaging, 2011. **1**: p. 30.

17. Hübner, C.G., A. Renn, I. Renge, and U.P. Wild, *Direct observation of the triplet lifetime quenching of single dye molecules by molecular oxygen*. The Journal of Chemical Physics, 2001. **115**(21): p. 9619-9622.

18. Davies, M.J., *Reactive species formed on proteins exposed to singlet oxygen.* Photochemical & Photobiological Sciences, 2004. **3**(1): p. 17-25.

19. Aitken, C.E., R.A. Marshall, and J.D. Puglisi, *An oxygen scavenging system for improvement of dye stability in single-molecule fluorescence experiments.* Biophysical journal, 2008. **94**(5): p. 1826-1835.

20. Stein, I.H., S. Capone, J.H. Smit, F. Baumann, T. Cordes, and P. Tinnefeld, *Linking Single‐Molecule Blinking to Chromophore Structure and Redox Potentials.* ChemPhysChem, 2012. **13**(4): p. 931-937.

21. Vogelsang, J., R. Kasper, C. Steinhauer, B. Person, M. Heilemann, M. Sauer, and P. Tinnefeld, *A reducing and oxidizing system minimizes photobleaching and blinking of fluorescent dyes.* Angewandte Chemie International Edition, 2008. **47**(29): p. 5465-5469.

22. Swoboda, M., J. Henig, H.-M. Cheng, D. Brugger, D. Haltrich, N. Plumeré, and M. Schlierf, *Enzymatic oxygen scavenging for photostability without pH drop in single-molecule experiments.* ACS nano, 2012. **6**(7): p. 6364-6369.

23. Holland, I.B., S.P. Cole, K. Kuchler, and C.F. Higgins, *ABC proteins: from bacteria to man.* 2003: Elsevier.

24. Scheepers, G.H., J.A. Lycklama a Nijeholt, and B. Poolman, *An updated structural classification of substrate‐binding proteins.* FEBS letters, 2016. **590**(23): p. 4393-4401.

25. Tam, R. and M.H. Saier Jr, *Structural, functional, and evolutionary relationships among extracellular solute-binding receptors of bacteria.* Microbiological reviews, 1993. **57**(2): p. 320-346.

26. Quiocho, F.A. and P.S. Ledvina, *Atomic structure and specificity of bacterial periplasmic receptors for active transport and chemotaxis: variation of common themes.* Molecular microbiology, 1996. **20**(1): p. 17-25.

27. Khare, D., M.L. Oldham, C. Orelle, A.L. Davidson, and J. Chen, *Alternating access in maltose transporter mediated by rigid-body rotations.* Molecular cell, 2009. **33**(4): p. 528-536.

28. KELLERMANN, O. and S. SZMELCMAN, *Active transport of maltose in Escherichia coli K12: Involvement of a "periplasmic" maltose binding protein.* European journal of biochemistry, 1974. **47**(1): p. 139-149.

29. Sharff, A.J., L.E. Rodseth, J.C. Spurlino, and F.A. Quiocho, *Crystallographic evidence of a large ligand-induced hinge-twist motion between the two domains of the maltodextrin binding protein involved in active transport and chemotaxis.* Biochemistry, 1992. **31**(44): p. 10657-10663.

30. Spurlino, J.C., G.-Y. Lu, and F.A. Quiocho, *The 2.3-A resolution structure of the maltose-or maltodextrin-binding protein, a primary receptor of bacterial active transport and chemotaxis.* Journal of Biological Chemistry, 1991. **266**(8): p. 5202-5219.

31. Shuman, H.A., *Active transport of maltose in Escherichia coli K12. Role of the periplasmic maltose-binding protein and evidence for a substrate recognition site in the cytoplasmic membrane.* Journal of Biological Chemistry, 1982. **257**(10): p. 5455-5461.

32. Dietzel, I., V. Kolb, and W. Boos, *Pole cap formation in Escherichia coli following induction of the maltose-binding protein.* Archives of microbiology, 1978. **118**(2): p. 207-218.

33. Manson, M.D., W. Boos, P. Bassford Jr, and B. Rasmussen, *Dependence of maltose transport and chemotaxis on the amount of maltose-binding protein.* Journal of Biological Chemistry, 1985. **260**(17): p. 9727-9733.

34. Mächtel, R., A. Narducci, D.A. Griffith, T. Cordes, and C. Orelle, *An integrated transport mechanism of the maltose ABC importer.* Research in microbiology, 2019. **170**(8): p. 321-337.

35. Pistolesi, S. and N. Tjandra, *Temperature dependence of molecular interactions involved in defining stability of glutamine binding protein and its complex with L-glutamine.* Biochemistry, 2012. **51**(2): p. 643-652.

36. Su, J.G., X. Jiao, T.G. Sun, C.H. Li, W. Zu Chen, and C.X. Wang, *Analysis of domain movements in glutamine-binding protein with simple models.* Biophysical journal, 2007. **92**(4): p. 1326-1335.

37. Chen, P.-c., P. Masiewicz, K. Perez, and J. Hennig, *Structure-based screening of binding affinities via small-angle X-ray scattering.* IUCrJ, 2020. **7**(4).

38. Sun, T.G., J.P. Hu, C.H. Li, W. Zu Chen, and C.X. Wang, *A molecular dynamics simulation study of glutamine-binding protein.* Journal of Molecular Structure: THEOCHEM, 2005. **725**(1-3): p. 9-16.

39. Sun, Y.-J., J. Rose, B.-C. Wang, and C.-D. Hsiao, *The structure of glutamine-binding protein complexed with glutamine at 1.94 Å resolution: comparisons with other amino acid binding proteins.* Journal of molecular biology, 1998. **278**(1): p. 219-229.

40. Gerstein, M., A.M. Lesk, and C. Chothia, *Structural mechanisms for domain movements in proteins.* Biochemistry, 1994. **33**(22): p. 6739-6749.

41. Feng, Y., L. Zhang, S. Wu, Z. Liu, X. Gao, X. Zhang, M. Liu, J. Liu, X. Huang, and W. Wang, *Conformational Dynamics of apo‐GlnBP Revealed by Experimental and Computational Analysis.* Angewandte Chemie International Edition, 2016. **55**(45): p. 13990-13994.

42. Pang, A., Y. Arinaminpathy, M.S. Sansom, and P.C. Biggin, *Interdomain dynamics and ligand binding: molecular dynamics simulations of glutamine binding protein.* FEBS letters, 2003. **550**(1-3): p. 168-174.

43. Wu, S., W. Zhang, W. Li, W. Huang, Q. Kong, Z. Chen, W. Wei, and S. Yan, *Dissecting the Protein Dynamics Coupled Ligand Binding with Kinetic Models and Single-Molecule FRET.* Biochemistry, 2022.

44. Zhang, L., S. Wu, Y. Feng, D. Wang, X. Jia, Z. Liu, J. Liu, and W. Wang, *Ligand-bound glutamine binding protein assumes multiple metastable binding sites with different binding affinities.* Communications biology, 2020. **3**(1): p. 1-11.

45. Gouridis, G., Y.A. Muthahari, M. de Boer, D.A. Griffith, A. Tsirigotaki, K. Tassis, N. Zijlstra, R. Xu, N. Eleftheriadis, and Y. Sugijo, *Structural dynamics in the evolution of a bilobed protein scaffold.* Proceedings of the National Academy of Sciences, 2021. **118**(49).

46. Kooshapur, H., J. Ma, N. Tjandra, and G.A. Bermejo, *NMR Analysis of Apo Glutamine‐Binding Protein Exposes Challenges in the Study of Interdomain Dynamics.* Angewandte Chemie International Edition, 2019. **58**(47): p. 16899-16902.

47. Kienlein, M. and M. Zacharias, *Ligand binding and global adaptation of the GlnPQ substrate binding domain 2 revealed by molecular dynamics simulations.* Protein Science, 2020. **29**(12): p. 2482-2494.

48. Gouridis, G., G.K. Schuurman-Wolters, E. Ploetz, F. Husada, R. Vietrov, M. De Boer, T. Cordes, and B. Poolman, *Conformational dynamics in substrate-binding domains influences transport in the ABC importer GlnPQ.* Nature Structural & Molecular Biology, 2015. **22**(1): p. 57-64.

49. Nir, E., X. Michalet, K.M. Hamadani, T.A. Laurence, D. Neuhauser, Y. Kovchegov, and S. Weiss, *Shot-noise limited single-molecule FRET histograms: comparison between theory and experiments.* The Journal of Physical Chemistry B, 2006. **110**(44): p. 22103-22124.

50. Gebhardt, C., M. Lehmann, M.M. Reif, M. Zacharias, G. Gemmecker, and T. Cordes, *Molecular and spectroscopic characterization of green and red cyanine fluorophores from the Alexa Fluor and AF series.* ChemPhysChem, 2021. **22**(15): p. 1566-1583.

51. Harris, P.D., A. Narducci, C. Gebhardt, T. Cordes, S. Weiss, and E. Lerner, *Multi-parameter photon-by-photon hidden Markov modeling.* Nature communications, 2022. **13**(1): p. 1-12.

52. Ingargiola, A., E. Lerner, S. Chung, S. Weiss, and X. Michalet, *FRETBursts: an open source toolkit for analysis of freely-diffusing single-molecule FRET.* PloS one, 2016. **11**(8): p. e0160716.

53. Dahiya, V., G. Agam, J. Lawatscheck, D.A. Rutz, D.C. Lamb, and J. Buchner, *Coordinated conformational processing of the tumor suppressor protein p53 by the Hsp70 and Hsp90 chaperone machineries.* Molecular cell, 2019. **74**(4): p. 816-830. e7.

54. Kudryavtsev, V., M. Sikor, S. Kalinin, D. Mokranjac, C.A. Seidel, and D.C. Lamb, *Combining MFD and PIE for accurate single -pair Förster resonance energy transfer measurements.* ChemPhysChem, 2012. **13**(4): p. 1060-1078.

55. Agam, G., C. Gebhardt, M. Popara, R. Maechtel, J. Folz, B. Ambrose, N. Chamachi, S.Y. Chung, T.D. Craggs, and M. de Boer, *Reliability and accuracy of single-molecule FRET studies for characterization of structural dynamics and distances in proteins.* bioRxiv, 2022: p. 2022.08. 03.502619.

56. Schrimpf, W., A. Barth, J. Hendrix, and D.C. Lamb, *PAM: a framework for integrated analysis of imaging, single-molecule, and ensemble fluorescence data.* Biophysical journal, 2018. **114**(7): p. 1518-1528.

57. Edelstein, A., N. Amodaj, K. Hoover, R. Vale, and N. Stuurman, *Computer control of microscopes using µManager.* Current protocols in molecular biology, 2010. **92**(1): p. 14.20. 1-14.20. 17.

58. Preus, S., S.L. Noer, L.L. Hildebrandt, D. Gudnason, and V. Birkedal, *iSMS: single-molecule FRET microscopy software.* Nature Methods, 2015. **12**(7): p. 593-594.

59. Kong, X., E. Nir, K. Hamadani, and S. Weiss, *Photobleaching pathways in single-molecule FRET experiments.* Journal of the American Chemical Society, 2007. **129**(15): p. 4643-4654.

60. Boos, W. and H. Shuman, *Maltose/maltodextrin system of Escherichia coli: transport, metabolism, and regulation.* Microbiology and Molecular Biology Reviews, 1998. **62**(1): p. 204-229.

61. de Boer, M., G. Gouridis, Y.A. Muthahari, and T. Cordes, *Single-molecule observation of ligand binding and conformational changes in FeuA.* Biophysical journal, 2019. **117**(9): p. 1642-1654.

62. Kapanidis, A.N., N.K. Lee, T.A. Laurence, S. Doose, E. Margeat, and S. Weiss, *Fluorescence-aided molecule sorting: analysis of structure and interactions by alternating-laser excitation of single molecules.* Proceedings of the National Academy of Sciences, 2004. **101**(24): p. 8936-8941.

63. Hohlbein, J., T.D. Craggs, and T. Cordes, *Alternating-laser excitation: single-molecule FRET and beyond.* Chemical Society Reviews, 2014. **43**(4): p. 1156-1171.

64. Van Der Velde, J.H., J. Oelerich, J. Huang, J.H. Smit, A. Aminian Jazi, S. Galiani, K. Kolmakov, G. Gouridis, C. Eggeling, and A. Herrmann, *A simple and versatile design concept for fluorophore derivatives with intramolecular photostabilization.* Nature communications, 2016. **7**(1): p. 1-17.

65. Hwang, H., H. Kim, and S. Myong, *Protein induced fluorescence enhancement as a single molecule assay with short distance sensitivity.* Proceedings of the National Academy of Sciences, 2011. **108**(18): p. 7414-7418.

66. Rashid, F., V.-S. Raducanu, M.S. Zaher, M. Tehseen, S. Habuchi, and S.M. Hamdan, *Initial state of DNA-Dye complex sets the stage for protein induced fluorescence modulation.* Nature communications, 2019. **10**(1): p. 2104.

67. Ploetz, E., G.K. Schuurman-Wolters, N. Zijlstra, A.W. Jager, D.A. Griffith, A. Guskov, G. Gouridis, B. Poolman, and T. Cordes, *Structural and biophysical characterization of the tandem substrate-binding domains of the ABC importer GlnPQ.* Open Biology, 2021. **11**(4): p. 200406.

68. Lerner, E., E. Ploetz, J. Hohlbein, T. Cordes, and S. Weiss, *A quantitative theoretical framework for protein-induced fluorescence enhancement–Forster-type resonance energy transfer (PIFE-FRET).* The Journal of Physical Chemistry B, 2016. **120**(26): p. 6401-6410.

69. Tjandra, N., V. Simplaceanu, P.F. Cottam, and C. Ho, *Multidimensional1H and15N NMR investigation of glutamine-binding protein ofEscherichia coli.* Journal of Biomolecular NMR, 1992. **2**(2): p. 149-160.

70. Velázquez-Campoy, A., H. Ohtaka, A. Nezami, S. Muzammil, and E. Freire, *Isothermal titration calorimetry.* Current protocols in cell biology, 2004. **23**(1): p. 17.8. 1-17.8. 24.

71. Hellenkamp, B., S. Schmid, O. Doroshenko, and O. Opanasyuk, *Kü hnemuth R, Adariani SR, Ambrose B, Aznauryan M, Barth A, Birkedal V et al.: Precision and accuracy of single-molecule FRET measurements–a multi-laboratory benchmark study.* Nat Methods, 2018. **15**: p. 984.

72. Kalinin, S., T. Peulen, S. Sindbert, P.J. Rothwell, S. Berger, T. Restle, R.S. Goody, H. Gohlke, and C.A. Seidel, *A toolkit and benchmark study for FRET-restrained high-precision structural modeling.* Nature methods, 2012. **9**(12): p. 1218-1225.

73. Peter, M.F., C. Gebhardt, R. Mächtel, J. Glaenzer, G.H. Thomas, T. Cordes, and G. Hagelueken, *Cross-validation of distance measurements in proteins by PELDOR/DEER and single-molecule FRET.* bioRxiv, 2020.

74. Hellenkamp, B., S. Schmid, O. Doroshenko, O. Opanasyuk, R. Kühnemuth, S. Rezaei Adariani, B. Ambrose, M. Aznauryan, A. Barth, and V. Birkedal, *Precision and accuracy of single-molecule FRET measurements—a multi-laboratory benchmark study.* Nature methods, 2018. **15**(9): p. 669-676.

75. Kalinin, S., A. Valeri, M. Antonik, S. Felekyan, and C.A. Seidel, *Detection of structural dynamics by FRET: a photon distribution and fluorescence lifetime analysis of systems with multiple states.* The Journal of Physical Chemistry B, 2010. **114**(23): p. 7983-7995.

76. Torres, T. and M. Levitus, *Measuring conformational dynamics: a new FCS-FRET approach.* The Journal of Physical Chemistry B, 2007. **111**(25): p. 7392-7400.

77. Grosdidier, A., V. Zoete, and O. Michielin, *Fast docking using the CHARMM force field with EADock DSS.* Journal of computational chemistry, 2011. **32**(10): p. 2149-2159.

78. Grosdidier, A., V. Zoete, and O. Michielin, *SwissDock, a protein-small molecule docking web service based on EADock DSS.* Nucleic acids research, 2011. **39**(suppl_2): p. W270-W277.

79. Widengren, J. and P. Schwille, *Characterization of photoinduced isomerization and back-isomerization of the cyanine dye Cy5 by fluorescence correlation spectroscopy.* The Journal of Physical Chemistry A, 2000. **104**(27): p. 6416-6428.

80. Glembockyte, V., J. Lin, and G. Cosa, *Improving the photostability of red- and green-emissive single-molecule fluorophores via Ni2+ mediated excited triplet-state quenching.* The Journal of Physical Chemistry B, 2016. **120**(46): p. 11923-11929.

81. Rasnik, I., S.A. McKinney, and T. Ha, *Nonblinking and long-lasting single-molecule fluorescence imaging.* Nature methods, 2006. **3**(11): p. 891-893.

82. Shilton, B.H., M.M. Flocco, M. Nilsson, and S.L. Mowbray, *Conformational changes of three periplasmic receptors for bacterial chemotaxis and transport: the maltose-, glucose/galactose-and ribose-binding proteins.* Journal of molecular biology, 1996. **264**(2): p. 350-363.

83. Skrynnikov, N.R., N.K. Goto, D. Yang, W.-Y. Choy, J.R. Tolman, G.A. Mueller, and L.E. Kay, *Orienting domains in proteins using dipolar couplings measured by liquid-state NMR: differences in solution and crystal forms of maltodextrin binding protein loaded with β -cyclodextrin.* Journal of molecular biology, 2000. **295**(5): p. 1265-1273.

84. Trakhanov, S., N.K. Vyas, H. Luecke, D.M. Kristensen, J. Ma, and F.A. Quiocho, *Ligand-free and-bound structures of the binding protein (LivJ) of the Escherichia coli ABC leucine/isoleucine/valine transport system: trajectory and dynamics of the interdomain rotation and ligand specificity.* Biochemistry, 2005. **44**(17): p. 6597-6608.

85. Wang, Y., C. Tang, E. Wang, and J. Wang, *Exploration of multi-state conformational dynamics and underlying global functional landscape of*

maltose binding protein. PLoS computational biology, 2012. **8**(4): p. e1002471.

86. Berntsson, R.P.-A., S.H. Smits, L. Schmitt, D.-J. Slotboom, and B. Poolman, *A structural classification of substrate-binding proteins.* FEBS letters, 2010. **584**(12): p. 2606-2617.

87. Henzler-Wildman, K.A., V. Thai, M. Lei, M. Ott, M. Wolf-Watz, T. Fenn, E. Pozharski, M.A. Wilson, G.A. Petsko, and M. Karplus, *Intrinsic motions along an enzymatic reaction trajectory.* Nature, 2007. **450**(7171): p. 838-844.

88. Fernandes, D.D., C. Neale, G.-N.W. Gomes, Y. Li, A. Malik, A. Pandey, A.P. Orazietti, X. Wang, L. Ye, and R. Scott Prosser, *Ligand modulation of the conformational dynamics of the A2A adenosine receptor revealed by single-molecule fluorescence.* Scientific reports, 2021. **11**(1): p. 1-16.

89. Maslov, I., O. Volkov, P. Khorn, P. Orekhov, A. Gusach, P. Kuzmichev, A. Gerasimov, A. Luginina, Q. Coucke, and A. Bogorodskiy, *Sub-millisecond conformational dynamics of the A2A adenosine receptor revealed by single-molecule FRET.* bioRxiv, 2020.

90. Calabrese, A.N., B. Schiffrin, M. Watson, T.K. Karamanos, M. Walko, J.R. Humes, J.E. Horne, P. White, A.J. Wilson, and A.C. Kalli, *Inter-domain dynamics in the chaperone SurA and multi-site binding to its outer membrane protein clients.* Nature communications, 2020. **11**(1): p. 1-16.

91. Paul, F. and T.R. Weikl, *How to distinguish conformational selection and induced fit based on chemical relaxation rates.* PLOS Computational Biology, 2016. **12**(9): p. e1005067.

92. Vogt, A.D. and E. Di Cera, *Conformational selection or induced fit? A critical appraisal of the kinetic mechanism.* Biochemistry, 2012. **51**(30): p. 5894-5902.

93. Weikl, T.R. and F. Paul, *Conformational selection in protein binding and function.* Protein Science, 2014. **23**(11): p. 1508-1518.

94. Hammes, G.G., Y.-C. Chang, and T.G. Oas, *Conformational selection or induced fit: a flux description of reaction mechanism.* Proceedings of the National Academy of Sciences, 2009. **106**(33): p. 13737-13741.

95. Ramanathan, A., A. Savol, P. Agarwal, and C.S. Chennubhotla, *Discovering conformational sub-states relevant to protein function.* Biophysical Journal, 2011. **100**(3): p. 172a.

96. Telmer, P.G. and B.H. Shilton, *Insights into the conformational equilibria of maltose-binding protein by analysis of high affinity mutants.* Journal of Biological Chemistry, 2003. **278**(36): p. 34555-34567.

97. Oldham, M.L., D. Khare, F.A. Quiocho, A.L. Davidson, and J. Chen, *Crystal structure of a catalytic intermediate of the maltose transporter.* Nature, 2007. **450**(7169): p. 515-521.

98. Zhou, R., S. Kunzelmann, M.R. Webb, and T. Ha, *Detecting intramolecular conformational dynamics of single molecules in short distance range with subnanometer sensitivity.* Nano letters, 2011. **11**(12): p. 5482-5488.

99. Chan, F.T., C.F. Kaminski, and G.S. Kaminski Schierle, *HomoFRET Fluorescence Anisotropy Imaging as a Tool to Study Molecular Self-Assembly in Live Cells.* ChemPhysChem, 2011. **12**(3): p. 500-509.

100. Enderlein, J., I. Gregor, D. Patra, T. Dertinger, and U.B. Kaupp, *Performance of fluorescence correlation spectroscopy for measuring diffusion and concentration.* ChemPhysChem, 2005. **6**(11): p. 2324-2336.

101. Martyn, T.A., J.L. Moore, R.L. Halterman, and W.T. Yip, *Cucurbit [7] uril induces superior probe performance for single-molecule detection.* Journal of the American Chemical Society, 2007. **129**(34): p. 10338-10339.

102. Olesińska, M., G. Wu, S. Gómez-Coca, D. Antón-García, I. Szabó, E. Rosta, and O.A. Scherman, *Modular supramolecular dimerization of optically tunable extended aryl viologens.* Chemical science, 2019. **10**(38): p. 8806-8811.

103. Mohanty, J. and W.M. Nau, *Ultrastable rhodamine with cucurbituril.* Angewandte Chemie, 2005. **117**(24): p. 3816-3820.